# NOVEL METHODS FOR MICROSTRUCTURE-SENSITIVE PROBABILISTIC FATIGUE NOTCH FACTOR

A Thesis
Presented to
The Academic Faculty

by

William D. Musinski

In Partial Fulfillment
of the Requirements for the Degree
Master of Science in the
George W. Woodruff School of Mechanical Engineering

Georgia Institute of Technology
August 2010

# NOVEL METHODS FOR MICROSTRUCTURE-SENSITIVE PROBABILISTIC FATIGUE NOTCH FACTOR

Approved by:

Dr. David L. McDowell
George W. Woodruff School of Mechanical Engineering
*Georgia Institute of Technology*

Dr. Richard W. Neu
George W. Woodruff School of Mechanical Engineering
*Georgia Institute of Technology*

Dr. Ken Gall
George W. Woodruff School of Mechanical Engineering
*Georgia Institute of Technology*

Date Approved: 29 April 2010

# ACKNOWLEDGEMENTS

First and foremost, I would like to thank my advisor Dr. David L. McDowell for his patience, direction, and encouragement throughout the completion of this work. He offered thoughtful insight and helpful comments at pertinent times of this research. I also would like to thank the other committee members, Dr. Richard W. Neu and Dr. Ken Gall, for their careful review of this thesis and recommendations for future work. I would like to thank all of the people I met through my stay at Georgia Tech, especially my colleagues within the McDowell group, for their friendship and shared rapport. I deeply appreciate the support and funding from Pratt and Whitney towards my research activities, without would have not made this research a success. I would like to thank my family who has supported me throughout my career. Last and definitely not least, I would like to thank my wife, Melissa, who has loved and supported me throughout the research process.

# TABLE OF CONTENTS

# LIST OF TABLES

# LIST OF FIGURES

# SUMMARY

An extensive review of probabilistic techniques in fatigue analysis indicates that there is a need for new microstructure-sensitive methods in describing the effects of notches on the fatigue life reduction in cyclically loaded components. Of special interest are notched components made from polycrystalline nickel-base superalloys, which are used for high temperature applications in aircraft gas turbine engine disks. Microstructure-sensitive computational crystal plasticity is combined with novel probabilistic techniques to determine the probability of failure of notched components based on the distribution of slip within the notch root region and small crack initiation processes. The key microstructure features of two Ni-base superalloys, a fine and coarse grain IN100, are reviewed and the method in which these alloys are computationally modeled is presented. Next, the geometric model of the notched specimens and method of finite element polycrystalline reconstruction is demonstrated. Shear-based fatigue indicator parameters are used to characterize the shear-based, mode I formation and propagation of fatigue cracks. Finally, two different probabilistic approaches are described in this work including a grain-scale approach, which describes the probability of forming a crack on the order of grain size, and a transition crack length approach, which describes the probability of forming and propagating a crack to the transition crack length. These approaches are used to construct cumulative distribution functions for the probability of failure as a function of various notch root sizes and strain load amplitudes.

# CHAPTER I

# INTRODUCTION

## 1.1 Introduction

Traditional fatigue analysis schemes used for geometries with stress gradient fields (such as notches) have required many experiments to determine the probability of fatigue failure. Due to the extensive amount of scatter in high cycle fatigue (HCF) analysis, typically fatigue life data are fitted using a significant amount of experiments into an assumed distribution, such as a Weibull or lognormal distribution. The resulting notch effect on fatigue life is characterized via a notch root fatigue strength reduction factor, often alternatively called the fatigue notch factor, $K_f$. The experimental results are beneficial for life prediction of a given geometry and microstructure, but do not offer predictive insight into the underlying physical mechanisms that explain scatter, size effects, and gradient effects on fatigue damage. Moreover, if the material is changed, the fatigue notch factor changes for a given geometry. Computational crystal plasticity models that characterize sensitivity to microstructure variability, notch size and gradient effects, and extrinsic defects (inclusions, FOD) can be used to assist in characterizing these fatigue mechanisms and to provide insight into materials design and selection for a given application. The goal of this research is to develop approaches that combine computational crystal plasticity with nonlocal notch root plasticity and damage approaches for small crack formation in HCF, LCF, and mixed conditions, with applications to aircraft gas turbine engine materials. These approaches combine elements of crystal plasticity with new probabilistic methods for notch sensitivity based on computed slip distributions in the microstructure at the notch root.

## 1.2 Scope of Thesis

The purpose of this research is to extend microstructure-sensitive nonlocal fatigue modeling methodology previously conducted in the McDowell research group [1–3] to next generation notch root analysis. Preliminary efforts within our group [4] formed the initial foundation for the present work. This method incorporates such effects as notch size effect, peak stress, stress gradient, and microstructure variability through characterization of probability distributions of slip and small crack initiation processes. These distributions are informed by computational crystal plasticity simulations on realistic microstructures. Additionally, the concept of the fatigue notch factor, $K_f$, is extended to include microstructure sensitivity effects resulting from these probability distributions.

## 1.3 Layout of Thesis

This thesis is divided into five chapters:

- Chapter II provides the background information for this thesis. Previous approaches to fatigue notch analysis are introduced and analyzed for their deficiencies. Next, the motivation for the development of a new microstructure-sensitive fatigue notch factor is emphasized based on the need to consider microstructure effects in fatigue and the experimental time to characterize a given microstructure. Finally, probabilistic approaches previously used in fatigue analysis are reviewed.

- Chapter III presents the material model used for analysis. First, the microstructure of nickel-base superalloys and the crystal plasticity model used to represent the constitutive response are introduced. Next, this chapter introduces the means in which different stages of fatigue crack formation and microstructurally small crack growth are modeled. Finally, this chapter describes the geometric

model of the notched specimens used and the method in which the polycrystalline microstructure is reconstructed and used in a finite element software.

- Chapter IV describes the probabilistic fatigue notch framework and results from using this framework. Grain-scale and transition crack length approaches are presented with justification for each analysis.

- Chapter V summarizes the thesis and offers recommendations for future work.

# CHAPTER II

# BACKGROUND

## 2.1 Introduction

Notches are prevalent in many different components at many different scales. They are present at the component scale in locations such as bolt holes and fillets and at a microstructural scale in the form of an inclusion or void, so-called "micronotches". Under loading, these notches induce a stress concentration and a stress gradient field emanating from the notch root. Typical analyses of notches are relatively outdated and characterized by a deterministic notch root strength reduction factor, often called the fatigue notch factor. The formation and growth of a crack from a notch is microstructurally dependent. These typical notch root analyses do not explicitly incorporate the physical mechanisms that account for notch sensitivity and effects of microstructure. Frequently, the fatigue notch root factor is a deterministic mean value that is estimated using experiments. The goal of this research is to use computational crystal plasticity constitutive equations and probabilistic schemes to inform a microstructure-sensitive fatigue notch factor. Prior to introduction of a new microstructure-sensitive fatigue notch factor, previous approaches to notch root analysis and probabilistic techniques used for fatigue variability are reviewed.

## 2.2 Traditional Fatigue Notch Root Analysis Schemes

Traditional simplified notch root analysis techniques employ a global-local approach to analyzing the fatigue response of notched specimens. If the local stress and strain components due to a remote applied stress are known within the notch root field, the fatigue life can be estimated using stress-life or strain-life approaches based on

smooth specimen experimental results. Therefore, a significant amount of research has been devoted to estimating the stress and strain components near the notch root.

### 2.2.1 Elastic Stress Concentration Factor

Near notches and other stress concentration sites, the maximum local stress near the notch root, $\sigma_{max}$, is larger than the remote applied stress, $S_a$. In linear elastic materials, the ratio of these stresses is the theoretical elastic stress concentration factor

$$K_t = \frac{\sigma_{max}}{S_a} \tag{2.1}$$

The theoretical elastic stress concentration factor depends on the geometry of the specimen and the nature of the loading condition (bending, tensile, torsional, etc.). A compilation of stress concentration factors can be found in Peterson's book [5].

### 2.2.2 Fatigue Notch Factor and Notch Sensitivity Index

When considering fatigue in a stress-life approach, the fatigue strength "knock-down effect" of notches is depicted through the fatigue notch factor, $K_f$. The fatigue notch factor is the ratio of fatigue strength of an unnotched (or smooth) member to the fatigue strength of a notched specimen at a given life, i.e.,

$$K_f = \frac{\sigma_f^{unnotched}}{\sigma_f^{notched}} \tag{2.2}$$

The fatigue notch factor is often measured experimentally at a life of $10^6$ cycles for a probability of failure of 50%. It depends on geometry, loading condition, and varies with material. Values of the fatigue notch factor vary from $K_f = 1$ (no notch effect) to $K_f = K_t$ (full theoretical elastic stress concentration effect). The relationship between the elastic stress concentration, $K_t$, and the fatigue notch factor, $K_f$, is often depicted through the notch sensitivity factor, $q$, i.e.,

$$q = \frac{K_f - 1}{K_t - 1} \tag{2.3}$$

Values of $q$ range from 0 (no notch effect) to 1 (full theoretical elastic stress concentration effect).

### 2.2.3 Critical Distance Methods

Critical distance methods consider the local or average stress value over a significant length scale at the notch root when analyzing fatigue potency of a notched component. These methods can be categorized into point, line, 2D and 3D methods [4].

#### *2.2.3.1 Traditional Peterson and Neuber Methods*

Some of the more traditional point and average stress models include the Peterson [5] and Neuber [6] approaches. Through experimental correlation, Peterson and Neuber have proposed analytical relationships for finding the notch sensitivity factor. The Peterson approach is a point stress model that considers the stress at a characteristic distance ($d_o$) away from the notch root. If this value is greater than or equal to the fatigue strength of a smooth specimen, then fatigue failure is assumed. Assuming that the stress near the notch root decays linearly, Peterson proposed [5]

$$q = \frac{1}{1 + a/r} \tag{2.4}$$

where $r$ is the notch root radius and $a$ is a material constant determined through many experiments. Combining equations 2.3 and 2.4 yields the classical Peterson equation for the fatigue notch factor,

$$K_f = 1 + \frac{K_t - 1}{1 + a/r} \tag{2.5}$$

When plotting $K_f$ vs. $r$, the plot exhibits a characteristic sigmoidal shape [7].

The Neuber approach is different from the Peterson approach in that it compares the fatigue limit to the average stress over a characteristic length. Neuber proposed [6]

$$q = \frac{1}{1 + \sqrt{\rho/r}} \ , \tag{2.6}$$

where $\rho$ is an experimentally correlated material constant. Combining equations 2.3 and 2.6, the fatigue notch factor becomes:

$$K_f = 1 + \frac{K_t - 1}{1 + \sqrt{\rho/r}} \tag{2.7}$$

The Peterson and Neuber approaches are first order attempts to incorporate a material length scale in describing notch sensitivity as a function of material ($a$ and $\rho$), notch geometry ($K_t$), notch size ($r$), and loading condition ($K_t$). Generally, for two different sized notches with similar geometries (identical $K_t$ values), the specimen with a larger notch will have a higher fatigue notch factor and lower fatigue strength. This phenomenon is often referred to as the notch size effect.

There are many other analytical relationships for the fatigue notch factor that have been proposed by different researchers. A list of these can be found in review papers such as Qylafku et al. [8] or Weixing et al. [9]. Each approach is an attempt to simplify the complex behavior of fatigue in notches to a few geometric and characteristic material parameters. One major downfall to these approaches is that the fatigue notch factors are commonly determined through time-consuming, costly experiments on notched and smooth specimens for very long lives. Also, these techniques do not consider the effect of microstructure, stress field gradients, and grain size and orientation on notch size effects.

#### *2.2.3.2 Stress Field Intensity Models*

The stress field intensity approach is an attempt to characterize the fatigue damage of notched components based on the peak stress and the stress field intensity within the notch root zone. This approach finds the average stress by integrating the notch root stress distribution, using continuum elastic-plastic finite element analyses, over a critical distance. The stress intensity function takes the general form [8–11]

$$\sigma_{SFI} = \frac{1}{D} \int_D f\left(\sigma_{ij}\right) \varphi\left(\mathbf{r}\right) dD \ , \tag{2.8}$$

where $f(\sigma_{ij})$ is the equivalent stress as a function of the stress tensor, $\varphi(\mathbf{r})$ is a weight function that depends on the distance $\mathbf{r}$ from the notch root, and $D$ is the highly stressed volume domain in which fatigue damage is expected. The domain can be 1D (line), 2D (planar) or fully 3-dimensional, depending on complexity of the problem/analysis. The weight function is a monotonically decreasing function that depends on notch geometry, loading type, boundary conditions and material properties. In this model, fatigue failure is assumed when the stress field intensity function reaches a critical equivalent stress, i.e., $\sigma_{SFI} \geq \sigma_f$.

The stress field intensity approach can be used to estimate the fatigue notch factor [9]. First, the critical stress field intensity is found for the notched and smooth specimens. For a smooth specimen,

$$\sigma_{SFI,cr} = S_e \tag{2.9}$$

where $S_e$ is the endurance limit of the material. For a notched component, the stress tensor is a function of the net applied stress ($S_N$), i.e. $\sigma_{ij} = \sigma_{ij}(S_N)$. Thus, if we define an equivalent stress function as $f(\hat{\sigma}_{ij}) = f(\sigma_{ij})/S_N$, the critical stress field intensity for a notched specimen can be written as

$$\sigma^N_{SFI,cr} = \frac{S_N}{D} \int_D f(\hat{\sigma}_{ij})\, \varphi(\mathbf{r})\, dD \tag{2.10}$$

Combining Equations 2.9 and 2.10, the fatigue notch factor can be calculated using the stress field intensity approach as

$$K_f = \frac{S_e}{S_N} = \frac{1}{D} \int_D f(\hat{\sigma}_{ij})\, \varphi(\mathbf{r})\, dD \tag{2.11}$$

The stress intensity approach is a more general case of the Peterson and Neuber approaches [9]. For example, if the weight function is the Dirac delta function of the form $\varphi(\mathbf{r}) = \delta(r - d_o)$ the stress field intensity is equivalent to Peterson's point stress model. If the weight function is equal to unity, then the stress field intensity

is equivalent to the average stress over the highly stressed domain. In this case, the stress intensity is equal to Neuber's approach.

### 2.2.4 Strain Life Notch Approaches

For notches that are loaded in the low cycle fatigue (LCF) regime, the strain-life approach is more readily used. Below the yield point at the notch root, the local stresses and strains at the notch ($\sigma$ and $\epsilon$) are linearly related to the remotely applied loads ($S$ and $e$), through the stress concentration factor. For notches with localized plasticity in the notch root region, it is very difficult to experimentally measure the local stresses and strains in the notch root field. Due to the constraint imposed by the elastically stressed material surrounding the plastic zone, deformation at the notch root is close to a strain-controlled condition. Therefore, the strain-life approach has been developed to estimate the material response at the notch root. Thus, the basic assumption of the strain-life approach is that a smooth specimen tested under strain-control ($\sigma_a$,$\epsilon_a$) can simulate the damage of a notched specimen exposed to a remotely applied ($S_a$, $e_a$) load if they have identical stress-strain loading histories (cf. Figure 2.1). The smooth specimen is used as a basis for comparison with the critically stressed zone of the notched specimen. Under strain-life assumptions, the failure of the laboratory smooth specimen is assumed to correspond to "crack initiation" in the critically stressed zone of the notched specimen.

#### *2.2.4.1 "Crack Initiation"*

The distinction of "crack initiation" is not always well-defined. It depends strongly on the length scale of interest and the ability to detect a crack at that scale. Traditionally, crack initiation corresponded to the formation of a crack on the order of 0.5 mm to 2.0 mm in length [12]. This was due impart to the limited ability of the naked eye to resolve a surface crack to a scale finer than a millimeter. The ability to detect both surface and subsurface cracks has been augmented by non-destructive techniques.

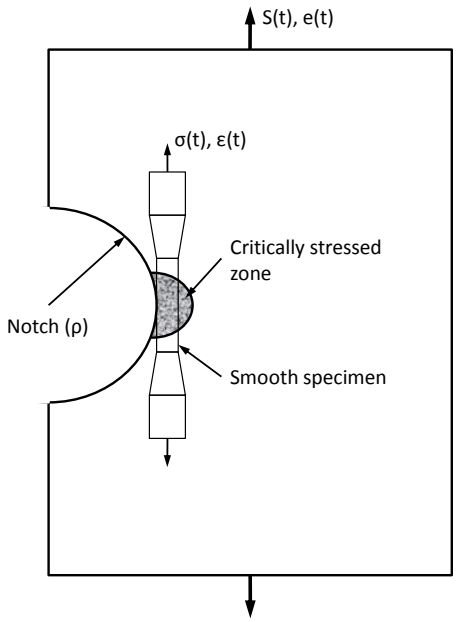


**Figure 2.1:** Notch strain-life assumption of equivalent stressed volume of material. After ref. [7].

However, non-destructive techniques are also limited in their ability to detect cracks that are less than a millimeter. Following the formation of a crack to this length ($\approx 1\,\text{mm}$), fracture mechanics has traditionally been employed to estimate the growth of the crack to a critical crack length.

Interestingly, due to the advent of high-powered electron microscopes with the ability to resolve cracks to a much finer scale, the study of "crack initiation" over the last 20-30 years has experienced a paradigm shift to the study of formation of small cracks on the order of micrometers (alternatively, known as microcracks). Consequently, the study of the crack growth behavior of these microcracks from scales of microns to millimeters has emerged as a significant research topic that is still prevalent today. As the microcrack grows from the micron to millimeter scale, the growth behavior progressively has less dependence on local microstructure. The behavior of small crack growth can be distinguished into regimes of microstructurally small crack growth and mechanically or physically small crack growth. Small crack growth

behavior will be described in more detail in Section 2.3.2.

Thus, based on the current ability to detect cracks at the scale of micrometers, the strain-life estimation of "crack initiation" in a notched component would constitute both microcrack nucleation and small crack growth regimes. The crack initiation life can be estimated through various approaches including the Basquin's equation for HCF, Coffin-Manson equation for LCF, or a combination of the two for the full range of fatigue lives [7].

#### *2.2.4.2 Elastic-Plastic Stress Concentration Factor*

In order to find the stress and strain histories near the notch root under elastic-plastic conditions, many estimation techniques have been developed. Perhaps the most noteworthy are those proposed by Neuber [6] and Molski and Glinka [13]. Under fully elastic conditions in the uniaxial case, stress and strain are linearly related through Hooke's law, $\sigma = E\epsilon$. When plasticity occurs, the uniaxial stress-strain response becomes non-linear and is typically modeled through other techniques such as the Ramberg-Osgood relationship [14], i.e.,

$$\epsilon = \frac{\sigma}{E} + \left(\frac{\sigma}{H}\right)^{1/n} \tag{2.12}$$

where $H$ is monotonic strength coefficient and $n$ is the strain hardening exponent, which typically ranges from 0-0.5 [15]. The first and second terms on the right hand side of Equation 2.12 are the elastic and plastic strains, respectively. Analogously, the cyclic hysteresis curve can be described by

$$\frac{\Delta\epsilon}{2} = \frac{\Delta\sigma}{2E} + \left(\frac{\Delta\sigma}{2K'}\right)^{1/n'} \tag{2.13}$$

where $K'$ and $n'$ are the cyclic strength coefficient and cyclic strain hardening exponent, respectively. Here, the Massing hypothesis of tension-compression symmetry is assumed. These constants are generally not equal to their monotonic counterparts.

Prior to yielding, the elastic stress concentration factor, $K_t$, is equal to the local stress concentration factor, $K_\sigma = \sigma/S$, and the local strain concentration factor, $K_\epsilon = \epsilon/e$. Due to the material response, when yielding occurs, the local strain is higher than that predicted by $K_t$ and the local stress is lower than that predicted by $K_t$, as depicted by Figure 2.2. The theoretical stress concentration should lie somewhere in between $K_\sigma$ and $K_\epsilon$. Based on nonlinear elastic analyses, Neuber [6] proposed that the theoretical stress concentration should be the geometric mean of the stress and strain concentration factor, i.e.,

$$K_t = \sqrt{K_\sigma K_\epsilon} \tag{2.14}$$

Equation 2.14 is known as Neuber's rule. Under monotonic loading, this relationship can be restated in a different form using the stress and strain concentration factors as

$$\frac{(K_t S)^2}{E} = \sigma\epsilon = \frac{\sigma^2}{E} + \sigma\left(\frac{\sigma}{H}\right)^{1/n} \tag{2.15}$$

Molski and Glinka [13] introduced an energy-based method to estimate the local stress-strain history near the notch root. Using the Ramberg-Osgood relationship (Equation 2.12), the local strain energy in the notch root region can be calculated as

$$W_\sigma = \int_0^\epsilon \sigma(\epsilon)\, d\epsilon = \frac{\sigma^2}{2E} + \frac{\sigma}{n+1}\left(\frac{\sigma}{H}\right)^{1/n} \tag{2.16}$$

Assuming that localized plasticity near the notch root does not effect the overall strain energy distribution within the notch root, the stress concentration factor can be estimated as

$$K_t = \left(\frac{W_\sigma}{W_S}\right)^{1/2} \tag{2.17}$$

where $W_\sigma$ is the strain energy per unit volume due to local stress and strain at the notch root and $W_S$ is the elastic strain energy per unit volume due to the nominal remote applied stress S. Thus, Equations 2.16 and 2.17 can be combined and rearranged

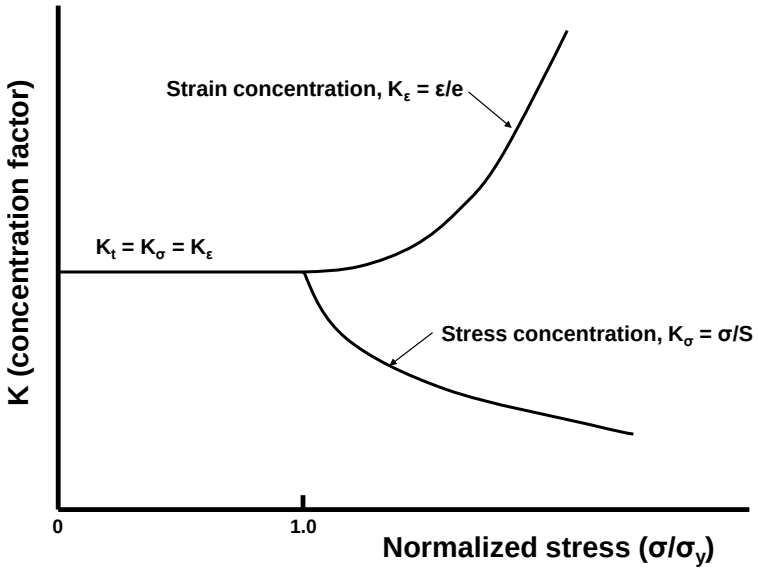


**Figure 2.2:** Effect of yielding on stress and strain concentration factors. After ref. [7].

to give

$$\frac{(K_t S)^2}{2E} = \frac{\sigma^2}{2E} + \frac{\sigma}{n+1}\left(\frac{\sigma}{H}\right)^{1/n} \tag{2.18}$$

## 2.3 Motivation for Microstructure Sensitive Fatigue Notch Factor

### 2.3.1 Microstructure Effects Not Taken Into Account

The empirical methods described in the previous section can indicate size effects and notch sensitivity without direct consideration of microstructure. However, these simplified models do not fully characterize the complexity of the problem. There is a great deal of uncertainty when estimating $K_f$ and $q$ values using these methods due to the significant amount of scatter in high cycle fatigue life (2-3 orders of magnitude). This scatter can be linked to the variability in material microstructure. In HCF, cyclic plastic strain is heterogeneously distributed within the notch damage process zone. The heterogeneous distribution of plastic strain can be due to many factors including texture, grain size distribution, internal defect localization, proximity to

the surface and hardening mechanisms. These microstructural attributes in turn affect the probability of fatigue crack formation and small crack growth from a notch. Thus, an approach based on average stress or stress field intensity is not a sufficient driving force for fatigue crack initiation at the notch root. Therefore, a coupled computational and statistical approach that considers the distribution of slip within grains among multiple instantiations is needed.

Another issue with the previous $K_f$ and $q$ estimation approaches is that they are usually determined from the mean of a number of experiments (typically limited) and are directed toward a probability of failure of 50%. Many fatigue-critical gas turbine engine components are typically designed for "safe-life" replacement based on statistical analysis on a large database of fatigue data to estimate life for a desired probability of failure. When a statistically prescribed number of operating cycles corresponding to a given probability of failure, for example 0.1%, are used up, the entire assembly is replaced, even though a majority of the components may have a considerable amount of life remaining. Therefore, the ability to estimate the fatigue failure probability distribution, in addition to the mean, is of great importance for safe-life design components. However, it takes many experiments to build up statistics for low probability of failure related to the tail of this distribution.

### 2.3.2 Small Crack Behavior

There have been many investigations into the behavior of small/short fatigue crack growth. The growth of small cracks may be divided into two regimes, namely, (1) microstructurally small cracks and (2) physically or mechanically small cracks. Microstructurally small cracks are fatigue cracks that are comparable in size to a characteristic microstructure unit size, which could be grain size, average inclusion spacing, etc. [16]. Mechanically small cracks are those which are physically small ($< 1 - 2\,\text{mm}$) but no longer exhibit significant dependence on microstructure. The

crack length for this transition to relative microstructure insensitivity is often on the order of 3-10 grain diameters [12]. Based on multiple small crack growth experiments, (cf. [12,16–18]) for the same apparent driving force (applied $\Delta K$), small crack growth rates are significantly higher than large crack growth rates. Also, microstructurally small cracks (MSCs) grow below the long crack threshold [16, 18]. These conditions of (1) higher MSC growth rate at the same driving force (applied $\Delta K$) and (2) lower MSC growth thresholds as compared to large cracks, are observed in crack growth experiments on Udimet 720 (cf. Figure 2.3), a powder metal nickel-base superalloy with an average grain size of 10 μm. A majority of the small cracks in Figure 2.3 were classified as mechanically small and the rest were considered microstructurally small. The use of a linear elastic fracture mechanics (LEFM) estimation of driving force ($\Delta K$) in a regime in which LEFM is not applicable (conditions for similitude are not met) is a contributing factor to this small versus large crack growth rate discrepancy.

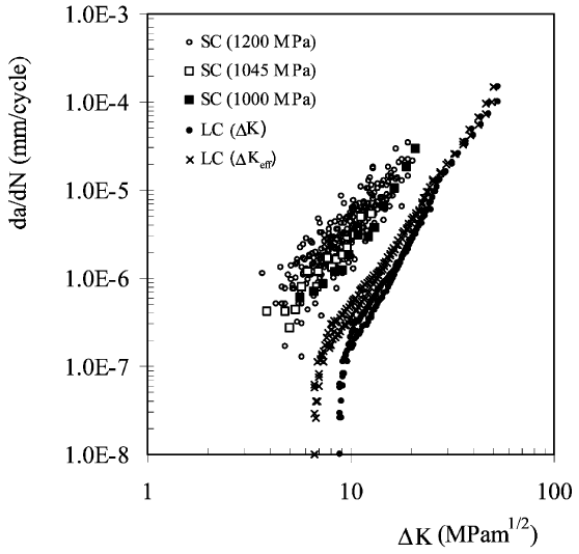


**Figure 2.3:** Small Crack (SC) vs. Large Crack (LC) Growth of a PM nickel-base superalloy Udimet 720 at room temperature [16]. Specimens were single edge notched specimens loaded under four-point bending with R=0.1 and f=10 Hz.

Another reason for higher small versus large crack growth rates is a direct consequence of the definition of $\Delta K$. As stated previously in Equation 3.21, for cyclic loading the change in the stress intensity factor is defined by $\Delta K = Y\Delta\sigma\sqrt{\pi a}$. For microstructurally small cracks, in order to have an equivalent driving force $\Delta K$ (as compared to a "large crack"), a higher local stress is required at the crack tip (as crack length $a$ decreases, $\Delta\sigma$ needs to increase for an equivalent $\Delta K$). As a consequence, a large crack tip plastic zone and crack tip blunting can occur and LEFM is not applicable in this case. Thus, a more applicable approach such as elastic-plastic fracture mechanics (EPFM) where $\Delta CTD$ (cyclic crack tip displacement), $\Delta J$ (cyclic J integral), or an equivalent stress intensity factor $\Delta K_{eq}$ are used to describe the crack driving force [19].

A further source for the anomalous behavior of small crack growth is effects from local microstructure barriers such as a grain boundary. High angle, or large disorientation, grain boundaries have been shown to hinder crack growth to a greater extent than low angle, or small disorientation, grain boundaries. As a result of these microstructure barriers, microstructurally small cracks display an oscillatory crack growth rate. As the MSC approaches a microstructure obstacle, the crack propagation rate decelerates until sufficient driving force is capable to propagate the crack past the microstructure barrier (cf. Figure 2.4). Otherwise, the MSC may arrest, corresponding to a small crack growth threshold. This effect has been shown in various materials including aluminum alloys [20, 21], pure titanium [18], and steels [22].

Crack closure can also affect the growth rate of small cracks. There are many possible sources of crack closure, including oxidation-assisted, plasticity-induced, roughness-induced, bridging mechanisms and phase transformation-induced crack closure. However, effects of crack closure, particularly plasticity-induced crack closure, are not nearly as significant as in the case of physically small and long crack growth. At near threshold $\Delta K$, oxide formation can cause crack closure and increase the threshold

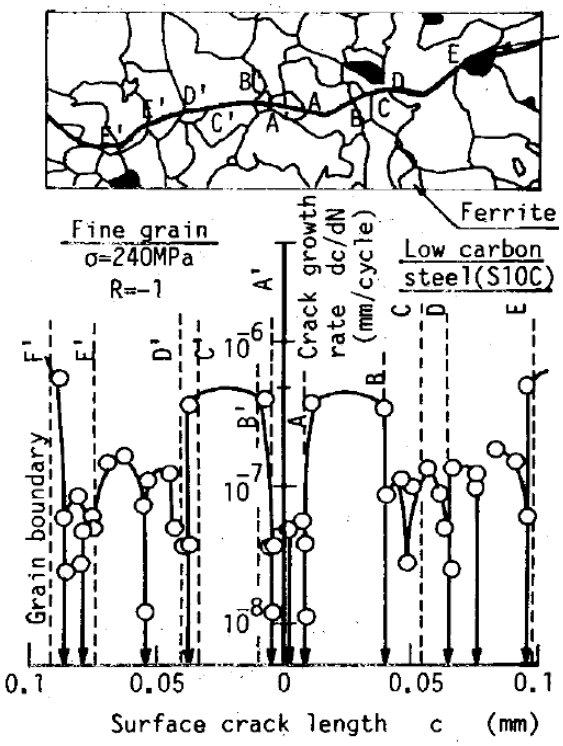


**Figure 2.4:** Example of MSC crack growth behavior (da/dN vs. crack length a) interaction with grain boundaries in a fine grain low carbon steel [22].

$\Delta K$ value [15]. At higher $\Delta K$ values, small crack growth can be accelerated due to embrittlement ahead of the crack tip [23]. In regards to the roughness of the crack path, generally speaking, the more tortuous the fracture suface, the slower the MSC growth rate. This has been shown in René88DT, a powder metal processed nickel-base superalloy, through investigation of the topography of experimentally fractured crack surfaces [24].

### 2.3.3 Experimental Time Required to Qualify Microstructures

The time required to qualify a new material or manufacturing process is significant. It can take 5-10 years to develop and implement a new Ni-base superalloy into existing products [25]. When using the previous empirical techniques in conjunction with developing and testing a new material, many fatigue specimens are required. Although these techniques are dependable, they can be very costly and time-consuming. Also, these methods cannot support design projections for microstructures that have not yet been processed or tested.

For aircraft gas turbine disk and blade applications, the maximum operating temperature is strongly dependent on the high temperature performance characteristics of Ni-base superalloys used in the hot sections (combustion chamber and turbine blades). In order to improve propulsion and fuel economy of aircraft gas turbine engines, there is a thrust to develop materials that are able to operate at higher temperatures with improved fatigue response. The ability to model and predict the effects of different microstructure attributes and tailor these to a given application is essential to accelerate development and implementation of new materials to satisfy this demand. Especially critical is the prediction of damage response at stress concentrations such as notches. Therefore, we are motivated to develop computational tools to assist materials design and modeling, including a new microstructure-sensitive fatigue notch factor that takes into account stress amplitude, mean stress, stress gradients,

microstructure length scales, deformation mechanisms and fatigue crack nucleation and microstructurally small crack growth. These tools can be used in conjunction with limited numbers of calibration and verification experiments to validate a new material or process.

## 2.4 Prior Probabilistic Approaches

In order to account for scatter in HCF, various probabilistic approaches have been developed. Most probabilistic approaches in HCF are based on weakest link theory and incorporate probability distributions such as the two parameter Weibull distribution, three parameter Weibull distribution [26], or a Gumbel distribution [27]. These approaches are typically based on the distribution of stress or strain found from experimental results or component finite element analysis.

### 2.4.1 Defect Distribution - Poisson Point Process

Most probabilistic approaches used by researchers consider the distribution of physical defects such as inclusions, pores or microcracks that contribute to failure [28–30]. Other approaches consider the distribution of microvoids [31] or microplasticity [32]. The probability of finding a fatigue-critical defect (within the bulk of the material) such as an inclusion, microcrack, etc., is usually fit to a discrete Poisson distribution of the form [33]

$$P_k = \frac{[\phi V]^k}{k!} \exp\{-[\phi V]\} \ , \tag{2.19}$$

where $P_k$ is the probability of finding $k$ fatigue critical sites in a volume domain ($V$) and $\phi V$ is the average number (expected value) of fatigue critical sites. An underlying assumption of randomness of microstructure is assumed in applying the Poisson distribution. The density per unit volume of active fatigue critical sites, $\phi$, depends on many factors including applied stress amplitude, stress ratio, grain size, internal defect size, local anisotropy, and location within a component. The density

factor $\phi$ follows a power law of the stress amplitude and can take various forms. Typically, for three-parameter Weibull statistical analyses,

$$\phi = \frac{1}{V_o} \left\langle \frac{\sigma - \sigma_L}{\sigma_o} \right\rangle^m \tag{2.20}$$

where $\sigma_L$ is the location parameter, $\sigma_o$ is the scale parameter, $m$ is the shape parameter (or Weibull slope), and $V_o$ is a reference volume. For a given value of $a$, the Macauley brackets $\langle \cdot \rangle$ indicate that $\langle a \rangle = a$ for $a > 0$ and $\langle a \rangle = 0$ for $a \leq 0$.

### 2.4.2 Weakest Link Theory

In weakest link theory a volume ($V$) is divided into $i$ number of subvolumes ($V_i$). The highly stressed volume of interest depends on the specimen geometry. For a smooth uniaxial specimen, the highly stressed volume would encompass the entire gauge section, whereas in a notched specimen it would only comprise the highly stressed volume at the notch root. For surface-dominated crack formation, the highly stressed volume of the smooth specimen would comprise the volume that is less than a given depth from the surface of the specimen. Therefore, the volume ($V$) in this case pertains to the highly stressed volume of interest. Using the above density factor $\phi$ (Equation 2.20), the probability of failure of the $i^{th}$ infinitesimal volume is given as $dP_{fi} = \phi_i \, dV_i$. Following weakest link theory [34], where an entire chain is only as strong as its weakest link, the probability of survival of volume ($V$) is equivalent to the probability that all subvolumes $dV_i$ within $V$ simultaneously survive, determined by the product of survival probabilities, i.e.,

$$P_s = \prod_{i=1}^{m} (1 - \phi_i \, dV_i) \tag{2.21}$$

where $m$ is the number of subvolumes ($m = \frac{V}{dV_i}$). Equation 2.21 assumes that there is no interaction between critically-stressed subvolumes. In other words, the distance between critical "defects" is sufficiently large enough that there is no interaction between defects. This assumption holds true in the high cycle fatigue (HCF) regime,

where heterogeneous microplasticity is sparsely scattered throughout the fatigue specimen. If the subvolume size is very small compared to volume $V$ and the density of sites $\phi$ is relatively low for low probabilities of failure, Equation 2.21 can be rewritten as

$$P_s \approx \lim_{dV_i \to 0} \left[ \prod_{i=1}^{m} (1 - \phi_i \, dV_i) \right] = \exp \left( - \int_V \phi_i \, dV_i \right) \tag{2.22}$$

Consequently, combining Equations 2.20 and 2.22 the probability of failure of the volume $V$ of the specimen becomes

$$P_f = 1 - \exp \left( - \int_V \phi_i \, dV_i \right) = 1 - \exp \left\{ -\frac{1}{V_o} \int_V \left\langle \frac{\sigma - \sigma_L}{\sigma_o} \right\rangle^m dV \right\} \tag{2.23}$$

The form of Equation 2.23 has been used extensively to model variability of fatigue strength. The value of $\sigma$ in this equation can be a maximum principal stress or equivalent stress, such as Von Mises or Tresca, that varies with position and is considered as a random parameter. Frequently, Equation 2.23 is rewritten in the form

$$P_f = 1 - \exp \left[ -\frac{kV_{th}}{V_o} \left( \frac{\sigma_{max}}{\sigma_o} \right)^m \right] \tag{2.24}$$

$$where \quad k = \left( \frac{\sum_{n=1}^{n_{Vth}} \langle \sigma - \sigma_L \rangle^m}{(\sigma_{max})^m} \right) \tag{2.25}$$

Here, the concept of an effective volume is introduced ($V_{eff} = kV_{th}$) that can be linked to size effects. The threshold volume is defined as the summation of subvolumes that contain an equivalent stress greater than or equal to a given critical stress. Typically the reference volume $V_o$, a material parameter, is merged with $\sigma_o$ to form a modified scaling parameter $\sigma_o^* = V_o^m \sigma_o$. As the volume ($V_{th}$) of critically stressed locations increases, so does the probability of failure of the whole specimen. Hence, the effective volume is indicative of size effects.

### 2.4.3 Different Derivatives of the Weibull Stress Function Approach

Various researchers have used variant forms of Equation 2.23 to determine the cumulative distribution function of a component. Some of these approaches are summarized here and are listed at the end of this section in Table 2.1 on page 35 for quick reference. Each of these techniques is an attempt to inject a stronger physical basis into the estimation of the probability of fatigue failure of a component.

#### *2.4.3.1 Strain Energy Density Approach*

Motivated by the fact that microdamage can occur at stresses below the conventional fatigue limit ($\sigma_{th} < \sigma_e$), Delahay and Palin-Luc [35] proposed using an energy approach based on the stress and strain distributions within a damage process zone. This zone is comprised of volumes in which an equivalent strain work density $W_{eq}$ is greater than a given threshold, $W_{th} = \sigma_{th}^2/E$. The resulting strain work density probability function proposed is

$$P_f = 1 - \exp\left[-\frac{1}{V_o}\int_V \left\langle \frac{W_{eq} - W_{th}}{W_o} \right\rangle^m dV\right] \ , \tag{2.26}$$

where the parameters $W_o$ and $m$ are fit to experiments. This method is a generalization of the Weibull approach that can be used for complex strain histories including in- and out-of-phase loading and multiaxial stresses. The value of $W_{eq}$ is calculated over the full loading cycle using the elastic strains after elastic shakedown of the material.

#### *2.4.3.2 Strain-Life Approach*

De Jesus et al. [36] proposed a strain-life Weibull model where the fatigue life, $N_f$, is a random variable at a constant strain amplitude, $\epsilon_a$, and vice versa. They proposed

$$P_f = 1 - \exp\left[-\left\langle \frac{log\left(N_f/N_o\right) log\left(\epsilon_a/\epsilon_{ao}\right) - x_L}{x_o} \right\rangle^m\right] \ , \tag{2.27}$$

where $N_o$ and $\epsilon_{ao}$ are threshold values and $x_L$, $x_o$, and $m$ are the Weibull parameters fit to strain-life experimental data. De Jesus et al. [36] determined the local stresses and strains near the notch root using Neuber [6] and Molski and Glinka [13] rules and modeled the elastoplastic response as a simple Ramberg-Osgood [14] stress-strain response.

#### *2.4.3.3 Critical Plane/Multiaxial Techniques*

Based on phenomenological experimental observations that fatigue cracks form and propagate on preferential "critical" slip planes, many different critical plane or multiaxial theories have been developed and studied. An extensive summary of different multiaxial fatigue models can be found in Kallmeyer et al. [37]. Most multiaxial parameters consider the combined effects of resolved shear stresses/strains and normal stresses/strains on a given plane. Theoretically, the normal stresses provide crack opening, reducing friction between crack surfaces, and resolved shear stresses support dislocation motion on the dominant slip plane under Stage I propagation. These multiaxial approaches can be incorporated into Weibull models to estimate the probability of failure of a specimen under complex, multiaxial and non-proportional loadings. A couple of these approaches are described below.

With the assumption that fatigue damage is caused by crack formation due to shear localization at the grain scale, Doudard et al. [33] proposed a Weibull model based on the distribution of microplasticity within grains. In this approach, Doudard used Kröners [38, 39] self-consistent model and Eshelby's [40] solution for a spherical inclusion to determine the local stress tensor at the grain scale. The "inclusion" in this case is the set of grains where local plasticity occurs while the "matrix" is the surrounding grains that deform elastically. The density factor, $\phi$, is a function of the resolved shear stress amplitude, $\tau_a$, and considers the distribution of activated slip of all possible slip system planes. Slip becomes active when the resolved shear

stress amplitude, $\tau_a$, is greater than a critical resolved shear stress (CRSS) value. In three-dimensional space, the density factor is integrated over all possible slip plane normal angles, $\Theta$, and takes the general form

$$\phi = \frac{1}{V_o \; S_o^m} \int (2 \; \tau_a)^m \, d\Theta \; , \tag{2.28}$$

where $m$ and $V_o S_o^m$ are material parameters. The resulting probability of failure is given as

$$P_f = 1 - exp \left[ -\frac{1}{V_o} \int_V \left( \frac{2 \; \tau_a}{S_o} \right)^m cos \left( \zeta \right) d\Theta \; dV \right] \tag{2.29}$$

This probabilistic framework accounts for scatter in HCF fatigue data through the distribution and variability in the slip system activation level and can be used for multiaxial and non-proportional loadings.

Flaceliere and Morel [41] considered a non-local multiaxial equivalent stress that is a superposition function of the resolved shear stress amplitude acting on a slip plane and the maximum hydrostatic stress, i.e.,

$$\sigma_{eq} = \sqrt{f \left( \tau_a^2 \right)} + p \; \sigma_{H,max} \tag{2.30}$$

where $\sqrt{f \left( \tau_a^2 \right)}$ is the root mean square averaged value of resolved shear stress over all slip planes and slip plane directions as defined by Papadopoulos [42], $p$ is a material constant and $\sigma_H^{max}$ is the maximum hydrostatic stress over a loading period. Therefore, the failure probability is given by

$$P_f = 1 - exp \left[ -\frac{1}{V_o} \int_V \frac{\sqrt{f \left( \tau_a^2 \right)} + p \; \sigma_{H,max}}{\sigma_o} dV \right] \tag{2.31}$$

where $V_o$ and $\sigma_o$ are typical Weibull stress function parameters.

In addition, Flaceliere and Morel [41] also studied surface and stress gradient effects in probabilistic fatigue failure through four different experimental loading conditions, including tension, torsion, plane bending and rotating bending. They used an

equivalent surface stress function based on the normalized gradient of the maximum hydrostatic stress as

$$\sigma_{eq,S}(\boldsymbol{\sigma}, G(\sigma_{H,max})) = \sqrt{f\left(\tau_a^2\right)} + p\left(1 - \beta\left\langle \frac{G(\sigma_{H,max})}{\sigma_{H,max}} \right\rangle^n\right)\sigma_{H,max} \tag{2.32}$$

where

$$G(\sigma_{H,max}) = \sqrt{\left(\frac{\partial \sigma_{H,max}}{\partial x}\right)^2 + \left(\frac{\partial \sigma_{H,max}}{\partial y}\right)^2 + \left(\frac{\partial \sigma_{H,max}}{\partial z}\right)^2}, \tag{2.33}$$

$\beta$ is a normalized hydrostatic stress intensity factor, and $n$ is a constant assumed to be equal to 1. This function was used to define a surface stress Weibull function of the form

$$P_f(\sigma_{eq,S}) = 1 - \exp\left[-\frac{1}{S_o}\int_S \frac{\sigma_{eq,S}(\boldsymbol{\sigma}, G(\sigma_{H,max}))}{\sigma_o}\, dS\right], \tag{2.34}$$

where $S_o$ is a reference surface area and $\sigma_{eq,S}(\boldsymbol{\sigma}, G(\sigma_{H,max}))$ is given by Equation 2.32. Using Equation 2.34, Flaceliere and Morel showed good correlation between the surface model framework and experimental probability of failure for a C36 mild steel and a GS52 nodular cast iron. However, the surface and volume approaches showed a significant difference in the nodular csst iron due to the presence of larger defects in the form of pores ranging in size from 50-1000 µm [41]. Considering surface/defect interactions is very important in fatigue damage of components containing sizable defects such as pores and inclusions. This will be demonstrated further in the next two sections.

#### *2.4.3.4 Inclusion/Matrix Interactions*

Processing of nickel-base superalloy materials through powder metallurgy methods can introduce pores and nonmetallic inclusions into the material. Inclusions play a dominant role in the fatigue crack formation and propagation in Ni-base superalloys [43, 44]. Also, under low cycle fatigue (LCF) conditions, surface inclusions are typically more detrimental than inclusions in the bulk [43–45]. These inclusions are often stiffer than the surrounding matrix causing local elastic incompatibility. Under

fatigue loading, this incompatibility in deformation, combined with lack of constraint near the surface on plasticity, can promote enhanced cyclic slip at the inclusion/matrix interface and fatigue crack formation [46]. The probability of initiating and propagating a crack from these inclusions has a significant effect on the overall probability of failure of Ni-base superalloy components, especially under LCF conditions.

Based on the above considerations, Pineau [47] proposed a model that uses the statistical distribution of inclusion sizes present in a PM nickel-base superalloy and a fatigue crack growth law (of the Paris-Erdogan form [48]) to determine the probability of failure of different sized components. This model considers both surface/volume effects and the formation and propagation of cracks from an inclusion to a critical size. Much like the technique described in Section 2.4.1, the inclusions are assumed to be randomly distributed throughout the matrix and observe a known size probability distribution function.

Prior to introduction of the probability framework, a few definitions of dimensions are introduced here to maintain consistency among different inclusion/matrix and inclusion/surface probabilistic approaches. The diameter (or equivalent diameter for non-spherical particles) of a spherical inclusion is $D$ and the distance that the inclusion is embedded in the matrix relative to the surface is denoted as $d$. For a fully embedded inclusion, the depth of the inclusion relative to the free surface is $h$. These dimensions are illustrated in Figure 2.5.

For a uniform size distribution of spherical inclusions randomly dispersed within a volume, the probability of any one inclusion intersecting the free surface is given as [47]

$$P_{surf}\left(D, n, S, V\right) = 1 - \left(1 - \frac{DS}{V}\right)^{nV} \tag{2.35}$$

where $D$ is the inclusion diameter, $n$ is the number of inclusions per unit volume, and $S$ and $V$ are the highly stressed surface area and volume of the specimen, respectively. For a distribution of inclusion sizes, the inclusion sizes are divided into $k$ number of

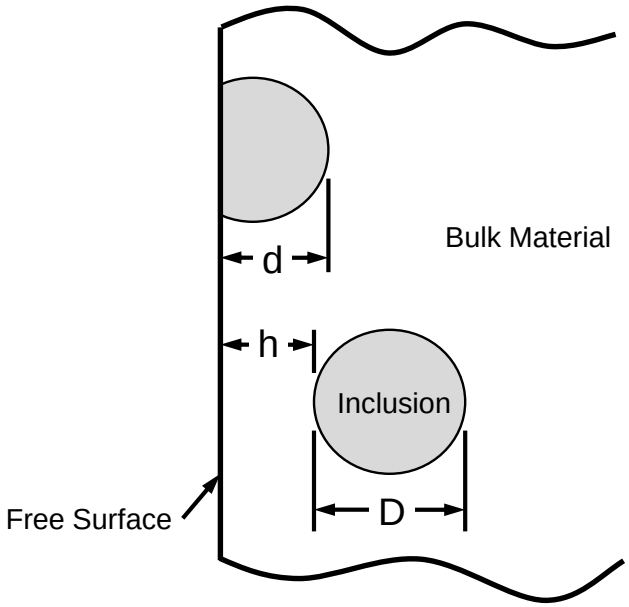


**Figure 2.5:** Definition of inclusion dimensions relative to the free surface.

classes or bins. Thus, for a given bin size ($k$), Equation 2.35 can be rewritten as the probability that an inclusion of bin size ($k$) intercepts the surface, i.e.,

$$P_{k,surf}\left(D_k, n_k, S, V\right) = 1 - \left(1 - \frac{D_k S}{V}\right)^{n_k V} \tag{2.36}$$

To consider interactions between the inclusion and the surface, Equation 2.36 is modified to incorporate the extent (depth) in which the inclusion is embedded in the material relative to the surface, via

$$P_{k,surf}\left(D_k, d, n_k, S, V\right) = \left\{1 - \left(1 - \frac{D_k S}{V}\right)^{n_k V}\right\}\left[\frac{D_k - d}{D_k}\right] \tag{2.37}$$

where $d$ is the depth in which the inclusion is embedded with respect to the surface. The form of Equation 2.37 is based on the premise that an inclusion located in the subsurface region is biased to have a higher probability of failure by virtue of fatigue crack formation and propagation process physics. Another assumption for Equation 2.37 is that $D_k \geq d$. Thus, the probability that the life of a specimen, $N_f$, is less than

a potential life, $N_o$ is given as

$$P_f\left(D_k, d, n_k, S, V;\ N_f < N_o\right) = 1 - \prod_{k=1}^{N_{classes}} \left[1 - P_{k,surf}\left(D_k, d, n_k, S, V\right)\right] \tag{2.38}$$

Substituting Equation 2.37 into Equation 2.38 gives

$$P_f = 1 - \prod_{k=1}^{N_{classes}} \left[1 - \left\{1 - \left(1 - \frac{D_k S}{V}\right)^{n_k V}\right\} \left[\frac{D_k - d}{D_k}\right]\right] \tag{2.39}$$

Here, the potential life $N_o$ as a function of flaw size $D_k$ and depth $d$ is calculated using a Paris crack growth law. A schematic of this relationship is shown in Figure 2.6. For the Paris crack growth law, a semi-elliptical initial crack shape was assumed to form during the first cycle. The major and minor axes of the initial semi-elliptical crack depend on the depth ($d$) in which the inclusion is embedded in the material relative to the surface (cf. Figure 3 in ref. [47]).

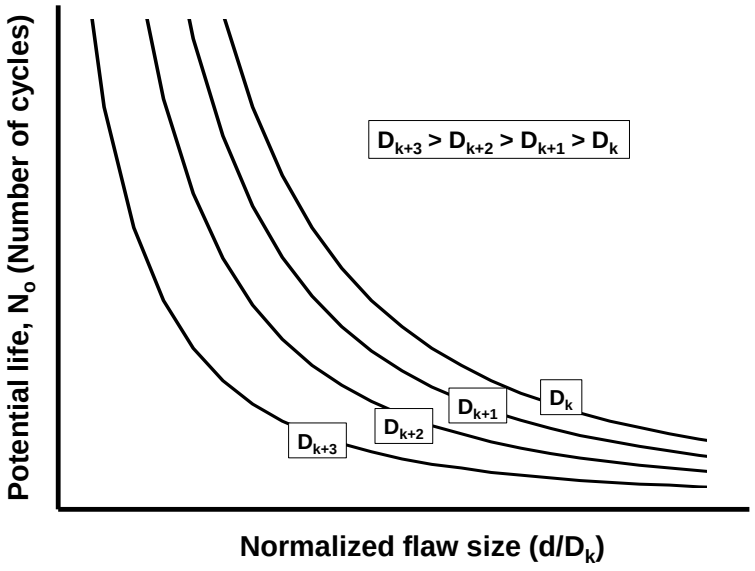


**Figure 2.6:** Number of cycles to failure as a function of the normalized position of the inclusion $d/D_k$ for different size classes $D_k$. After ref. [47].

Using this approach, Pineau [47] estimated the probability of failure of three different sized components made from René 95, (from largest to smallest) corresponding to a large disc size, a small disc size, and a specimen size. Results similar to that

shown in Figure 2.7 were found which indicates that the probability of failure of a component is highly size dependent. Therefore, a strain-life approach in which the fatigue crack initiation in a large component is estimated through the failure of a small smooth specimen may not be sufficient. Figure 2.8 shows that the life-limiting inclusion size causing crack initiation increases with the size of the component. This is expected because the probability of finding a larger-sized inclusion increases with the size of the component. Considering the results shown in Figures 2.7 and 2.8, it is easy to see the importance in close control of the manufacturing process in order to limit the size and frequency in which nonmetallic inclusions are present in the microstructure.

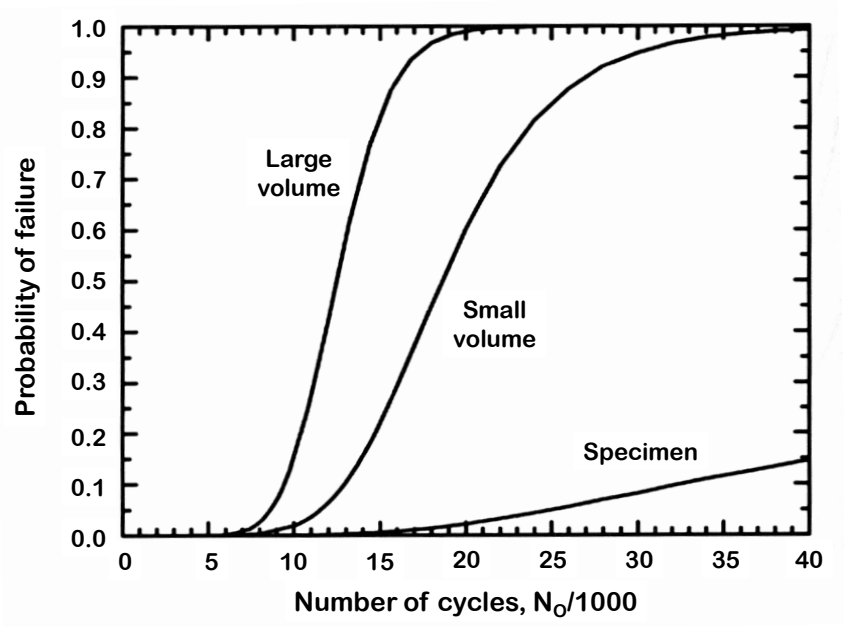


**Figure 2.7:** Variation of probability of failure versus the number of cycles for different sized specimens of René 95 [49].

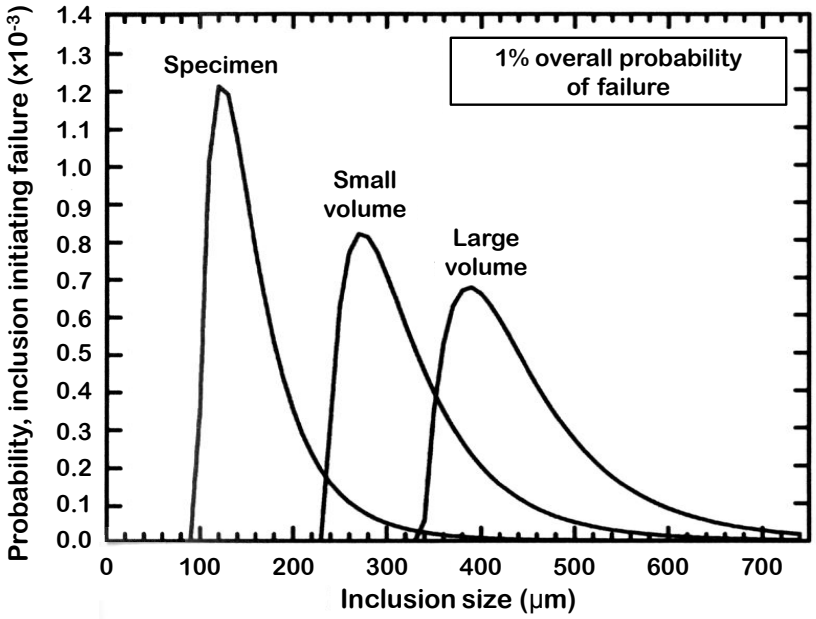


**Figure 2.8:** Variation of the probability of failure versus life-limiting inclusion size for different sized specimens of René 95 [49].

An extension of the above approach to include the micro-mechanics of inclusion/matrix deformation was proposed by Deyber et al. [50]. In addition to using the statistical distribution of particle size, Deyber et al. [50] estimated the probability of failure based on deterministic inclusion/matrix micro-mechanisms of crack initiation and propagation. Two different fatigue crack initiation modes were considered. Transgranular stage I fatigue crack initiation along intense slip bands was observed in larger grain sizes, while fatigue crack formation at second phase particles was observed in grain sizes smaller than about 10 μm [51]. For the formation of cracks at particle/matrix interfaces, an equivalent Weibull stress function was proposed [50] as

$$P_f(\sigma_d) = 1 - exp\left(-\left[\frac{\Sigma_1 + \beta\left\langle\sigma_{eq} - \sigma_y\right\rangle}{\sigma_o}\right]^m\right) \tag{2.40}$$

where $\Sigma_1$ is the maximum principal stress, $\beta$ is the particle shape factor, $\sigma_{eq}$ is the equivalent Von Mises stress, $\sigma_y$ is the yield stress, and $\sigma_o$ is a scaling parameter. Failure is considered when the numerator in Equation 2.40 reaches a critical decohesion

stress, i.e., $\sigma_d = \Sigma_1 + \beta \langle \sigma_{eq} - \sigma_y \rangle$. Following crack initiation, a micro-crack propagation law based on the Tomkins model [52] was used to model crack propagation, i.e.,

$$\frac{da}{dN} = \omega \ a \ , \qquad \text{where } \omega = \frac{\Delta\epsilon_p \sigma^2 \pi^2}{32T^2} \left(1 + \frac{\Delta\sigma^2\pi^2}{32T^2}\right) \tag{2.41}$$

Here, $T$ is the ultimate tensile stress in the plastic zone of the crack. From this model, the probability that a particle of a potential diameter, $D_o$, would propagate in a potential number of cycles ($N_o$) was determined. The probability of a given propagation life is therefore equivalent to the probability of finding a particle of size greater than the potential diameter, $D_o$. The overall global probability of survival was equal to the product of the probabilities of survival of particles at the surface ($surf$), subsurface ($subsurf$), and within the bulk ($bulk$) of the material. Thus, the global probability of failure ($P_f = 1 - P_{survival}$) is given by

$$\begin{aligned} P_f = 1 - \Bigg\{ & \prod_{n=1}^{Nel,surf} \left[(1 - P_f(\sigma_d) P(D \geq D_o))^{Np,surf}\right] \\ & * \prod_{n=1}^{Nel,subsurf} \left[(1 - P_f(\sigma_d) P(D \geq D_o))^{Np,subsurf}\right] \\ & * \prod_{n=1}^{Nel,bulk} \left[(1 - P_f(\sigma_d) P(D \geq D_o))^{Np,bulk}\right] \Bigg\} \end{aligned} \tag{2.42}$$

where $P_f(\sigma_d)$ is given by Equation 2.40, and $Npart$ and $Nel$ are the number of particles contained in the computational mesh elements, repectively, in each location (surface, subsurface, and bulk).

#### *2.4.3.5 Inclusion/Surface Considerations*

As stated previously, proximity of inclusions to the surface is very important in designing against low cycle fatigue failure of powder metal nickel-base superalloys. Another extension to Pineau's [47] framework was introduced by de Bussac and Lautridou [53]. They considered the probability for an individual particle to have a depth greater than

a critical depth $d_c$, i.e.,

$$P\left(d > d_c\right) = \frac{S(D - d_c)}{V} \tag{2.43}$$

Considering particles of different size classes (much like that described above) and imposing weakest link statistics over each class, the probability that the number of cycles to failure of the entire component ($N_f$) is less than a potential life ($N_o$) is given as

$$P_f\left(N_f < N_o\right) = 1 - \prod_{k=1}^{N_{classes}} \left[\exp\left\{-n_k S\left(D_k - d_c\right)\right\}\right] \tag{2.44}$$

In a later publication, de Bussac [45] proposed that there was competition between the largest defect at the free surface and the largest defect within the bulk of the material. The total probability of failure of a component was proposed to be equal to the product of the individual probabilities of each failure mechanism, i.e.,

$$P_f = 1 - \left\{\left[1 - P_S\right]\left[1 - P_V\right]\right\} \tag{2.45}$$

where $P_S$ and $P_V$ are the probabilities of surface and bulk volume failure, respectively.

This probabilistic model was evaluated by using a large amount of LCF data of N18, a PM nickel-base superalloy, which is used for high-temperature jet engine disk applications. The LCF fracture surfaces were examined through scanning electron microscopy (SEM) to determine the size of the life-limiting defect as a function of the depth ($h$) in which the defect was embedded relative to the free surface (cf. Figure 2.9). The typical defect diameters found from the LCF fracture surfaces were in the 20-100 μm range [45]. From Figure 2.9 it is easy to see that there is a "sweet spot" at around 5 μm from the surface in which an inclusion will cause the most damage. This can be concluded because the critical defect size at this depth is the smallest. Thus, the near-surface initiation is more damaging than surface initiation. This can be attributed to the fact that a crack formed beneath the surface will propagate through the surface and effectively introduce a larger surface defect. Also, the critical defect size causing fatigue crack initiation increases as a function of depth from the

surface up to a size of about 100 µm. At depths larger than this transition depth (100 µm), the critical defect size is relatively constant [45]. This indicates that there is a significant surface effect on the probability of forming a crack in this PM Ni-base superalloy.

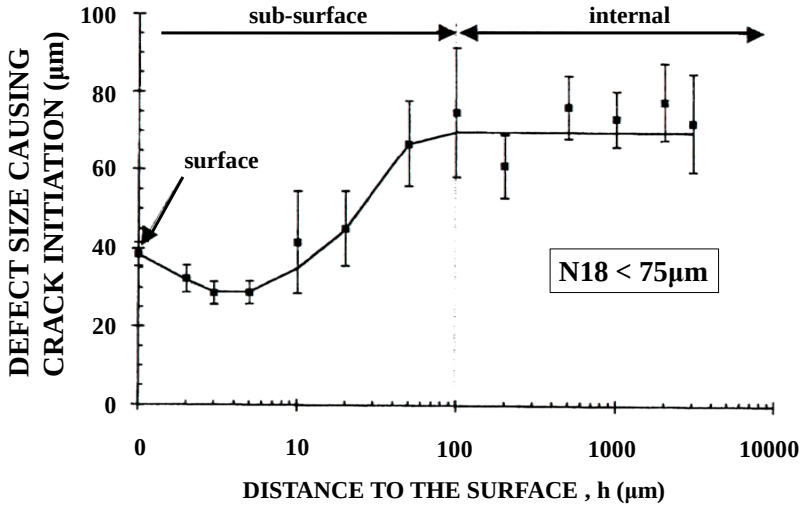


**Figure 2.9:** Crack initiation size versus distance from surface for a PM nickel-base superalloy N18 [45].

Similarly, Jha et al. [54] noticed a competition between mean-controlling and life-limiting probability density functions over different stress amplitudes in experiments on IN100, a Ni-base superalloy of interest. They categorized the total fatigue lifetime as a superposition of the surface-dominated (life-limiting) and interior-dominated (mean-controlling) mechanisms in fatigue. Also, they noted increased separation between these two populations with decreasing applied stress amplitude (cf. Figure 2.10). They proposed the total probability function as

$$P_{f,t}(x) = P_{surf} f_{surf}(x) + P_{internal} f_{internal}(x) \tag{2.46}$$

where $f_{(*)}(x)$ is the probability density function of each mechanism (*) and $P_{(*)}$ is the weighted probability of occurrence of each individual response. Note that in Equation

2.46, $P_{surf} + P_{internal} = 1$.

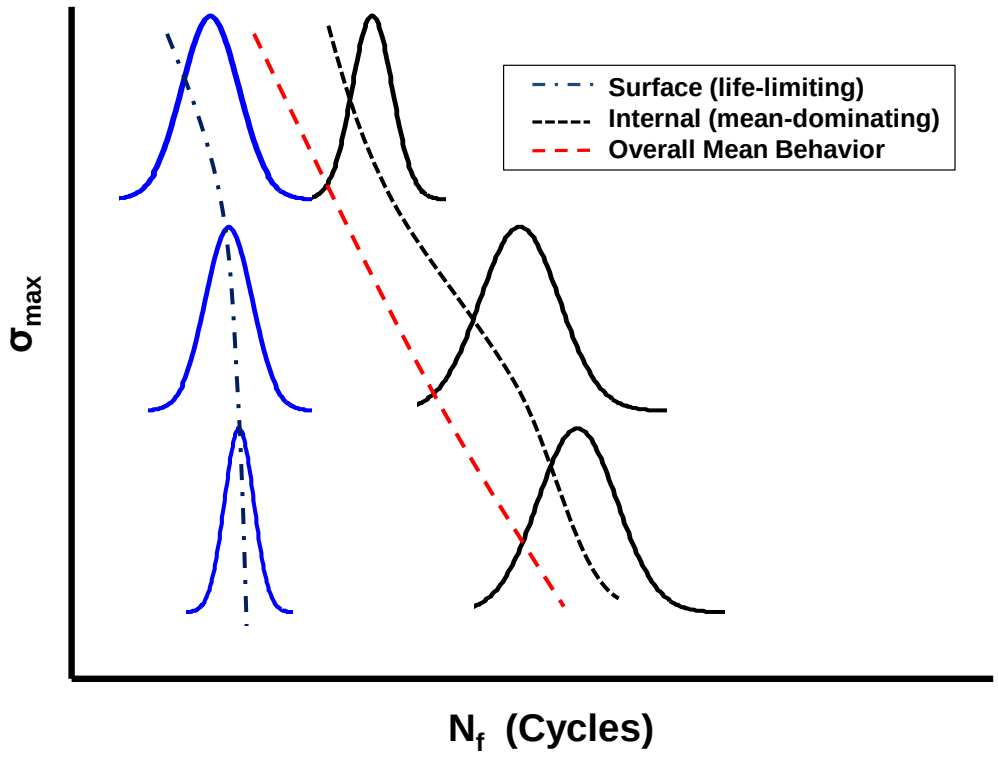


**Figure 2.10:** Schematic representation of variability in lifetime of a PM nickel-base superalloy IN100. After ref. [54].

**Table 2.1:** Some Expressions for Probabilistic Life Approaches

| Authors | CDF Function | Eqn. | Description | Ref. |
|---|---|---|---|---|
| Weibull | $P_f = 1 - exp\left[-\frac{1}{V_o}\int\limits_V \left\langle \frac{\sigma - \sigma_L}{\sigma_o} \right\rangle^m dV\right]$ | (2.23) | Weibull stress function | [26, 34] |
| Delahay, Palin-Luc | $P_f = 1 - exp\left[-\frac{1}{V_o}\int\limits_V \left\langle \frac{W_g - W_{th}}{W_o} \right\rangle^m dV\right]$ | (2.26) | Strain energy density function | [35] |
| De Jesus, Pinto, Fernández-Canteli, Castillo, Correia | $P_f = 1 - exp\left[-\left\langle \frac{log\left(\frac{N_f}{N_o}\right) log\left(\frac{\epsilon_a}{\epsilon_{ao}}\right) - x_L}{x_o} \right\rangle^m\right]$ | (2.27) | Strain-life Approach | [36] |
| Doudard, Hild, Calloch | $P_f = 1 - exp\left[-\frac{1}{V_o}\int\limits_V \left(\frac{2\ \tau_a}{S_o}\right)^m cos\left(\zeta\right) d\Theta\ dV\right]$ | (2.29) | CRSS function | [33] |
| Flaceliere, Morel | $P_f = 1 - exp\left[-\frac{1}{V_o}\int\limits_V \frac{\sqrt{f\left(\tau_a^2\right)} + p\ \sigma_{H,max}}{\sigma_o} dV\right]$ | (2.31) | Multiaxial equivalent stress function | [41] |
| Flaceliere, Morel | $P_f = 1 - \exp\left[-\frac{1}{S_o}\int\limits_S \frac{\sigma_{eq,S}(\boldsymbol{\sigma}, G(\sigma_{H,max}))}{\sigma_o}\ dS\right]$ | (2.34) | Surface and gradient of hydrostatic stress function | [41] |
| Pineau | $P_f = 1 - \prod\limits_{k=1}^{N_{classes}} \left[1 - P_{k,surf}\left(D_k, d, n_k, S, V\right)\right]$ | (2.38) | Statistical distribution of inclusions and crack growth law | [47] |
| Deyber, Alexandre, Vaissaud, Pineau | $P_f = 1 - exp\left(-\left[\frac{\Sigma_1 + \beta\left\langle\sigma_{eq} - \sigma_y\right\rangle}{\sigma_o}\right]^m\right)$ | (2.40) | Critical stress to form cavity in inclusion/matrix material | [50] |
| de Bussac(1994); Jha, Caton, Larsen(2008) | $P_{f,t}(x) = P_{surf} f_{surf}(x) + P_{internal} f_{internal}(x)$ | (2.45, 2.46) | Competing surface and internal fatigue mechanisms | [45, 54] |

## 2.5 Summary

This chapter provides the background information for this thesis related to statistical approaches to size effects of notches. Stress- and strain-life approaches to notch fatigue analysis were introduced. Most of these approaches require many experiments to phenomenologically fit a number of microstructure constants. These approaches do not take into account the microstructure scale fatigue mechanisms when describing material variability and size effects. Also, the time required to determine these experimental fits necessitates the use of computational and probabilistic strategies and experimental verification in parallel to improve fatigue notch analyses and confidence ratios. Many probabilistic schemes were described in this section, most of which are derivatives of the Weibull stress function [26, 34]. Each probabilistic strategy is an attempt to inject a stronger physical basis into the estimation of the probability density function. When considering the different micro-mechanisms for fatigue, one extremely important takeaway is that the traditional approach to fatigue variability as the fatigue distribution about the mean-lifetime behavior may not be sufficient in view of the extreme value nature of the problem. Also, very few of these studies, if any, have attempted to combine computational materials design tools with probabilistic approaches. A probabilistic approach based on the physical mechanisms of fatigue damage formation and propagation and the competition between these mechanisms should be used for all physically based models. Therefore, in the following chapters a probabilistic model based on the physical mechanisms of fatigue crack formation and growth is introduced to try to improve fatigue notch response prediction and modeling.

# CHAPTER III

# MATERIAL MODELING

## 3.1 Introduction

Nickel-base superalloys are processed through various techniques, depending on the end product characteristics and microstructure desired. The two means of preparing billets are casting and powder metallurgy techniques. These billets can be further processed through hot-isostatic pressing, extrusion, forging, machining and final protective coating application. Over the years, casting techniques have drastically improved the creep characteristics of Ni-base superalloys. The advent of directionally solidified and single-crystal superalloys greatly suppress or eliminate the grain boundary diffusional creep mechanism at higher temperatures. These types of casting processes allow for preferential orientation of the crystals to maximize fatigue resistance in that orientation.

For components made of many different chemical constituents, powder metallurgy processes are preferred in order to reduce individual phase segregation. The use of very fine powder can help decrease the number of nonmetallic inclusions and pores, which have a significant effect on fatigue crack nucleation and crack growth, as evidenced in the previous chapter. Powder metallurgy has also been used to process very fine-grained microstructures with very high strength and structural homogeneity. These microstructures are typically used for components operating in the intermediate temperature ($\sim$ 650°C) regime such as disks, spacers and seals. The overall manufacturing process to create a PM nickel-base superalloy is summarized in Figure 3.1.

Nickel has a face-centered cubic (FCC) crystalline structure that is stable from

room temperature to its melting point. Nickel-base superalloys are often strengthened through solid solution strengthening of the $\gamma$ matrix and precipitation strengthening using $L1_2$ (ordered FCC) $\gamma^{'}$ precipitates in the austenitic $\gamma$ matrix. Typically there can be three different size distributions of $\gamma^{'}$ precipitates ($\approx$1.0, $\approx$0.1, and $\approx$0.01 $\mu$m in diameter), often referred to as primary, secondary, and tertiary $\gamma^{'}$ precipitates, respectively. The larger primary $\gamma^{'}$ precipitates form during the first step of heat treatment (for subsolvus heat treatment) and typically form high-angle grain boundaries between the primary $\gamma^{'}$ precipitates and the $\gamma$ matrix. The secondary and tertiary precipitates form during cooling and subsequent aging. These two precipitates are coherent with the $\gamma$ matrix. Due to the unique deformation mechanisms in the ordered $Ni_3Al$ precipitates, these alloys display an anomalous yield strength with increasing temperature, up to about 800°C.

One of the limiting factors in fatigue performance in PM nickel-base superalloys is the presence of nonmetallic ceramic inclusions that serve as crack initiation sites [43, 44]. These inclusions are often introduced to the molten metal, due to erosion or spalling of the crucible, tundish or nozzle, prior to the gas atomization process used to create the powder [49, 53]. To reduce the size and frequency of these particles, the metal powder is repeatedly sieved with screens of progressively finer mesh size to remove the largest harmful oxide particles [49, 53]. This screening process also removes the largest metal particles which reduces usable metal particle yield and increases overall production cost.

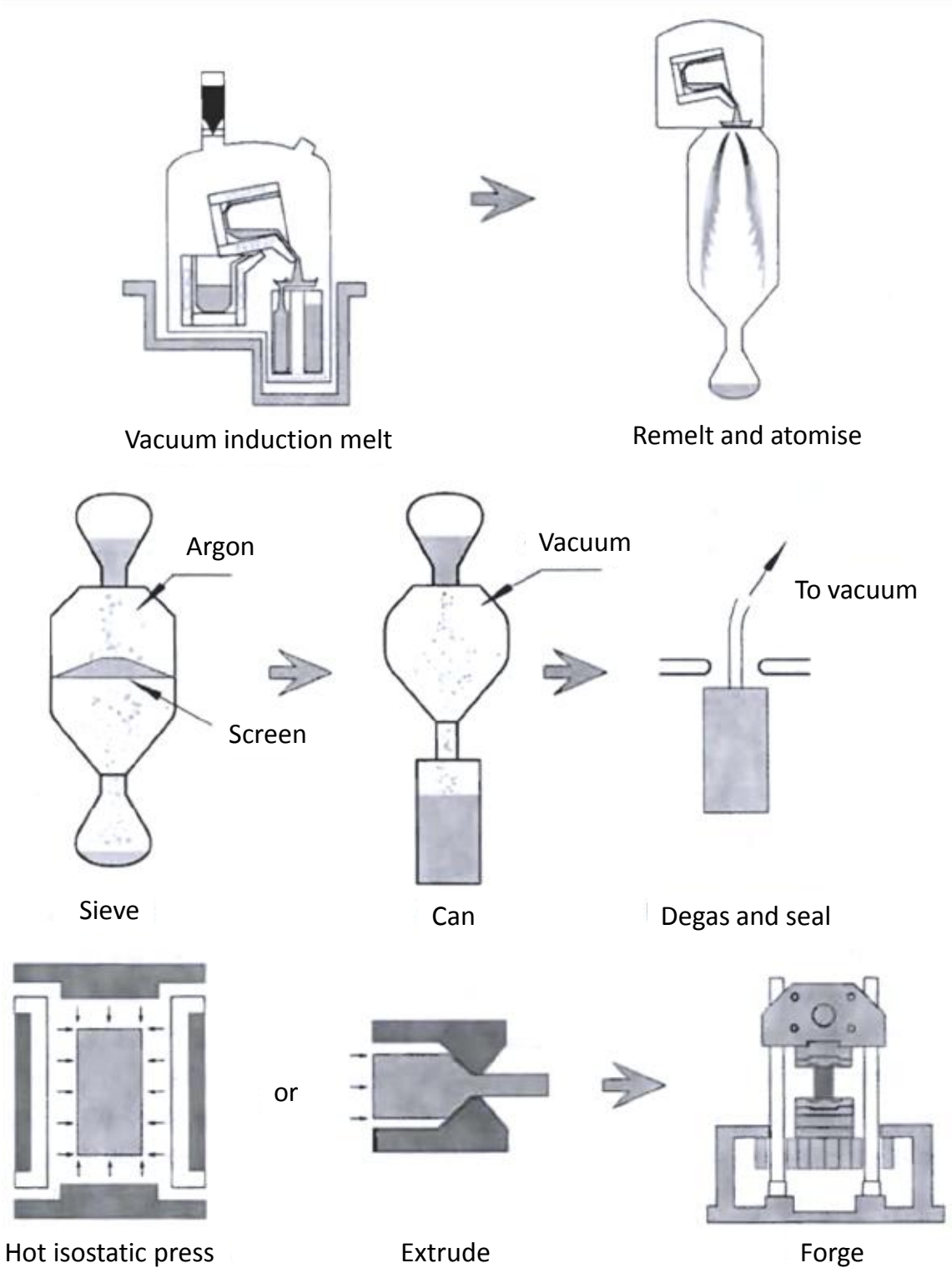


**Figure 3.1:** Typical manufacturing process of a PM nickel-base superalloy [49].

## 3.2 Key Features for Microstructures of Consideration

In this study, two different families of the Ni-base superalloy Inconel 100 (IN100) will be modeled. IN100 was first developed in cast form in the early 1960s and has been significantly improved due to PM processing. The use of PM processing is appropriate when considering the chemically complex microstructure with over 10 constituent elements (ref. Table 3.1). IN100 is used extensively for intermediate temperature ($\sim 650°C$) applications such as turbine engine disks due to its enhanced strength, creep, fatigue, and corrosion resistance at these temperatures. The two different microstructures that will be studied here are the fine grain (FG) sister disk and the coarse grain (CG) super weak microstructures, as outlined in Milligan et al. [55]. These two microstructures represent the bounds of subsolvus and supersolvus microstructures. These microstructures were thoroughly characterized through the work of Wusatowska-Sarnek and coworkers [56, 57].

**Table 3.1:** Chemical Constituents of IN100 and Its Phases (Weight Percent) [58]

| Alloy/Phase | Ni | Al | Cr | Co | Mo | Ti | V | Fe | C | Zr | B |
|---|---|---|---|---|---|---|---|---|---|---|---|
| IN100 | 56.0 | 4.9 | 12.3 | 18.3 | 3.3 | 4.3 | 0.70 | 0.10 | 0.06 | 0.02 | 0.02 |
| $\gamma$ matrix | 38.7 | 2.25 | 24.5 | 27.8 | 5.73 | 0.93 | 0.05 | | | | |
| $\gamma^{'}$ ppt | 71.8 | 7.06 | 2.59 | 8.94 | 1.42 | 6.97 | 1.23 | | | | |

Following the forging process, the PM-processed Ni-base superalloy is heat-treated to create the final desired microstructure. The microstructure features differ depending on the heat treatment process. A typical heat treatment for IN100 consists of a subsolvus (at 1143°C) or supersolvus (at 1205°C) heat treatment for 2 hours, followed by subsequent stabilization (at 982°C) for 1 hour and aging (at 732°C) for 8 hours [58], as shown in Figure 3.2. The $\gamma^{'}$ solvus temperature, or the temperature at which the phase transformation of $\gamma \rightarrow (\gamma + \gamma^{'})$ occurs upon cooling, is approximately 1185°C. Often Ni-base superalloys are characterized based on whether the first heat treatment is above or below the solvus temperature (respectively, supersolvus and

subsolvus). The heat treatment is selected based on the desired material properties of the end product. The strength of IN100 is highly dependent on a number of inter-related microstructure features including the volume fraction, particle size, particle distribution, and grain sizes of the $\gamma$ matrix and $\gamma^{'}$ precipitate phases.

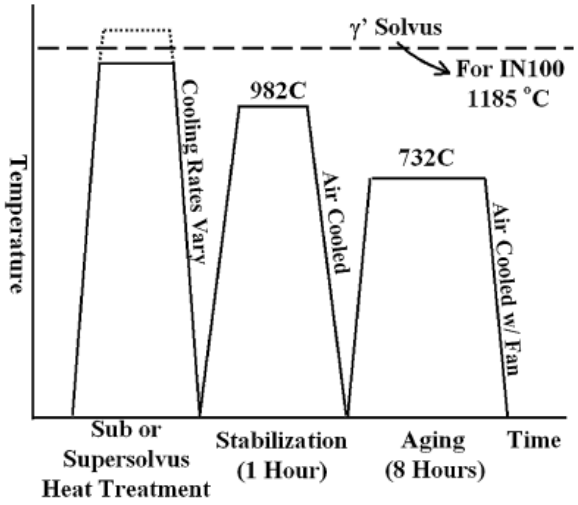


**Figure 3.2:** Typical heat treatment for subsolvus and supersolvus IN100 microstructures [58].

Other minor phases are present in these alloys including carbides and borides. These phases are present in very low quantities (total volume fraction equal to about 1.6 %). Elongated carbides of the $M_{23}C_6$ type tend to form at the grain boundaries while smaller spherical particles of MC type are more predominantly located within the grain structure. Although it is possible to form topologically close-packed (TCP) phases $\sigma$, $\mu$, and Laves phases in IN100, the exposure time required to form such phases is longer than the typical processing regime of these microstructures [57]. Therefore, the TCP phases are not present in the IN100 microstructures used in this study.

### 3.2.1 Fine Grain IN100

The fine grain IN100 used in this study is processed using a subsolvus heat treatment. The primary $\gamma^{'}$ precipitates created in this step help control the grain size of the $\gamma$

matrix through grain boundary pinning. As stated previously, the secondary and tertiary $\gamma'$ precipitates are formed during subsequent cooling and aging processes. An example of a fine grain IN100 microstructure is shown in Figure 3.3. Note that the size of the primary $\gamma'$ is of the same order of magnitude as the $\gamma$ matrix grain size. The key microstructure details of the subsolvus fine grain IN100, including size and volume fractions of each phase, are summarized in Table 3.2.

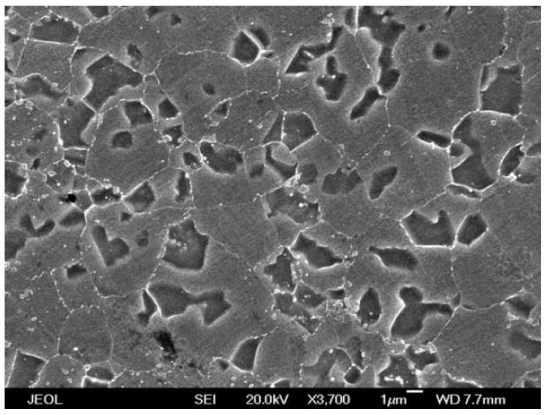


(a) Grain structure showing $\gamma$ matrix (lighter gray) and primary $\gamma'$ precipitate (darker gray) distribution [56].

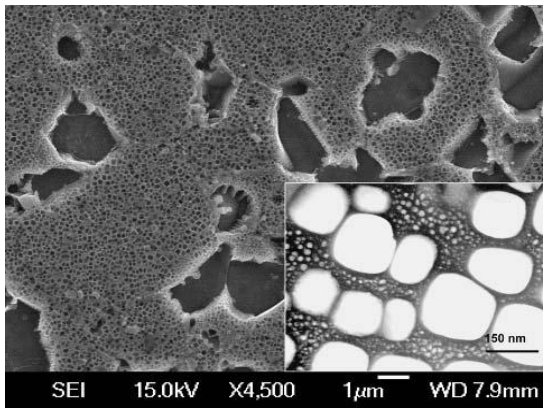


(b) Grain structure showing closer view of $\gamma$ matrix (lighter gray) and primary $\gamma'$ precipitate (darker gray) distribution. The inset is a dark-field TEM image which shows morphology of cuboidal secondary (large white) and tertiary (small white dots) $\gamma'$ distribution [57].

**Figure 3.3:** SEM and TEM images of a fine grain subsolvus IN100 microstructure.

### 3.2.2 Coarse Grain IN100

Coarse grain IN100 microstructures are created through supersolvus heat treatment. During this heat treatment the primary $\gamma'$ are dissolved, resulting in a bimodal distribution of precipitates. An example of a coarse grain IN100 is shown in Figure 3.4. As seen in these SEM images, the coarse grain IN100 has a bi-modal distribution of secondary and tertiary $\gamma'$ precipitates. These precipitates are formed in the cooling and aging processing steps after the supersolvus heat treatment. The key microstructure details of the supersolvus coarse grain IN100 are summarized in Table 3.2.

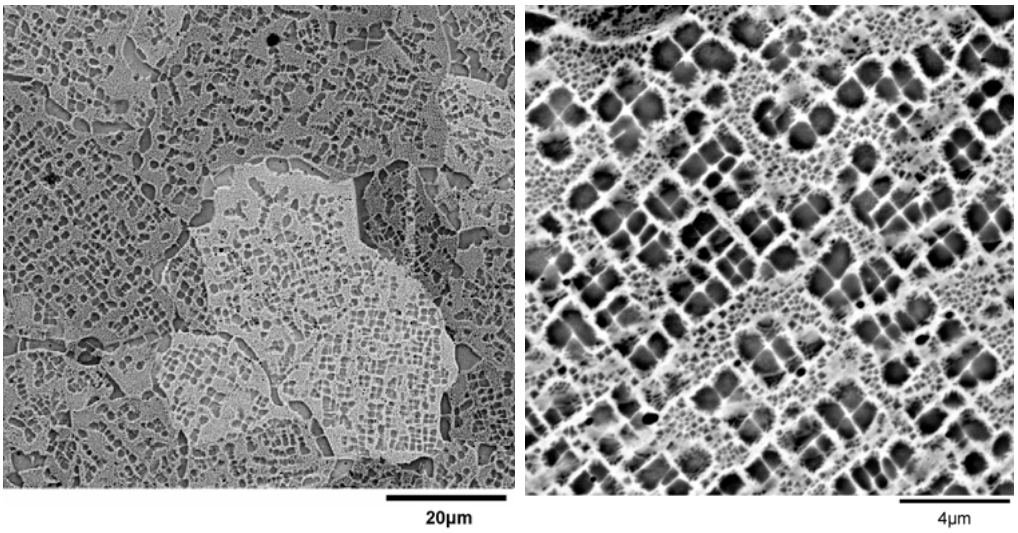


(a) Grain structure showing secondary $\gamma^{'}$ distribution.

(b) Grain structure showing secondary and tertiary $\gamma^{'}$ distribution.

**Figure 3.4:** SEM images of a coarse grain supersolvus IN100 microstructure [24].

**Table 3.2:** Microstructural Details for IN100 [55]

| Material | Primary $\gamma^{'} f_{p1}$ | Secondary $\gamma^{'} d_2$(nm) | Secondary $\gamma^{'} f_{p2}$ | Tertiary $\gamma^{'} d_3$(nm) | Tertiary $\gamma^{'} f_{p3}$ | Grain $d_{gr}$(μm) |
|---|---|---|---|---|---|---|
| Coarse Grain (CG) | - | 340 | 0.46 | 11 | 0.137 | 34 |
| Fine Grain (FG) | 0.25 | 109 | 0.32 | 21 | 0.024 | 4.2 |

## 3.3 Crystal Plasticity Model

To model the complex behavior of the coarse and fine grain IN100 microstructures, a fully three-dimensional computational crystal plasticity model is used. The crystal plasticity model used here follows that of Przybyla and McDowell [59]. This model is a rate-dependent, microstructure-sensitive model used to capture the first order effects on the macroscopic stress-strain response due to grain size, $\gamma^{'}$ precipitate size distribution and $\gamma^{'}$ precipitate volume fraction. These microstructure features all greatly affect the material and fatigue response of nickel-base superalloys. This model was calibrated to complex cyclic stress-strain data of multiple microstructure variations at an operating temperature of 650°C with and without hold times [1].

Physically-based hardening models are used based on dislocation/precipitate interactions evidenced from experiments.

The kinematics of deformation are based on the fundamental multiplicative decomposition of the deformation gradient, $\mathbf{F}$, into an elastic portion, $\mathbf{F^e}$, and a plastic portion, $\mathbf{F}^p$, i.e. $\mathbf{F} = \mathbf{F}^e \cdot \mathbf{F}^p$. The elastic portion, $\mathbf{F}^e$ takes into account the elastic lattice distortion and rotation and $\mathbf{F}^p$ addresses dislocation glide along crystallographic slip planes. The elastic Green strain and second Piola-Kirchhoff stress tensor are denoted by $\mathbf{E}^e = \frac{1}{2}\left(\mathbf{F}^{eT} \cdot \mathbf{F}^e - 1\right)$ and $\boldsymbol{\sigma}^{pk2} = \det\left(\mathbf{F}^e\right)\mathbf{F}^{e-1} \cdot \boldsymbol{\sigma} \cdot \mathbf{F}^{e-T}$, respectively. Assuming small elastic strains, ($\boldsymbol{\epsilon}^e \approx \mathbf{E}^e$), the linear hyperelastic relation is given by $\boldsymbol{\sigma}^{pk2} = \mathbf{C} : \mathbf{E}^e$, where $\mathbf{C}$ is the fourth rank anisotropic elasticity tensor of the crystal.

In the reference configuration, the slip plane unit normal vector $\mathbf{m}_o^{(\alpha)}$ and slip direction unit vector $\mathbf{s}_o^{(\alpha)}$ for each slip system ($\alpha$) frame the plastic velocity gradient in the intermediate configuration via

$$\mathbf{L}^p = \dot{\mathbf{F}}^p \cdot \mathbf{F}^{p-1} = \sum_{\alpha=1}^{N_{slip}} \dot{\gamma}^{(\alpha)} \left(\mathbf{s}_o^{(\alpha)} \otimes \mathbf{m}_o^{(\alpha)}\right) \tag{3.1}$$

where $\dot{\gamma}^{(\alpha)}$ is the shearing rate for each slip system ($\alpha$). The slip system normals and directions in the current configuration are respectfully related to that in the reference configuration $\mathbf{s}^{(\alpha)} = \mathbf{F}^e \cdot \mathbf{s}_o^{(\alpha)}$ and $\mathbf{m}^{(\alpha)} = \mathbf{m}_o^{(\alpha)} \cdot \mathbf{F}^{e-1}$. Thus, the resolved shear stress on each slip system is $\boldsymbol{\tau}^{(\alpha)} = \boldsymbol{\sigma} : \left(\mathbf{s}^{(\alpha)} \otimes \mathbf{m}^{(\alpha)}\right)$, where $\boldsymbol{\sigma}$ is the Cauchy stress.

The shearing rate on each slip system is given by a two-term potential flow rule [60]

$$\dot{\gamma}^{(\alpha)} = \left[\dot{\gamma}_1 \left\langle \frac{\left|\tau^{(\alpha)} - \chi^{(\alpha)}\right| - \kappa^{(\alpha)}}{D^{(\alpha)}} \right\rangle^{n_1} + \dot{\gamma}_2 \left\langle \frac{\left|\tau^{(\alpha)} - \chi^{(\alpha)}\right|}{D^{(\alpha)}} \right\rangle^{n_2}\right] \operatorname{sgn}\left(\tau^{(\alpha)} - \chi^{(\alpha)}\right) \tag{3.2}$$

Here $\dot{\gamma}_1$ and $\dot{\gamma}_2$ are constants, $n_1$ and $n_2$ are flow exponents, $\kappa^{(\alpha)}$ is the threshold stress, and $D^\alpha$ is an average drag resistance. The first term in Equation 3.2 captures the dominant cyclic behavior with the threshold stress playing the role of yield strength. The second term incorporates the effect of thermally activated creep at lower stresses. At lower stresses, the first term may not be active, and the dominant flow mechanisms

are controlled by heterogeneous partial dislocation dissociation and matrix faulting. The use of a two term flow rule is necessary to model complex cyclic stress-strain histories.

The anomalous yield behavior of nickel base superalloys can be attributed to the unique deformation mechanisms in its constituent phases. As mentioned previously, the $\gamma$ matrix is an FCC crystalline lattice. At lower temperatures, dislocation motion within the matrix is often limited to planar slip along the 12 octahedral slip planes $\langle 110 \rangle$ $\{111\}$, which is typical for the FCC lattice structure. At higher temperatures, macroscopic slip traces have shown evidence of an additional activation of 6 "cube" slip systems $\langle 110 \rangle$ $\{001\}$. Upon further investigation through transmission electron microscopy (TEM), Bettge and *Ö*sterle [61] discovered that this cube slip was actually due to thermal activation of "zig-zag" cross slip of screw dislocations. As the screw dislocations migrate through $\gamma'$ precipitate channels, they are blocked at the $\gamma/\gamma'$ interface causing the zig-zag cross slip mechanism (cf. Figure 3.5). Thus, at higher temperatures, cross slip creates complicated forest dislocation interaction which increases the dislocation density and restricts further motion of mobile dislocations. Therefore, we employ two internal state variables (ISVs) to describe the microstructure evolution of IN100, namely dislocation density, $\rho^{(\alpha)}$, and the back stress, $\chi^{(\alpha)}$. Based on the above considerations, we model 12 octahedral slip systems $\langle 110 \rangle$ $\{111\}$ and 6 "cube" slip systems $\langle 110 \rangle$ $\{001\}$ in IN100.

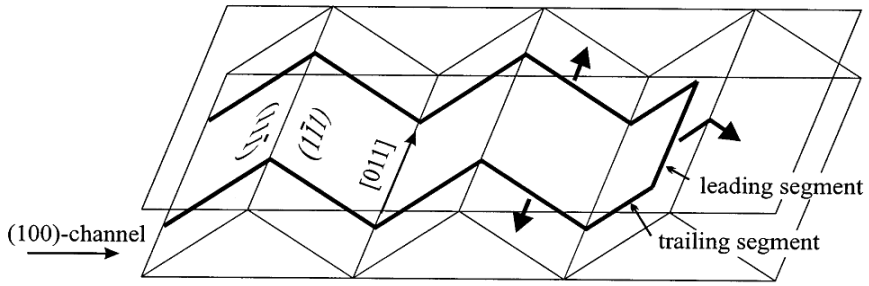


**Figure 3.5:** Schematic of zig-zag $\{111\}$ slip in the $\{100\}$ $\gamma'$ channels [61].

The hardening of the threshold stress on each slip system is assumed to follow the Taylor relation

$$\kappa_{\lambda}^{(\alpha)} = \kappa_{o,\lambda}^{(\alpha)} + \alpha_t \ \tilde{\mu} \ \tilde{b} \ \sqrt{\rho_{\lambda}^{(\alpha)}} \tag{3.3}$$

In Equation 3.3, $\lambda$ represents either octahedral or cube slip systems and $\rho^{(\alpha)}$ is the dislocation density on each slip system. The shear modulus $\tilde{\mu}$ follows a rule of mixtures $\tilde{\mu} = (f_{p1} + f_{p2} + f_{p3})\,\mu_{\gamma'} + f_m \mu_m$, where $f_{p1}$, $f_{p2}$, $f_{p3}$, and $f_m$ are the volume fractions of the primary $\gamma^{'}$, secondary $\gamma^{'}$, tertiary $\gamma^{'}$ and matrix phases respectively, and $\mu_{\gamma'}$ and $\mu_m$ are the shear moduli of the precipitate and matrix phases. Similarly, an effective burgers vector is employed, $\tilde{b} = (f_{p1} + f_{p2} + f_{p3})\ b_{\gamma'} + f_m\ b_m$, where $b_{\gamma'}$ and $b_m$ are the burgers vectors of the $\gamma^{'}$ precipitates and matrix, respectively. Also, $\alpha_t$ is a statistical coefficient that accounts for spatial arrangements of the dislocation population. The initial critical resolved shear stress (CRSS), $\kappa_{o,\lambda}^{(\alpha)}$ is based on the work of Reppich and co-workers [62, 63] and is given as:

$$\begin{aligned}
\kappa_{o,\mathrm{oct}}^{(\alpha)} &= \left[\left(\tau_{o,\mathrm{oct}}^{(\alpha)}\right)^{n_\kappa} + \Psi_{\mathrm{oct}}\left(f_{p1}, d_2, f_{p2}, d_3, f_{p3}\right)^{n_\kappa}\right]^{1/n_\kappa} + (f_{p1} + f_{p2})\ \tau_{ns}^{(\alpha)} \\
\kappa_{o,\mathrm{cub}}^{(\alpha)} &= \left[\left(\tau_{o,\mathrm{cub}}^{(\alpha)}\right)^{n_\kappa} + \Psi_{\mathrm{cub}}\left(f_{p1}, d_2, f_{p2}, d_3, f_{p3}\right)^{n_\kappa}\right]^{1/n_\kappa}
\end{aligned} \tag{3.4}$$

where

$$\begin{aligned}
\Psi_{oct} &= \Psi_{cub} \\
&= \left[c_{p1}\sqrt{\zeta \frac{f_{p1}^{'}}{d_1}} + c_{p2}\sqrt{\zeta \frac{f_{p2}^{'}}{d_2}} + c_{p3}\sqrt{\zeta\ f_{p3}^{'}\ d_3} + \frac{c_{gr}}{\sqrt{d_{gr}}}\right]
\end{aligned} \tag{3.5}$$

In this equation, $\zeta = \frac{\Gamma_{APB}}{\Gamma_{APB,ref}}$ where $\Gamma_{APB}$ is the anti-phase boundary energy. Also, $d_1$, $d_2$, and $d_3$, are the sizes of the primary, secondary, and tertiary $\gamma^{'}$ precipitates, respectively, while $d_{grn}$ is the grain size. The exponent $n_\kappa$ ranges from 1-1.2, and $c_{p1}$, $c_{p2}$, $c_{p3}$, and $c_{gr}$ are determined by fitting the initial yield strength to the experimental data. The non-Schmid stress dependence of the octahedral slip systems is given by $\tau_{ns}^{(\alpha)} = h_{pe}\tau_{pe}^{(\alpha)} + h_{cb}\left|\tau_{cb}^{(\alpha)}\right| + h_{se}\tau_{se}^{(\alpha)}$ [64–66], where $\tau_{pe}^{(\alpha)}$, $\tau_{cb}^{(\alpha)}$, and $\tau_{se}^{(\alpha)}$ are the resolved shear stresses on the primary, cube and secondary slip systems, respectively and $h_{pe}$,

$h_{cb}$, and $h_{se}$ are constants. The normalized precipitate volume fractions are defined by

$$f_{p1}^{'} = \frac{f_{p1}}{f_{p1} + f_m}, \qquad f_{p2}^{'} = \frac{f_{p2}}{f_{p2} + f_m}, \qquad f_{p3}^{'} = \frac{f_{p3}}{f_{p3} + f_m}. \tag{3.6}$$

During plastic deformation partial dislocations travel in pairs in order to retain order in the crystalline structure. When a pair of partial dislocations encounter a $\gamma^{'}$ precipitate obstacle, the dislocations can shear the obstacle, pile up at the obstacle, loop around the obstacle, or avoid the obstacle through cross slip. In Ni-base superalloys these precipitate dislocation interactions depend strongly on the precipitate size: (1) for underaged precipitates ($< 100\,\text{nm}$), shearing takes place by weakly coupled dislocation pairs and the CRSS increases with precipitate size, (2) for slightly larger particles ($100\,\text{nm} < d_p < 400\,\text{nm}$), shearing occurs by strongly coupled dislocation pairs and the CRSS decreases as a function of the precipitate size, and (3) for overaged particles ($> 400\,\text{nm}$), dislocation looping can occur depending on precipitate distribution, and is promoted by increasing temperature. The relationship between weak and strong dislocation pairs as a function of precipitate size is schematically shown in Figure 3.6.

The first two terms in Equation 3.5 account for increase of the CRSS by the shearing of the (small) primary and secondary precipitates by strongly coupled dislocation pairs and the third term represents shearing of tertiary precipitates by weakly coupled dislocation pairs as evidenced by TEM observations of deformation of KM4, a similar Ni-base superalloy, at a temperature of 650°C [68]. The last term in Equation 3.5 is based on the Hall-Petch relationship in which the CRSS increases with decreasing grain size.

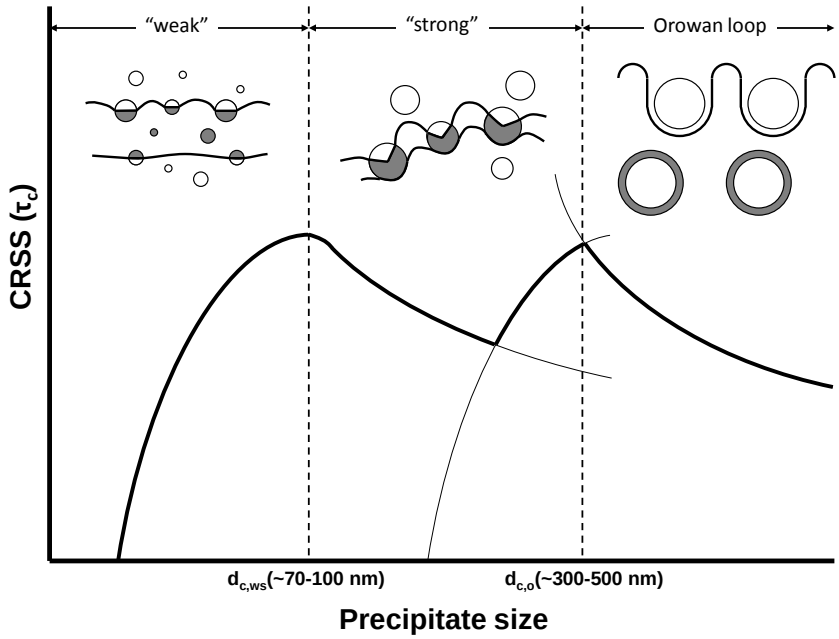


**Figure 3.6:** Schematic of theoretically expected CRSS as a function of particle size. After ref. [67].

In this model, hardening is assumed to be a function of dislocation storage, dynamic recovery, and the size and spacing of $\gamma^{'}$ precipitates. Dislocation storage includes statistically stored dislocations (SSDs) and geometrically necessary dislocations (GNDs) [69]. Dynamic recovery is due to dislocation annihilation and rearrangement. The rate of dislocation recovery is assumed to be directly proportional to the dislocation density [70]. Thus, the evolution of dislocation density is given by

$$\dot{\rho}_{\lambda}^{(\alpha)} = h_o \left\{ Z_o + k_1 \sqrt{\rho_{\lambda}^{(\alpha)}} - k_2 \ \rho_{\lambda}^{(\alpha)} \right\} \left| \dot{\gamma}^{(\alpha)} \right| \tag{3.7}$$

and

$$Z_o = \frac{k_\delta}{\tilde{b} \ d_{\delta \text{eff}}}, \quad d_{\delta \text{eff}} \approx \left( \frac{2}{d_{2\delta}} \right)^{-1} \tag{3.8}$$

where the $k_1 \sqrt{\rho_{\lambda}^{\alpha}}$ represents dislocation storage and $k_2 \rho_{\lambda}^{\alpha}$ represents dynamic recovery. Also, $k_1$, $k_2$, and $k_\delta$ are constants and $d_{2\delta}$ and $d_{\delta \text{eff}}$ represent secondary and equivalent precipitate spacing, respectively. In Equation 3.7, the hardening coefficients for the octahedral and cube slip systems are $h_o = 4.8$ and $h_o = 2.4$, respectively.

To capture the Bauschinger effect, a back stress term, $\chi^{(\alpha)}$, is used. The evolution of back stress follows the form

$$\dot{\chi}_{\lambda}^{(\alpha)} = C_{\chi} \left\{ \eta \ \tilde{\mu} \ \tilde{b} \ \sqrt{\rho_{\lambda}^{(\alpha)}} \ \mathrm{sgn}\left(\tau^{(\alpha)} - \chi_{\lambda}^{(\alpha)}\right) - \chi_{\lambda}^{(\alpha)} \right\} \left| \dot{\gamma^{(\alpha)}} \right| \tag{3.9}$$

and

$$\eta = \frac{\eta_o \ Z_o}{Z_o + k_1 \sqrt{\rho_{\lambda}^{(\alpha)}}} \tag{3.10}$$

where $C_{\chi}$ is a fitting parameter, and $\eta$ reflects the relative proportion of GNDs to total dislocation density.

A summary of the constitutive equations are shown in Table 3.3. The above constitutive model is implemented as a user defined material (UMAT) subroutine in ABAQUS [71].

### 3.3.1 Model Calibration

Using the above framework, Shenoy et al. [1] used fully 3D finite element analysis to fit the above constitutive responses to very complex cyclic stress-strain behavior. Strain histories with and without hold periods at maximum strain were used to estimate the time-dependent behavior of the stress strain curve at a temperature of 650°C, the intended gas turbine disk operating temperature. See Figures 12-15 in ref. [1] for stress-strain response calibration of the coarse grain (super weak) and fine grain (sister disk) IN100 microstructures used in the current study. The microstructure-sensitive crystal plasticity constants fitted through experiments are listed in Table 3.4.

**Table 3.3:** Microstructure-sensitive crystal plasticity constitutive equations

Flow rule with back stress, threshold stress and drag stress

$$\dot{\gamma}^{(\alpha)} = \left[\dot{\gamma}_1 \left\langle \frac{\left|\tau^{(\alpha)} - \chi^{(\alpha)}\right| - \kappa_\lambda^{(\alpha)}}{D^{(\alpha)}} \right\rangle^{n_1} + \dot{\gamma}_2 \left\langle \frac{\left|\tau^{(\alpha)} - \chi^{(\alpha)}\right|}{D^{(\alpha)}} \right\rangle^{n_2}\right] \operatorname{sgn}\left(\tau^{(\alpha)} - \chi^{(\alpha)}\right)$$

Threshold Stress

$$\kappa_\lambda^{(\alpha)} = \kappa_{o,\lambda}^{(\alpha)} + \alpha_t\ \tilde{\mu}\ \tilde{b}\ \sqrt{\rho_\lambda^{(\alpha)}} \quad \text{for} \quad \lambda = \text{oct, cub,}$$

where $\quad \tilde{\mu} = (f_{p1} + f_{p2} + f_{p3})\ \mu_{\gamma'} + f_m\ \mu_m, \qquad \tilde{b} = (f_{p1} + f_{p2} + f_{p3})\ b_{\gamma'} + f_m\ b_m$

Initial Thresholds

$$\kappa_{o,\text{oct}}^{(\alpha)} = \left[\left(\tau_{o,\text{oct}}^{(\alpha)}\right)^{n_\kappa} + \Psi_{\text{oct}}\left(f_{p1}, d_2, f_{p2}, d_3, f_{p3}\right)^{n_\kappa}\right]^{1/n_\kappa} + (f_{p1} + f_{p2})\ \tau_{ns}^{(\alpha)}$$

$$\kappa_{o,\text{cub}}^{(\alpha)} = \left[\left(\tau_{o,\text{cub}}^{(\alpha)}\right)^{n_\kappa} + \Psi_{\text{cub}}\left(f_{p1}, d_2, f_{p2}, d_3, f_{p3}\right)^{n_\kappa}\right]^{1/n_\kappa}$$

where

$$\tau_{ns}^{(\alpha)} = h_{pe}\tau_{pe}^{(\alpha)} + h_{cb}\left|\tau_{cb}^{(\alpha)}\right| + h_{se}\tau_{se}^{(\alpha)} \quad \text{(non-schmid term)}$$

$$\Psi_{oct} = \Psi_{cub} = \left[c_{p1}\sqrt{\zeta\frac{f_{p1}^{'}}{d_1}} + c_{p2}\sqrt{\zeta\frac{f_{p2}^{'}}{d_2}} + c_{p3}\sqrt{\zeta\ f_{p3}^{'}\ d_3} + \frac{c_{gr}}{\sqrt{d_{gr}}}\right],$$

$$\zeta = \frac{\Gamma_{APB}}{\Gamma_{APB,ref}}, \quad f_{p1}^{'} = \frac{f_{p1}}{f_{p1} + f_m}, \quad f_{p2}^{'} = \frac{f_{p2}}{f_{p2} + f_m}, \quad f_{p3}^{'} = \frac{f_{p3}}{f_{p3} + f_m},$$

Internal State Variables

(a) Dislocation Density:

$$\dot{\rho}_\lambda^{(\alpha)} = h_o\left\{Z_o + k_1\sqrt{\rho_\lambda^{(\alpha)}} - k_2\ \rho_\lambda^{(\alpha)}\right\}\left|\dot{\gamma}^{(\alpha)}\right| \quad \text{(self-hardening)}$$

$$Z_o = \frac{k_\delta}{\tilde{b}\ d_{\delta\text{eff}}}, \qquad d_{\delta\text{eff}} \approx \left(\frac{2}{d_{2\delta}}\right)^{-1}$$

(b) Back Stress:

$$\dot{\chi}_\lambda^{(\alpha)} = C_\chi\left\{\eta\ \tilde{\mu}\ \tilde{b}\ \sqrt{\rho_\lambda^{(\alpha)}}\ \operatorname{sgn}\left(\tau^{(\alpha)} - \chi_\lambda^{(\alpha)}\right) - \chi_\lambda^{(\alpha)}\right\}\left|\dot{\gamma^{(\alpha)}}\right| \quad \text{(self-hardening)}$$

$$\eta = \frac{\eta_o\ Z_o}{Z_o + k_1\sqrt{\rho_\lambda^{(\alpha)}}}$$

**Table 3.4:** Parameters of the microstructure-sensitive crystal plasticity model at 650°C [59].

| Material | $\alpha_t$ | $C_\chi$ | $d_{1\delta}$( nm) | $d_{2\delta}$( nm) | $\dot{\gamma}_1(x10^{-10}s^{-1})$ |
|---|---|---|---|---|---|
| Coarse Grain IN100 | 0.1 | 2 | - | 15 | 0.417 |
| Fine Grain IN100 | 0.0 | 8 | 358 | 19.4 | 0.157 |

Common parameters for all microstructures

| $\tau^{(\alpha)}_{o,\mathrm{oct}}$( MPa) | $\tau^{(\alpha)}_{o,\mathrm{cub}}$( MPa) | $c_{p1}$ | $c_{p2}$ | $c_{p3}$ | $c_{gr}$( MPa$\sqrt{\mathrm{mm}}$) | $n_\kappa$ |
|---|---|---|---|---|---|---|
| 85.1 | 170.2 | 1.351 | 1.351 | 1.22 x $10^5$ | 9.432 | 1 |

| $b_{\gamma'}$( nm) | $b_\gamma$( nm) | $\mu_{\gamma'}$( MPa) | $\mu_\gamma$( MPa) | $k_1$( mm$^{-1}$) | $k_2$ | $\rho^{(\alpha)}_{\lambda,o}$( mm$^{-2}$) | $h_o$ |
|---|---|---|---|---|---|---|---|
| 0.25 | 0.41 | 81,515 | 130,150 | 2.6 x $10^5$ | 8.2 | 1.0 x $10^5$ | 4.8(oct), 2.4(cub) |

| $h_{pe}$ | $h_{cb}$ | $h_{se}$ | $\Gamma_{\mathrm{APB}}(=\Gamma_{\mathrm{APB,ref}})$ ( J/m$^2$) | $\eta_o$ | $k_\delta$ |
|---|---|---|---|---|---|
| 0.8 | 0.0 | -0.4 | 164 x $10^{-3}$ | 2.82 | 2.5 x $10^{-3}$ |

| $C_{11},\gamma'$( MPa) | $C_{12},\gamma'$( MPa) | $C_{44},\gamma'$( MPa) | $C_{11},\gamma$( MPa) | $C_{12},\gamma$( MPa) | $C_{44},\gamma$( MPa) |
|---|---|---|---|---|---|
| 135,000 | 59,210 | 81,515 | 158,860 | 73,910 | 130,150 |

| $n_1$ | $n_2$ | $\dot{\gamma}_1$( s$^{-1}$) | $\dot{\gamma}_1$( s$^{-1}$) | $D^{(\alpha)}$( MPa) |
|---|---|---|---|---|
| 15 | 9 | 8.7 | 3.9 x $10^{-11}$ | 150(oct), 180(cub) |

## 3.4 Modeling Stages of Fatigue Crack Formation and Growth

Three stages of fatigue crack formation and growth are modeled in the present investigation, including fatigue crack incubation, microstructurally small crack growth and linear elastic fracture mechanics (LEFM) crack growth. In this study, deterministic approaches based on the physical mechanisms of fatigue crack formation and growth are used to compare multiple instantiations for specimens with different notch root sizes. The concept of a fatigue indicator parameter (FIP) is introduced in this section. These FIPs are computable response parameters that are used here to characterize the multiaxial micromechanics of damage accumulation within a microstructure.

### 3.4.1 Fatigue Indicator Parameters

There have been many multiaxial parameters that have been introduced to correlate fatigue damage and cyclic stress-strain state [72]. The multiaxial fatigue indicator parameters (FIPs) that are relevant to fatigue crack formation and small crack growth consider the combined effects of resolved shear stresses/strains and normal stresses/strains on a given plane. The normal stresses provide crack opening, reducing friction between crack surfaces, and resolved shear stresses support dislocation motion on the slip plane. In this study we characterize the Stage I, shear-dominated formation and growth of cracks through the use of the Fatemi-Socie (FS) parameter [72,73]. The FS parameter has demonstrated robust correlation of crack initiation in polycrystals under various multiaxial loading conditions [74,75]. Using the crystal plasticity constitutive equations described above the plastic strain tensor is computed based on the multiplicative decomposition of the deformation gradient into plastic (dislocation slip) and elastic parts (lattice rotation and distortion), i.e., $\boldsymbol{F} = \boldsymbol{F}^e \cdot \boldsymbol{F}^p$. The plastic strain tensor is then used to calculate the FS Parameter. This FIP takes into account the plane of maximum plastic shear and the stress normal to this plane,

i.e.,

$$P_{FS} = \frac{\Delta\gamma_{max}^{p*}}{2}\left(1 + K^{'}\frac{\sigma_n^{max*}}{\sigma_y}\right) = \Delta\Gamma \tag{3.11}$$

where $\Delta\gamma_{max}^{p*}$ is the maximum range of plastic shear strain over a fatigue cycle, $K^{'}$ is a constant that controls the effect of normal stress in fatigue crack formation and early growth, and $\frac{\sigma_n^{max*}}{\sigma_y}$ is the ratio between the maximum tensile stress normal to this plane and the cyclic yield strength. For consistency, the FIPs are averaged over the fine grain scale (4 µm) for both IN100 microstructures and are calculated over the third fatigue cycle in each simulation. In the present work, $K^{'} = 1.0$, which has been correlated to a wide variety of multiaxial loading histories for the fatigue life of IN718, a similar nickel-base superalloy [73].

### 3.4.2 Crack Incubation

In the present study, we consider crack incubation as the formation of a crack on the order of grain size. Many models involving the formation of cracks within a grain are based on the Tanaka and Mura model proposed for Stage I crack incubation [76]. The range of cyclic shear stress on the shear plane is assumed to drive the fatigue damage accumulation. This model assumes that two parallel, closely-spaced slip planes partake in dislocation dipole accumulation via a ratcheting mechanism (ex: layer I and layer II). Upon loading, dislocations on layer I move until they encounter an obstacle and pile up to form a back stress. This back stress equilibrates the applied shear stress on that plane. During load reversal, the back stress on layer I assists the applied shear stress on layer II and is balanced by the back stress on layer II (in the positive layer I direction). Next, this back stress on layer II becomes a forward stress on layer I. This cyclic ratcheting model and associated increase in dislocation density per fatigue cycle increases the potential energy of the layer I and layer II dislocation dipole. The energy balance between this dislocation dipole energy and the surface

energy to form a crack are related by [76]

$$2N_i\Delta U = 4aW_s \tag{3.12}$$

where $N_i$ is the number of cycles to form the crack, $2\Delta U$ is the potential energy of the dislocation dipole, $2a$ is the size of the grain, and $2W_s$ is the energy to form the crack surface. This equivalence was expanded to arrive at the following

$$(\Delta\tau - 2k)^2 N_i = \frac{4\mu W_s}{\pi(1-\nu)a} \tag{3.13}$$

Here, $\Delta\tau$ is the applied shear stress range, $k$ is the lattice friction stress, $\mu$ is the shear modulus, and $\nu$ is the Poisson ratio. A simplified form of this model has been extended to microplasticity by Shenoy et al. [2] to estimate the incubation life for IN100 for a crack on the order of a grain size

$$N_{inc}\left(\frac{avg\left(\Delta\gamma^p_{max}\right)}{2}\right)^2 = \frac{\alpha_g}{d_{gr}}\ , \tag{3.14}$$

where $\alpha_g$ is a parameter fit to experiments.

### 3.4.3 Microstructurally Small Crack Growth

The growth of microstructurally small cracks depends strongly on the local microstructure. In the HCF regime, a large portion of fatigue life is spent forming and propagating a small crack. Therefore, accurate modeling of small crack growth is very important in HCF fatigue life estimation. The most important condition for analysis is whether a crack, regardless of its size, will or will not propagate. Therefore, in this context, the fatigue limit is not related to the incubation of a crack, but to the threshold condition which determines whether the crack will continue to grow to failure.

The fluctuation of the crack growth resistance for the microstructurally small crack is often attributed to the retardation of crack growth by grain boundaries [16]. As seen in previous sections (ref. Figure 2.4), a decrease in growth rate can be observed when a crack-tip approaches a grain boundary and can even be arrested at

the boundary. This small crack growth threshold depends on microstructure features (such as mean distance between particles and grain size) and loading condition. Once the crack crosses the grain boundary, growth accelerates, and this oscillatory behavior may be repeated until microstructure effects are negligible and a condition of similitude is reached. Consequently, the growth of small cracks varies from microstructure to microstructure. There is no unique relationship between the range of stress intensity factor, $\Delta K$, and the crack growth rate da/dN of small cracks. Frequently, a phenomenological mean value of the fluctuating small crack growth rate is used in small crack growth models.

For the growth of small fatigue cracks other fracture mechanics techniques have been used, namely microstructural fracture mechanics (MFM) and elastic-plastic fracture mechanics (EPFM). In the MFM regime, microstructure effects dominate small crack growth. As the cracks grow, the effects of microstructure on growth decrease and the regimes of MFM, EPFM and LEFM merge into one crack growth curve. One relationship for MFM takes the form [77]

$$\frac{da}{dN} = A\Delta\gamma^{\alpha}\,(d-a) \tag{3.15}$$

where $A$ and $\alpha$ are material constants and $\Delta\gamma$ is the cyclic shear strain range. The value of $d$ depends on material length scales and the dominating microstructure barrier. This parameter is dependent on stress state, stress level and material microstructure. The growth of a crack under elastic-plastic fracture mechanics can be described by [77]

$$\frac{da}{dN} = B\Delta\gamma^{\beta}a - D \tag{3.16}$$

where $B$ and $\beta$ are material constants and $D$ is an EPFM threshold value. Using Equations 3.15 and 3.16, Miller et al. [78] compared experimental data of a 0.4% carbon steel and the results are shown in Figure 3.7. This figure shows the non-uniqueness of the small crack growth rate and the model that is used to estimate the

mean small crack growth rate.

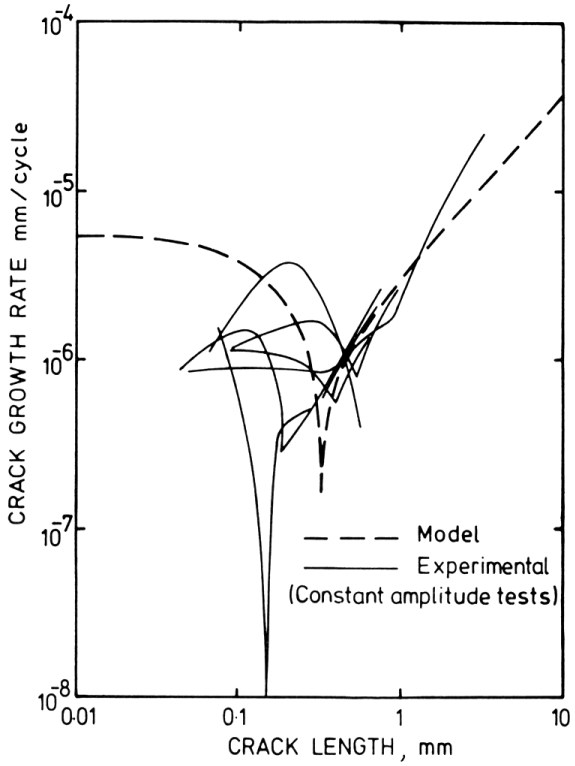


**Figure 3.7:** Comparison of experimental crack growth of a steel and predicted crack growth rates [78].

Previous work on fatigue crack propagation (FCP) life under multiaxial stress states have been done by many researchers. Fatemi and Kurath [72] and Fatemi and Socie [73] have demonstrated robust correlation of FCP life in a Ni-base superalloy IN718 using a shear-based multiaxial parameter, the Fatemi-Socie parameter, as an indication of microstructurally small crack (MSC) growth rate. A modified form of the MSC growth law with the Fatemi-Socie parameter, $\Delta\Gamma$, used as the driving force was proposed by Shenoy et al. [2], i.e.,

$$\frac{da}{dN} = A_{FS}\ \tau_y\ \Delta\Gamma\ a - \eta b \approx \Delta CTD - \Delta CTD_{th} \tag{3.17}$$

Here, $A_{FS}$ is a parameter fitted through experiments, $\tau_y$ is the critical resolved resolved shear stress given by $\tau_y = \sigma_y/M$, where $M = 3.06$ is the Taylor factor for a randomly textured FCC polycrystalline aggregate [79], $a$ is the crack length, $\Delta\Gamma$ is

the Fatemi-Socie FIP found through simulations, $\eta$ is a constant ($\approx 1$), and $b$ is the magnitude of the burgers vector. In the current study, the FS parameter is averaged over the fine-grain IN100 scale. The form of Equation 3.17 is consistent with the $\Delta J$ based approach to address the growth of small cracks along critical planes [80]. The value of $A_{FS}$ is calibrated through experiments and is determined to be 8.1 x $10^{-4}$ $(\text{MPa} - \text{cycle})^{-1}$ [2]. A modified form of Equation 3.17 is used in the present study to estimate the propagation life due to MSC growth, i.e.,

$$\frac{da}{dN} = A_{FS}\ \tau_y\ \Delta\Gamma\ a \tag{3.18}$$

For incremental crack extension, the modified MSC growth law in Equation 3.18 can be integrated and rearranged to determine the number of cycles to propagate a crack from $a_{j-1}$ to $a_j$

$$N_{prop,MSC}(a_{j-1} \rightarrow a_j) = \frac{\ln\left(\frac{a_j}{a_{j-1}}\right)}{A_{FS}\ \tau_y\ \Delta\Gamma_{ave}(a_{j-1}, a_j)}\ , \tag{3.19}$$

where $a_{j-1}$ and $a_j$ is the crack length at increment $j-1$ and $j$, respectively.

### 3.4.4 Linear Elastic Fracture Mechanics Crack Growth

Linear elastic fracture mechanics (LEFM) is used to model the growth of a crack from an initial size ($a_i \approx 1\,\text{mm}$) to a final crack size at failure ($a_f$). For LEFM to be applicable, the conditions for similitude and small scale yielding must be met. Similitude is the concept in which crack tip conditions are similar as long as the magnitudes of the characterizing parameter (in this case the stress intensity factor $\Delta K$) are identical [15]. The growth of a crack in LEFM is typically modeled through the use of the Paris-Erdogan law [48], a power law relationship between crack growth of "long" cracks (where LEFM is applicable) and the range of mode I stress intensity factor over one cycle ($\Delta K$), i.e.,

$$\frac{da}{dN} = C\,(\Delta K)^m \tag{3.20}$$

where $C$ and $m$ are material constants and $\Delta K = K_{max} - K_{min}$ is the stress intensity range. The stress intensity range depends on crack geometry, crack length, crack location in the specimen, and loading condition. The general form for the stress intensity factor range is

$$\Delta K = Y \Delta\sigma \sqrt{\pi a} \tag{3.21}$$

Here, $Y$ is a function of crack geometry and loading condition, $\Delta\sigma$ is the remote applied stress range, and $a$ is the crack length.

The growth rate of cracks also depends greatly on the load ratio (R-ratio) or the ratio of minimum to maximum applied stress. Generally, for the same stress intensity range, the crack growth rate is higher for a higher R-ratio. To account for load ratio dependence of the da/dN versus $\Delta K$, several empirical models have been proposed. The most widely used are approaches of Forman, Kearney, and Engle [81] defined by

$$\frac{da}{dN} = \frac{C_a \Delta K^{m_a}}{(1-R)K_c - \Delta K} \ , \tag{3.22}$$

and Walker [82]

$$\frac{da}{dN} = C_b[(1-R)^{n_b} K_{max}]^{m_b} \tag{3.23}$$

In the above equations, $K_c$ is the stress intensity factor at failure and $C_a$, $C_b$, $m_a$, $m_b$, and $n_b$ are Paris-type material constants.

The number of cycles to failure of the specimen can be estimated through rearrangement and integration (often numerically) of the Paris-Erdogan law, e.g.,

$$N_{prop,LEFM} = \int_{a_i}^{a_f} \frac{da}{C\,(\Delta K)^m} \tag{3.24}$$

Therefore, the total life of a component can now be estimated using the crack growth equations described for crack incubation (ref. Equation 3.14), microstructurally small crack growth (Equation 3.19), and long crack growth lives (Equation 3.24), i.e., $N_{total} = N_{inc} + N_{prop,MSC} + N_{prop,LEFM}$. Each of these regimes has different crack growth characteristics based on the distinctive deformation mechanisms observed in

each regime. These deterministic methods will be used to model crack formation and propagation on a notched specimen loaded under cyclic tension/compression loading.

### 3.4.5 Fatigue Crack Formation and Growth Calibration to Experiments

#### *3.4.5.1 Experimental Data and Trends*

To calibrate the above crack incubation and MSC growth models, a simple computational model was used and compared to experimental "initiation" lives. For the LCF regime, the experimental data used for comparison are from the work by Cowles et al. [83, 84]. They performed an extensive study to determine the high-temperature cyclic behavior of several Ni-base superalloys used for gas turbine engine disks. Several cyclic and cyclic/dwell tests were conducted on cylindrical "dog bone" specimens and compact tension specimens to determine crack initiation and propagation lives at 650°C in air. Of particular interest here are the fully reversed, strain-controlled fatigue tests conducted on the cylindrical specimens to determine fatigue crack "initiation" life. The fatigue crack initiation life in these experiments was defined as the number of cycles to produce a 5% drop in the cyclic load range. The specimens had a minimum gage section diameter of 5.36 mm. For further details on the specimen dimensions or test results refer to ref. [84]. The cyclic tests used a triangular strain-time waveform at a frequency of 0.33 Hz ($\dot{\epsilon} \approx 0.004$-$0.013\ s^{-1}$ depending on applied strain range). For this study, the fine grain IN100 microstructure is compared to the experiments performed on "Gatorized IN100" and the coarse grain IN100 microstructure is compared to the experiments performed on a hot isostatic pressed (HIP) Astroloy, which has a similar grain size (30-70 μm [85]) as that of coarse grain IN100 (34 μm).

Another experimental study was used to compare fatigue lives in the HCF ($\sim 10^6$) to VHCF ($\sim 10^9$) regimes. Bathias and Paris [86, 87] reported stress-life data in the HCF/VHCF range for a PM Ni-base superalloy N18 at 450°C for different R ratios (ref. Figure 3.8). In order to obtain S-N data within the $10^6 - 10^9$ fatigue life range in a reasonable amount of time, ultrasonic fatigue testing at 20 kHz is necessary. The

N18 alloy has a grain size of $\sim 7 - 15\,\mu m$. Figure 3.8 shows stress-life data for both a standard N18 alloy, which contains fewer than 20 inclusions per kilogram, and a seeded N18 alloy, which has 30,000 ceramic inclusions of $Al_2$ and MgO of size $\sim 80\,\mu m$ in one kilogram of the alloy. As seen from Figure 3.8, the R ratio has a significant effect on the fatigue life of this alloy. For comparison purposes, the applied strain amplitude was surmised by dividing the stress amplitude by the elastic modulus of $E = 170\,GPa$. The standard N18 fatigue data at $R = -1$ is contrasted with the computational model described in the next section.

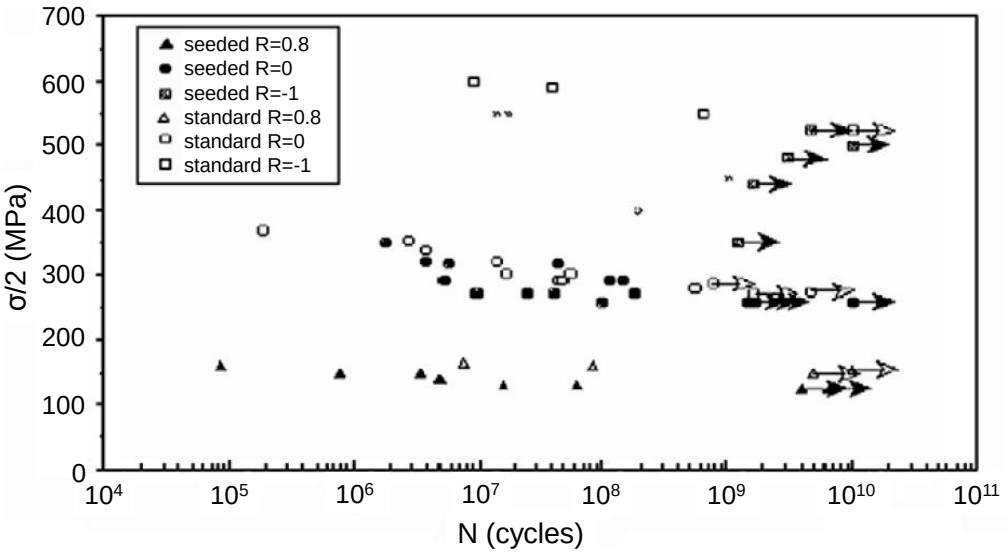


**Figure 3.8:** S-N curves for N18 at 450°C in HCF/VHCF regime [86].

One concern with running experiments at such a high frequency is the strain rate effects on the fatigue of a component. For example, experimental work on BCC low carbon steel shows that the crack growth rate under ultrasonic fatigue tests (f=20 kHz) is slower than that of conventional tension-compression fatigue tests (f=10 Hz) [88]. This can be attributed to the limited ability of slip bands to form at such a high strain rate, causing the plastic zone at the crack tip to be smaller than that of a fatigue test at a slower rate. Also, the fatigue strength for components subjected to ultrasonic fatigue tests were higher than those under conventional fatigue tests for the

same number of cycles to failure [88]. In contrast, room temperature fatigue testing of a Ni-base superalloy Udimet 500 show little effect of frequency on the fatigue life in the $10^6 - 10^9$ fatigue life regime (ref. Figure 3.9). However, based on the limited number of data points in the HCF/VHCF regime, the slope of the S-N curve for ultrasonic fatigue testing (f=20 kHz) is larger than the that of a more conventional fatigue testing loading rate (f=10 Hz) for the same Ni-base superalloy.

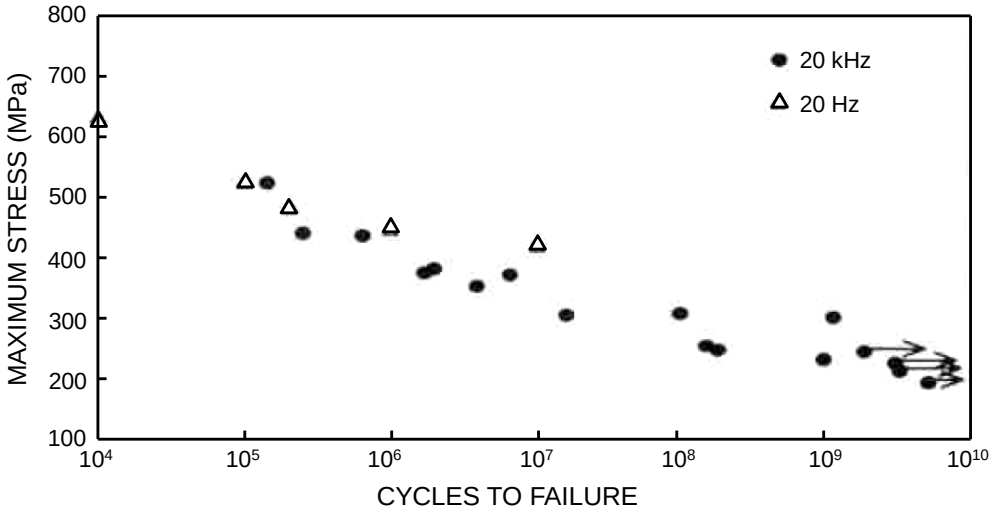


**Figure 3.9:** S-N curves for Udimet 500 at room temperature in HCF/VHCF regime, $R = -1$ [89].

#### *3.4.5.2 Computational Calibration to Experiments*

Two different blocks of material that contain 64 cuboidal grains (4 grains x 4 grains x 4 grains) and 1000 cuboidal grains (10 grains x 10 grains x 10 grains) with random orientation distribution were used to simulate the smooth fatigue specimens used in experiments. Each grain is composed of 8 C3D8 elements (2 elements x 2 elements x 2 elements) in both models. The two models used are shown in Figure 3.10. These idealized microstructures are loaded in uniaxial tension/compression fully reversed loading ($R_\epsilon = -1$) for three cycles at a strain rate of ($\dot{\epsilon} = 10^{-3}\,\mathrm{s}^{-1}$) and at various strain amplitudes. Periodic boundary conditions are imposed on each block so that opposite faces of the block have the same deformation. Periodic boundary conditions

tessellates the volume of the block to simulate overall bulk response of a given material. This model is used to simulate the response of a smooth test specimen. The maximum cyclic plastic shear strain is calculated over the third loading cycle. A value of $\alpha_g = 0.056\,\mu$m-cycle is used in Equation 3.14 to find the number of cycles to crack initiation to the grain size and Equation 3.19 is used for MSC growth to a desired length. In this study, MSC growth was considered through 3 grains from the initial cracked grain. This value provided good correspondence between computational and experimental strain-life data.

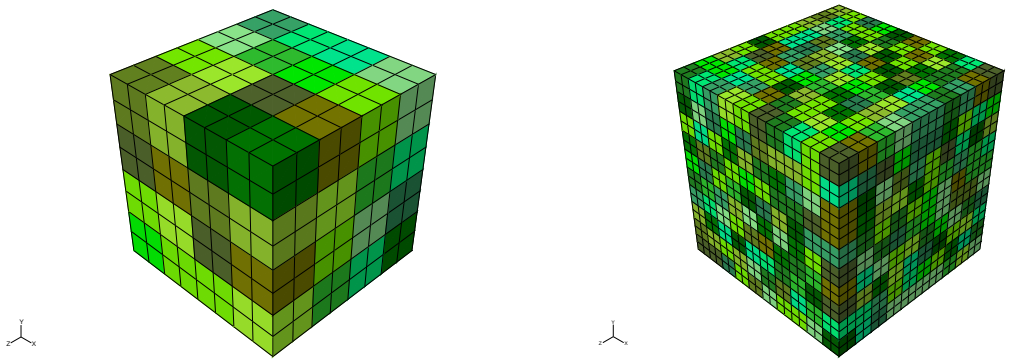

(a) 64 grain block model

(b) 1000 grain block model

**Figure 3.10:** Finite element meshes used to simulate a "smooth" specimen (figures not to scale).

Comparison of smooth specimen experimental and computational data is shown in Figure 3.11 for the fine grain IN100 microstructure and Figure 3.12 for the coarse grain IN100 microstructure. Note that the experimental data is only plotted for the regime in which experimental tests were conducted. There are several interesting conclusions that arise from this computational study:

- Considering the MSC growth of a crack through 3 neighboring grains from an initial crack on the order of a grain, the computational strain-life curves depict the experimental data well in the LCF to HCF regime.

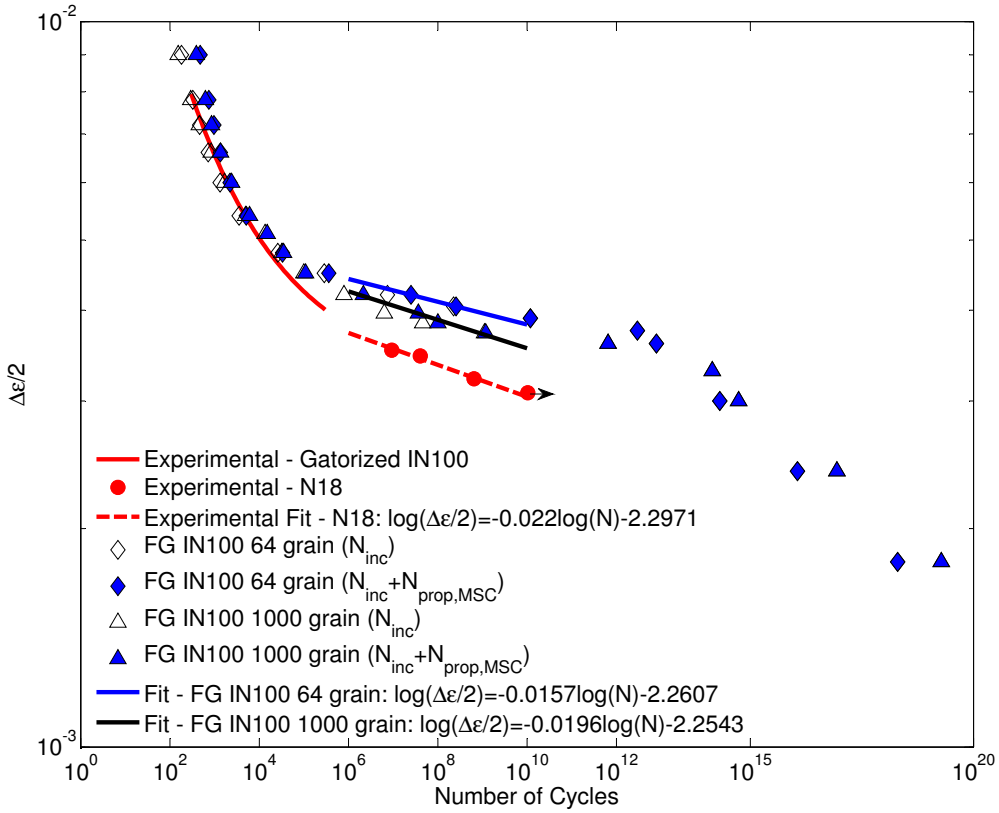


**Figure 3.11:** Comparison of experimental and computational fatigue crack "initiation" for $R_\epsilon = -1$ loading of a fine grain (FG) IN100. Experimental data for Gatorized IN100 are from [83] and N18 data are from [86].

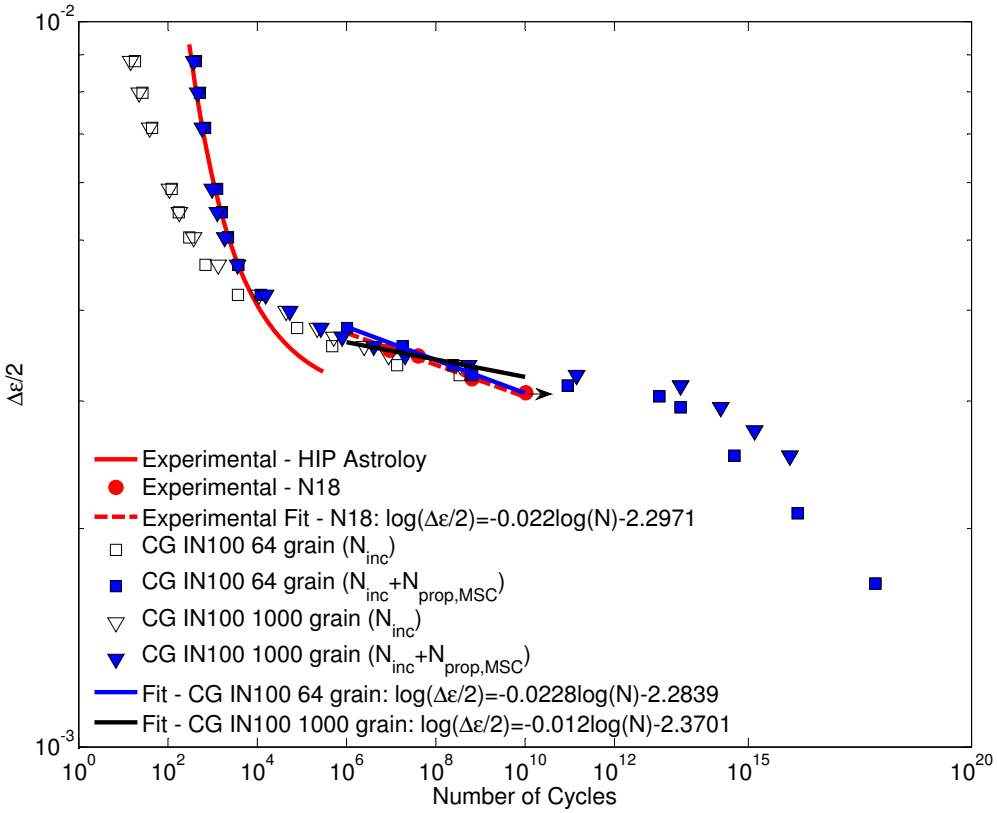


**Figure 3.12:** Comparison of experimental and computational fatigue crack "initiation" for $R_\epsilon = -1$ loading of a coarse grain (CG) IN100. Experimental data are for HIP Astroloy are from [83] and N18 data are from [86].

- The slope of the strain-life curve in the HCF/VHCF regime ($10^6 - 10^{10}$ cycles) found through the computational study is very close to that seen in experimental ultrasonic fatigue testing. As indicated in Figure 3.9, the slope of the strain-life in the "elastic" region for a Ni-base superalloy varied little for cyclic loading frequencies of 20 Hz and 20 kHz.

- The computational model predicts that there is another transition in the strain-life curve in the regime of $\sim 10^{12}$ cycles and beyond. This can indicate that there is an absence of plasticity within the grain level response. Further investigation of the grain level FIP shows an interesting characteristic. In Figure 3.13, the maximum, minimum, and average FIP values as a function of the applied strain amplitude are shown for 1-10 cycles. As indicated from the diagram, at low strain amplitudes, the FIP distribution is relatively stationary as indicated from the relative distance between the maximum, minimum and average lines. The change in FIP response as a function of strain amplitude at lower applied strains is relatively linear on the semi-log plot, reflecting the overall nominal elastic response. In addition, at lower applied strain amplitudes there is no difference in the computed FIP values among 1-10 cycles, which indicates that there is no cyclic ratcheting within the microstructure. This further displays that the grain level response is elastic. As the strain amplitude is increased, the FIP versus strain amplitude reaches an inflection point and a subsequent separation of the maximum, minimum, and average FIP curves occurs. This inflection point occurs at $\epsilon_a \approx 0.75\epsilon_y = 0.32\%$ ($\sigma_a = 560$ MPa) for coarse grain IN100, where $\epsilon_y$ is the macroscopic proportional limit for each material. This separation indicates that at this inflection point, localized slip can occur which signifies a threshold strain amplitude value in which the grain level response transforms from fully elastic to a mostly elastic/slightly plastic. This threshold strain amplitude is below the macroscopic proportional limit. Thus, a plot of

the macroscopic cyclic stress-strain data may not be sufficient to indicate microplasticity and microcrack formation at the grain level (ref. Figure 3.14). For a strain amplitude of $\epsilon_a = \epsilon_y$, the macroscopic stress-strain response is elastic as shown in Figure 3.14, but the grain level FIP values indicate localized plasticity (ref. Figure 3.13). It is also interesting to note that the inflection point at a strain amplitude of $\epsilon_a \approx 0.75\epsilon_y = 0.32\%$ in Figure 3.13 corresponds to the downturn in the strain-life plot at $\sim 10^{12}$ cycles in Figure 3.12. Since experiments are not available at this point for regimes past $10^{10}$ cycles, we are unable to verify the slope of the strain life curve beyond $10^{10}$ cycles in Figures 3.11 and 3.12. In addition, the number of cycles to fatigue crack initiation is found through Equation 3.14. This equation uses the plastic shear strain tensor, which is not relevant in this regime based on the above FIP argument, to calculate the cycles to crack initiation. Further investigation is required to determine the dominant fatigue mechanisms (if any) that are active in this ultra high cycle fatigue regime. However, we can conclude that the grain level response of a perfect material (without inclusions or other microdefects) is elastic for a smooth specimen loaded below the threshold strain amplitude of $\epsilon_a \approx 0.75\epsilon_y = 0.32\%$ ($\sigma_a = 560\,\text{MPa}$) for coarse grain IN100.

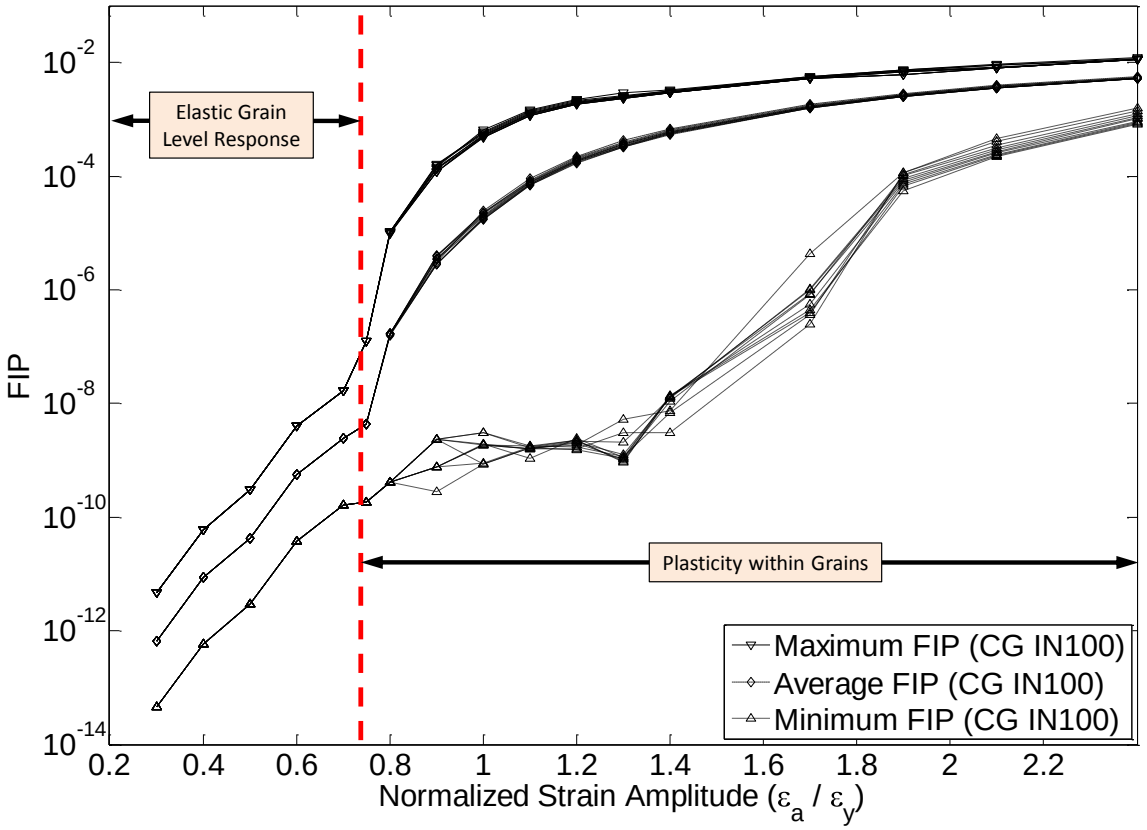


**Figure 3.13:** "Smooth specimen" computed FIP vs. normalized strain amplitude coarse grain IN100 64 grain model. Each black line represents the FIP value for a given number of cycles (1 through 10).

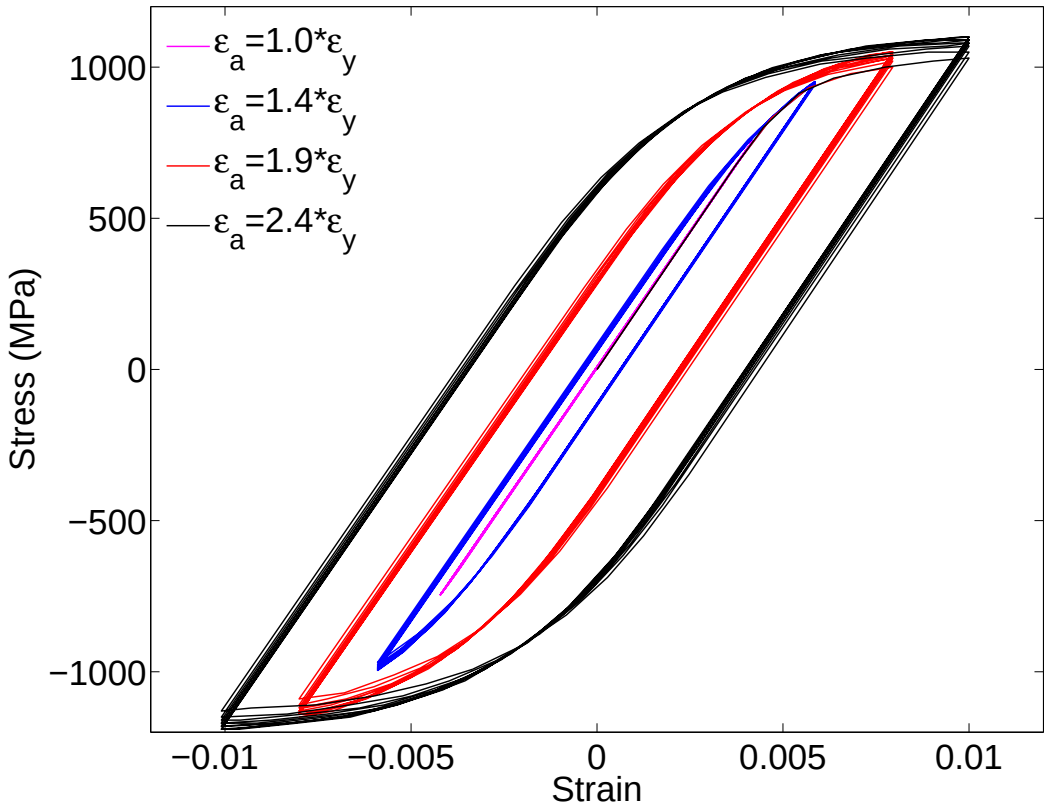


**Figure 3.14:** Stress strain curve for coarse grain IN100 64 grain smooth specimen for different strain amplitudes.

- It is recognized that this model has several limitations. Instead of using similar Ni-base superalloys such as HIP Astroloy and N18, the computational model could be better calibrated by comparing to actual coarse grain and fine grain IN100 material fatigue data in all strain-life regimes. Another limitation is the limited number of data points for experimental S-N plots reported in literature. Experimentally and computationally, there is a significant amount of scatter in fatigue life data in the HCF/VHCF regimes. The current model could be more robust with additional data points for curve fitting. Another aspect that could be improved is to consider the grain size distribution and to increase the number of elements per grain. Larger grains in a microstructure are typically more favorable for fatigue crack formation as compared to smaller grains. The smooth specimen model used here is an idealized microstructure that has a uniform grain size distribution and contains only 2 elements through the thickness of the grain. Using only 2 elements though the thickness of the grain can limit the ability to detect gradients in plastic slip distribution within a given grain. These plastic slip gradients arise due to combined effects of the anisotropic behavior of the nearest neighbor grains and the requirements of strain compatibility. Other defects and microstructure characteristics not taken into account in this model are inclusions, pores, initial residual stress distributions, and triple point junctions, which all have an effect on strain localization and thus, fatigue crack formation.

Considering the above limitations, the computational "smooth specimen" model fitted to experiments in this section is sufficient for the purposes of this study. The smooth specimen is used to establish a baseline comparison to notched specimens. The notched specimen computational model is described in the following section.

## 3.5 Finite Element Implementation

The crystal plasticity response described above is used to model the cyclic deformation of a notched specimen. Due to the stress concentration effect, fatigue cracks within a notched component usually form at the notch root. Therefore, we are interested in both the microstructure-sensitive response within the notch root region and the stress gradient effect on formation and propagation of a crack to a characteristic length. These simulations capture both the essence of the notch root stress concentration and the complexity of realistic microstructures. Notch size effects will be explored by simulating different size notches subjected to fully reversed tension/compression loading at different strain amplitudes. Using the crystal plasticity formulations described previously in conjunction with the deterministic crack formation and propagation techniques described in the previous section, the distribution of slip within the notch region will be used to identify the probability of failure of the notched components. The notched components simulated in this study are double edge notched tension/compression specimens. The implementation strategy in ABAQUS [71] is described in the following section.

### 3.5.1 Geometric Model Details

Simulations were conducted in ABAQUS CAE [71] on various notched specimen geometries. To improve computational efficiency, the notched specimen is decomposed into three regions: (1) the outermost region, which is far from the notch root, imposes an isotropic linear elastic response using the elastic modulus found from macroscopic experimental stress strain curves; (2) an intermediate region employs both macroscopic J2 cyclic plasticity theory and isotropic linear elasticity in order to minimize effects of discontinuity between the fully elastic outer region and (3) the innermost 3D crystal plasticity region. Since symmetry conditions exist, only one half of the

double edge-notched specimen was modeled to render the simulations less computationally expensive. The dimensions of the crystal plasticity region are selected so that the distribution of microslip within the notch region is fully encapsulated for the applied loading conditions. For higher strain amplitude loading, the size of the crystal plasticity zone would have to be increased. For consistency in fatigue indicator parameter analysis, the fine grain IN100 mesh size was used near the notch root region. Thus, the fine grain microstructure crystal plasticity (CP) zone contains 1 element per grain (see Figure 3.15 for example) and the coarse grain microstructure CP zone has an average of 530 elements per grain near the notch root. The coarse grain model employs the fine grain mesh size in a localized region near the notch root ($0.15\rho$ away from notch root, where $\rho$ is the notch root radius) and contains a gradient mesh that gradually increases to the coarse grain size at the outside barrier of the crystal plasticity zone. The modeling strategy for simulated double edge-notched specimens is summarized in Figure 3.16.

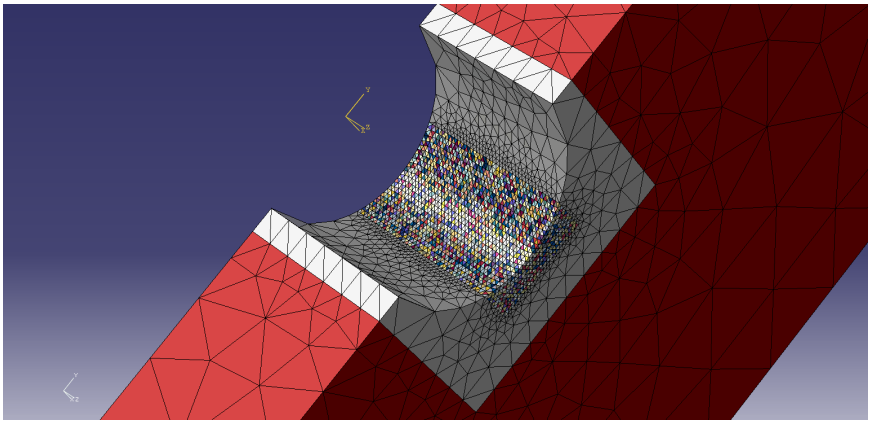

**Figure 3.15:** Assignment of grains for fine grain microstructure for a notch root radius of 0.2 mm.

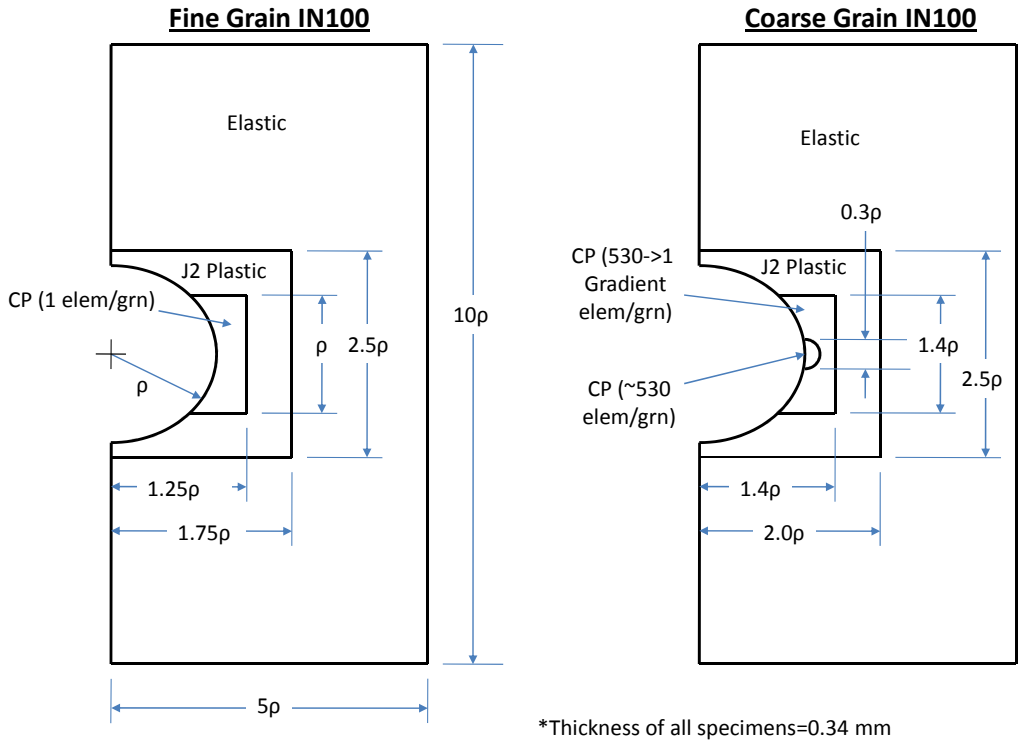


**Figure 3.16:** Modeling strategy for fine grain and coarse grain IN100 microstructures.

### 3.5.2 Polycrystalline Model Reconstruction

The fine grain shape is idealized as tetrahedral while the coarse grains employ a spherical packing algorithm to fit the grains to a lognormal distribution. The reason this algorithm was used was because it offers more control over grain sizing as compared to a more traditional random seed Voronoi type tessellation, which results in a normal distribution. The lognormal distribution takes the form:

$$f(x;\mu,\sigma) = \frac{1}{x\sigma\sqrt{2\pi}} \exp\left[\frac{-(ln(x)-\mu)^2}{2\sigma^2}\right] \tag{3.25}$$

The values of $\mu = -0.1$ and $\sigma = 0.4$ were chosen for the target lognormal distribution based on previous publications of fine grain IN100 grain size distributions [2,57,59,90]. The grain size distribution for the coarse grain microstructure is not available in the

literature, so the same normalized lognormal distribution was assumed. Also, as a first order approximation, the grain shape was assumed to be equiaxed. The goal of this research is to establish general trends of fatigue potency based on key microstructure attributes including grain size distribution. These computationally created microstructures can be considered as statistically representative volume microstructures that contain equiaxed grain structures. In addition, random grain orientations were assumed, lacking information regarding orientation distribution functions (ODF) and misorientation distribution functions (MODF) in the literature for the coarse grain microstructure.

Once the grain size distribution is known, a spherical packing algorithm was used. First, using the lognormal distribution function an array of sphere sizes was created based on random sampling from the distribution function. The number of spheres created is equal to the volume of the crystal plasticity region divided by the average grain size volume, i.e., $N_{grn} = \frac{V_{CP}}{<V_{grn}>}$. This ensures that the average volume of all grains is equal to the target overall average volume of the microstructure. In order to pack all of these spheres into the crystal plasticity volume, the volume of the spheres was decreased by 25% to account for the inherent packing factor of randomly placed spheres. In other words, when randomly packing spheres within a volume there is going to be open space between the spheres. The ratio of sphere volume over total volume is referred to as the packing factor. The reduced size spheres were placed inside the volume of the CP region in order of largest to smallest while ensuring no overlap between any two spheres. Next, the mesh created in ABAQUS [71] was superimposed in space on the spheres. Those elements that contained centroids that fell within a given sphere were assigned to that sphere as a grain. The remaining unassigned elements were assigned according to their proximity to the nearest spherical surface of a grain. This is analogous to uniform growth of each grain until all space is filled up. The general method for creation of the coarse grain IN100 polycrystalline structure

is illustrated in Figure 3.17. An example of a resulting grain size distribution using this technique is shown in Figure 3.18. As seen from Figure 3.18, the actual grain size distribution (solid line) takes the same shape as the target grain size distribution (dotted line) with minimal error.

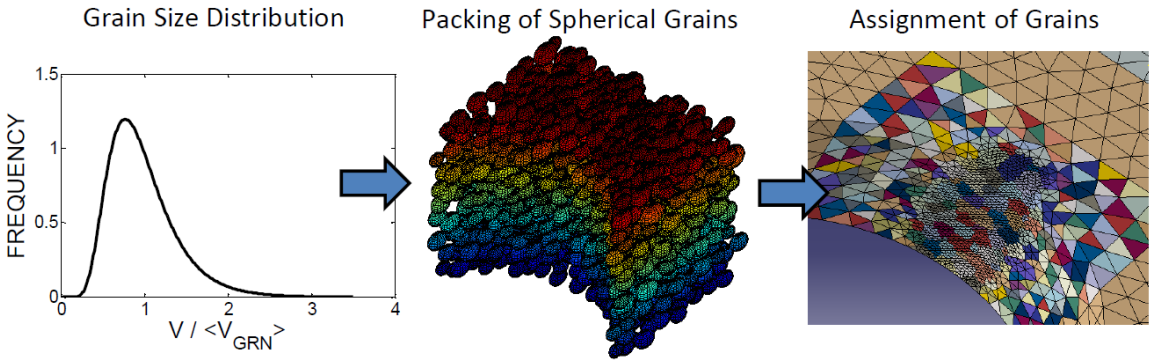


**Figure 3.17:** Method for creating spherical grains with given grain size distribution.

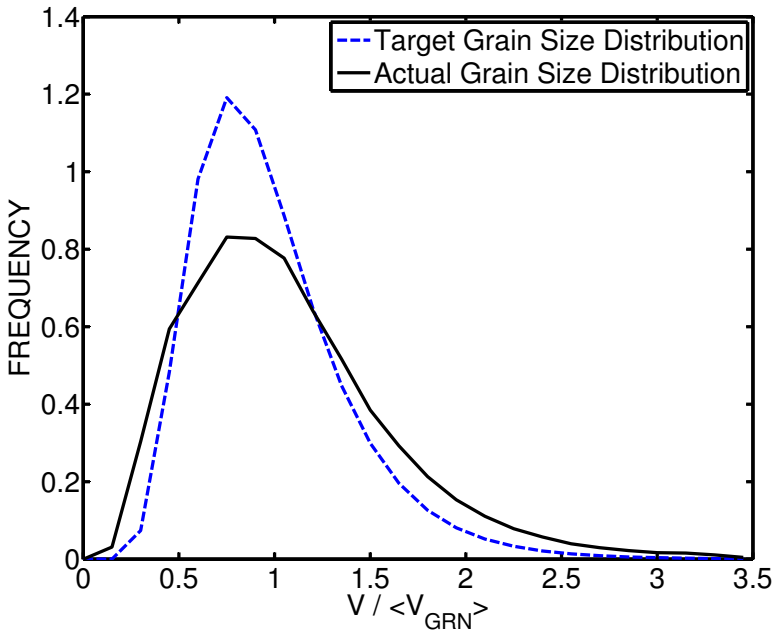


**Figure 3.18:** Actual vs. target coarse grain IN100 size distributions for a 0.8 mm notch root radius realization.

### 3.5.3 Mesh Size Convergence

#### *3.5.3.1 Coarse Grain (Super Weak) IN100*

To determine the necessary FIP averaging volume size and element size, a convergence study was performed on a 50 µm notched coarse grain specimen. Each grain was assigned a random crystallographic orientation and was maintained during mesh refinements. Tetrahedral elements were used because they are used for all models of the notched specimens since they work well for meshes with gradient mesh sizes. The disordered nature of tetrahedral element meshing can cause a large volume variance in grains between mesh refinements (ref. Figure 3.19) when using a traditional voronoi grain assignment method. Also, for the coarsest meshes, there may be some voronoi seeds without any assigned elements. Therefore, in this mesh refinement study, a modified voronoi tessellation approach was used to maintain consistency in grain size between mesh refinements. Prior to tetrahedral element meshing, the volume of the specimen was partitioned into mostly cuboidal grains. This resulted in identical grain element volumes among all convergence study simulations. The modified voronoi tessellation technique is shown in Figure 3.20.

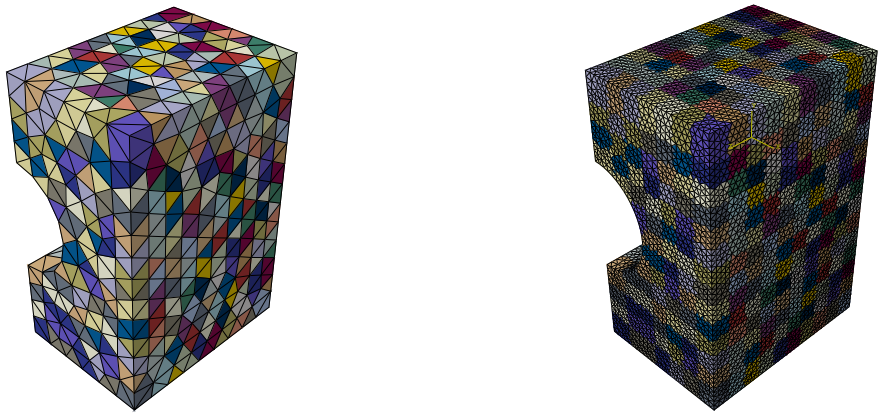

(a) 40 µm mesh seed size (∼ 6 elements/grain) (b) 10 µm mesh seed size (∼ 229 elements/grain)

**Figure 3.19:** Conventional voronoi tessellation grain assignment for a coarse mesh and fine mesh showing a large variation in grain volume due to mesh refinement. Each specimen contains a 100 µm notch.

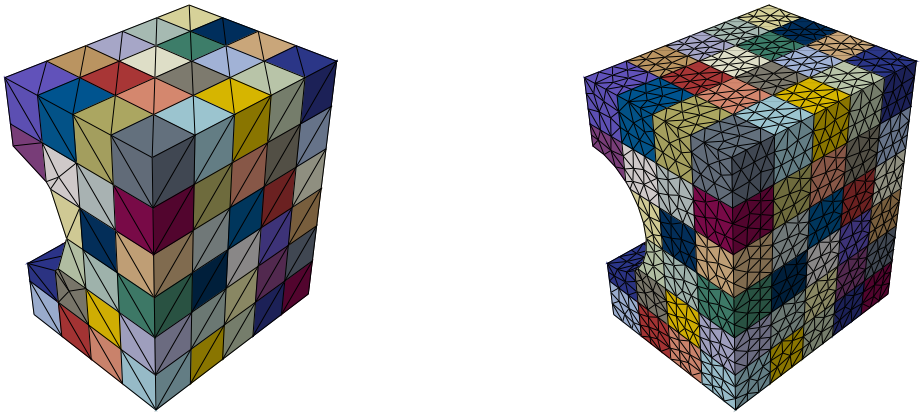

(a) 34 µm mesh seed size (∼ 13 elements/grain) (b) 11 µm mesh seed size (∼ 233 elements/grain)

**Figure 3.20:** Modified voronoi tessellation grain assignment of a coarse and fine mesh showing no variation in grain volume due to mesh refinement. Each specimen contains a 50 µm notch.

For the purposes of the convergence study, FIP values were averaged over the entire grain. The specimens were fatigue cycled under displacement control with a strain ratio $R_\epsilon = -1$, a strain rate $\dot{\epsilon} = 10^{-3}(s^{-1})$, and a strain amplitude of $\epsilon_a = 1.2\,\epsilon_y$, where $\epsilon_y^{CG} = 0.42\%$ is the macroscopic proportional limit of the coarse grain IN100 microstructure, identified through experimental stress strain data. Four mesh seed sizes were used, namely, 34 µm (grain size), 17 µm (grain size/2), 11.3 µm (grain size/3), and 8.5 µm (grain size/4). These mesh seed sizes correspond to a minimum of 1, 2, 3, and 4 elements through the thickness of each grain, respectively. For comparison purposes, the grain averaged FIP for each grain are sorted from largest to smallest FIP to display the differences in mesh refinements (ref. Figure 3.21). As shown in Figure 3.21 there is great correlation between the FIP values when using 233 and 450 elements per grain (3 and 4 elements through the thickness of the grain). It is very interesting to note that there is a large difference in the maximum FIP value for the most coarse mesh. This can be due to the inability of a single element to capture the complex deformation behavior within a grain. The error between each

level of mesh refinement was calculated for each grain as

$$error_i = \frac{abs(FIP_i^{coarse\ mesh} - FIP_i^{refined\ mesh})}{max(FIP_{all}^{coarse\ mesh}, FIP_{all}^{refined\ mesh})} \tag{3.26}$$

These errors were then averaged for each level of mesh refinement. The results are shown in Table 3.5.

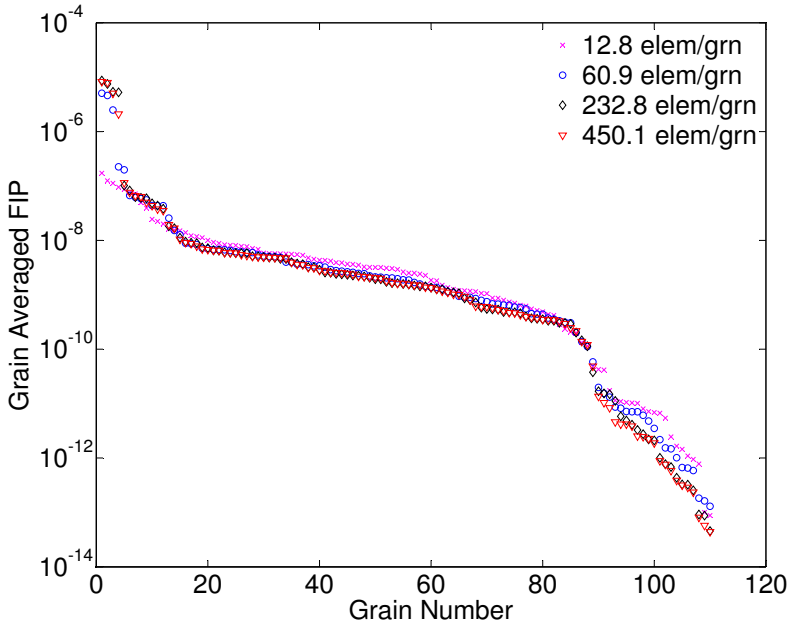


**Figure 3.21:** Grain averaged FIP sorted from largest to smallest as a function of grain number for coarse grain IN100. $R_\epsilon = -1$, $\rho = 0.05\,\text{mm}$, $\dot{\epsilon} = 10^{-3}(s^{-1})$, $\epsilon_a = 1.2\ \epsilon_y$.

From this study, a minimum of 3 tetrahedral elements through the thickness of a grain (11.3 µm mesh seed size) is recommended for the coarse grain IN100 microstructure to obtain a converged average FIP value over each grain. This mesh resulted in an average error of 0.5% in FIP calculation as compared to the model with 4 tetrahedral elements through the thickness of the grain. In addition to the grain scale mesh convergence study, element scale convergence can be qualitatively shown from contour plots. Figure 3.22 shows the contour plots of Von Mises equivalent stress and effective plastic strain for the 4 mesh cases used in this study. The contour plots are from the maximum tensile load during the third fatigue cycle. The Von Mises

**Table 3.5:** Mesh convergence study results for coarse grain and fine grain IN100

| Elements through grain thickness | Mesh seed Size(mm) | Average number of elements per grain | Maximum FIP over grain | Average FIP error over grain |
|---|---|---|---|---|
| Coarse Grain IN100: | | | | |
| 1 | 0.034 | 12.8 | 1.72e-7 | 2.2% |
| 2 | 0.017 | 60.9 | 5.05e-6 | 1.5% |
| 3 | 0.011 | 232.8 | 8.69e-6 | 0.5% |
| 4 | 0.009 | 450.1 | 8.22e-6 | - |
| Fine Grain IN100: | | | | |
| 1 | 0.0042 | 12.8 | 5.08e-4 | 1.5% |
| 2 | 0.0021 | 61.0 | 3.44e-4 | 1.6% |
| 3 | 0.0014 | 231.9 | 2.00e-4 | 0.7% |
| 4 | 0.0011 | 444.7 | 1.73e-4 | - |

uniaxial equivalent stress is given by $\overline{\sigma} = \frac{1}{\sqrt{2}}\sqrt{(\sigma_1 - \sigma_2)^2 + (\sigma_2 - \sigma_3)^2 + (\sigma_3 - \sigma_1)^2}$ while the cumulative Von Mises effective plastic strain is $\overline{\epsilon}^p = \sqrt{\frac{2}{3}\epsilon^p_{ij}\epsilon^p_{ij}}$. The values of effective plastic strain below a value of $\overline{\epsilon}^p = 10^{-7}$ were dropped from the contour plots to display the heterogeneity of plastic slip in the microstructure. This value was chosen because it is on the same order of magnitude as the FIP threshold in which the grain level response transferred from an elastic to elastic/plastic condition as shown in Figure 3.13. Also in Figure 3.22, the same scale was used for each refinement to show the differences in contour plots among mesh refinements. Based on these contour plots, convergence of the Von Mises stress and the effective plastic strain at the element scale is obtained for a mesh seed size of 11.3 µm, which is identical to the results shown at the grain scale. Therefore, a mesh seed size that is less than or equal to 11.3 µm (3 elements through the thickness of the grain; 233 elements per grain) is recommended for coarse grain IN100 in order to capture the complex deformation behavior within a grain. For the parametric studies on the notched specimens used in the current work, a mesh seed size of 8 µm is used because it corresponds to the fine grain mesh size.

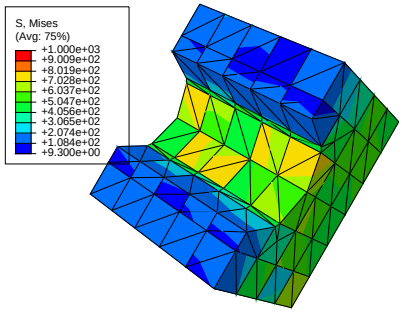


(a) Von Mises - 34 µm seed

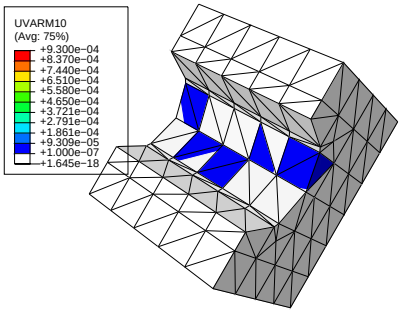


(b) Effective Plastic Strain - 34 µm seed

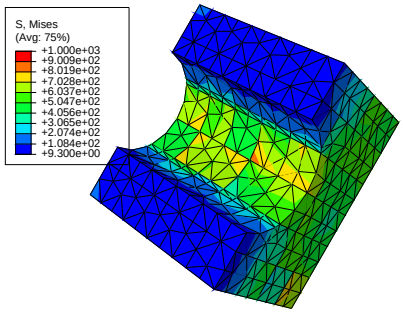


(c) Von Mises - 17 µm seed

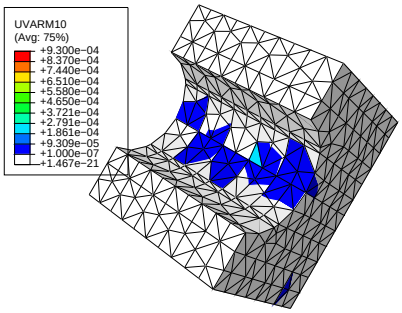


(d) Effective Plastic Strain - 17 µm seed

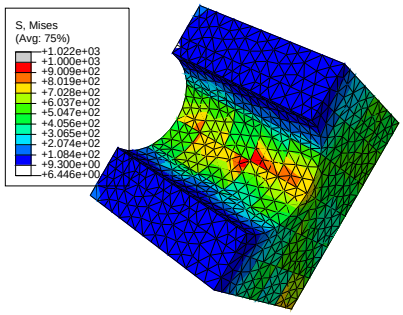


(e) Von Mises - 11 µm seed

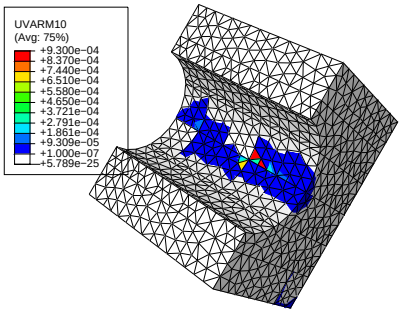


(f) Effective Plastic Strain - 11 µm seed

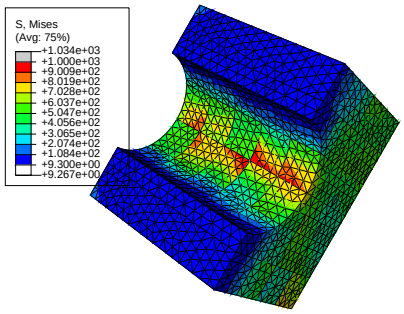


(g) Von Mises - 9 µm seed

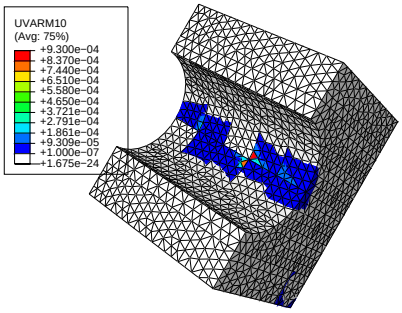


(h) Effective Plastic Strain - 9 µm seed

**Figure 3.22:** Coarse grain IN100 contour plots used for mesh convergence study.

#### *3.5.3.2 Fine Grain (Sister Disk) IN100*

The maximum possible element size for the fine grain IN100 microstructure is its grain size. This seed size ($a$) is chosen so that the tetrahedral volume is equal to the volume of a cube with side lengths equal to the grain size ($d_{grn}$), i.e.

$$V_{grn}^{tetrahedron} = \frac{\sqrt{2}}{12}a^3 = {d_{grn}}^3 = V_{grn}^{cube} \tag{3.27}$$

Thus, based on Equation 3.27, an 8 μm tetrahedral seed size is equivalent to a 4.2 μm cubic seed size. Applicability of continuum crystal plasticity becomes suspect at scales below 1 μm due to its homogenization of both dislocation substructures and slip banding; this sets the lower limit of mesh size. Similar to the previous section, a convergence study was performed on the fine grain IN 100 microstructure. The results for the fine grain averaged FIP convergence are shown in Table 3.5 and Figure 3.23. The contour plots of Von Mises equivalent stress and effective plastic strain are shown in Figure 3.24. As shown in these figures and tables, convergence is obtained both for the grain scale averaged FIP and the elemental scale for a mesh seed size of 1.4 μm (3 elements through the thickness of the grain; 232 elements per grain). However, using a mesh size of 1.4 μm will be too computationally intensive for the present purposes of this project. To compare the different microstructures (coarse grain and fine grain IN100) in a consistent manner, the same element size and averaging volume needs to be used. Therefore, the equivalent tetrahedral fine grain mesh size of 8 μm will be used for both microstructures. This mesh size provides convergence for the coarse grain model, but is lacking convergence in the fine grain model. This mesh size requires the least amount of computational time to maintain the physically-based crystal plasticity model. It is recognized that this assumption involves a limitation of the resolution that can be achieved of the intragranular slip distribution in the fine grain case, but it is necessary to facilitate parametric studies that include multiple microstructure instantiations/realizations for each notch root

radius to build up statistics to demonstrate the methodology.

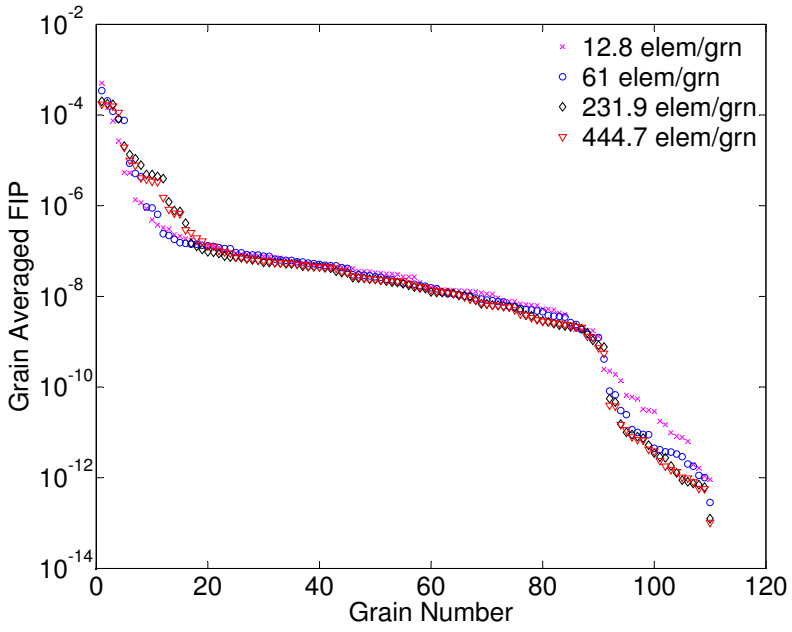


**Figure 3.23:** Grain averaged FIP sorted from largest to smallest as a function of grain number for fine grain IN100. $R_\epsilon = -1$, $\rho = 0.006\,\text{mm}$, $\dot{\epsilon} = 10^{-3}(s^{-1})$, $\epsilon_a = 1.2\,\epsilon_y$.

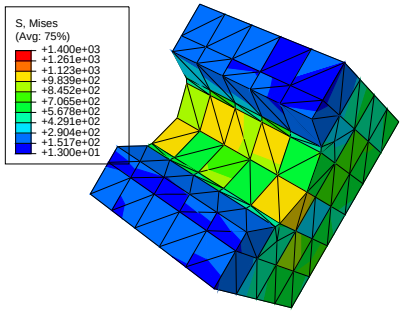


(a) Von Mises - 4.2 µm seed

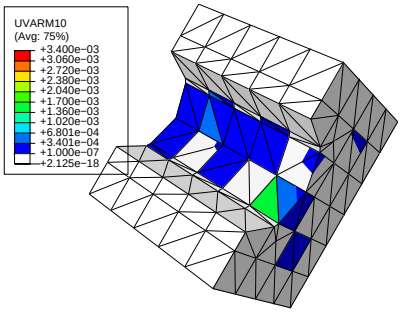


(b) Effective Plastic Strain - 4.2 µm seed

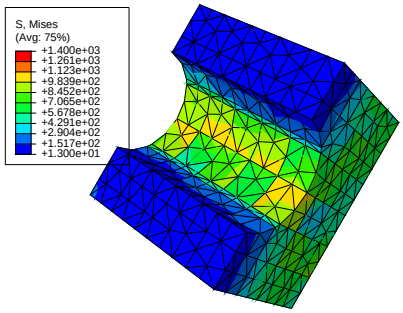


(c) Von Mises - 2.1 µm seed

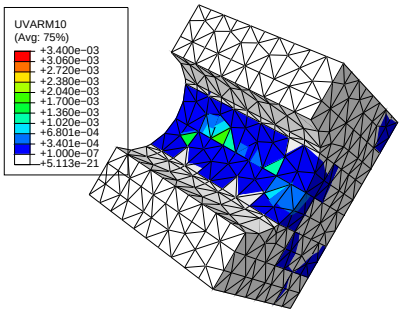


(d) Effective Plastic Strain - 2.1 µm seed

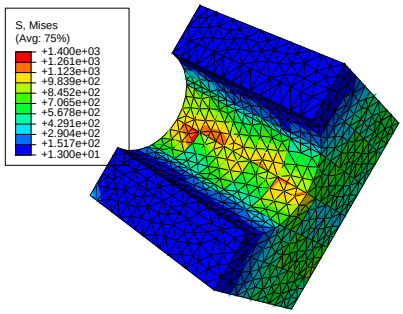


(e) Von Mises - 1.4 µm seed

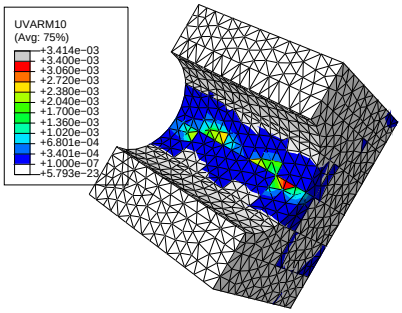


(f) Effective Plastic Strain - 1.4 µm seed

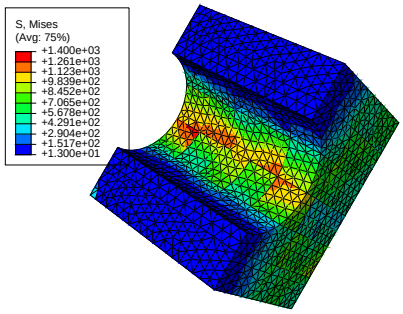


(g) Von Mises - 1.1 µm seed

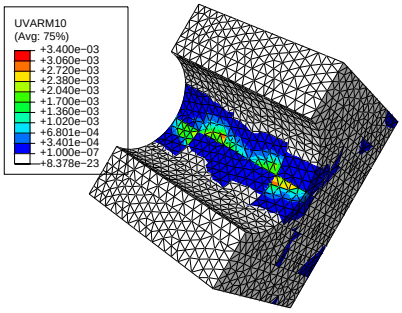


(h) Effective Plastic Strain - 1.1 µm seed

**Figure 3.24:** Fine grain IN100 contour plots used for mesh convergence study

### 3.5.4 Loading and Boundary Conditions

For application to Ni-base superalloys, simulations of 20 different realizations per notch root radius were performed on the coarse grain and fine grain IN100 microstructures. The specimens were fatigue cycled under displacement control with a strain ratio $R_\epsilon = -1$, a strain rate $\dot{\epsilon} = 10^{-3}(s^{-1})$, and various strain amplitudes ($\epsilon = 0.4\ \epsilon_y$, $\epsilon = 0.5\ \epsilon_y$, and $\epsilon = 0.6\ \epsilon_y$), where $\epsilon_y^{CG} = 0.42\%$ and $\epsilon_y^{FG} = 0.60\%$ are the macroscopic proportional limits of the coarse grain and fine grain microstructures, respectively, identified through experimental stress strain data. The fatigue indicator parameters were calculated over the third fatigue cycle. A summary of the loading and boundary conditions is shown in Figure 3.25 and Table 3.6. The height ($H = 10\rho$) and width ($W = 10\rho$) of the double edge-notched specimens depend on the notch root size ($\rho$).

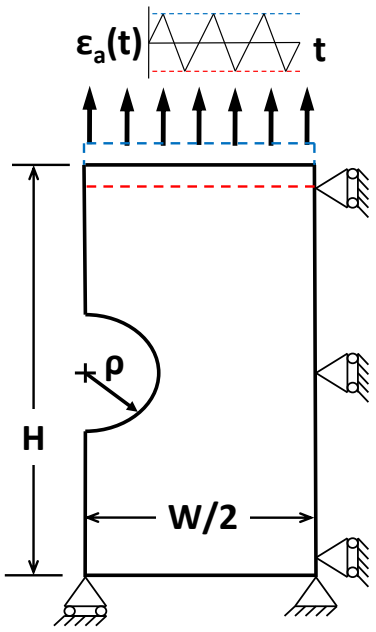


**Figure 3.25:** Loading and Boundary Conditions for Simulations.

**Table 3.6:** Geometric and Loading Variables and Material Constants

| Variables | |
|---|---|
| Microstructure | CG, FG |
| Notch Radius - $\rho$ (mm) | 0.2, 0.4, 0.6, 0.8, 1.0 |
| Strain Amplitude ($\epsilon_a$ / $\epsilon_y$) | 0.4, 0.5, 0.6 |
| **Constants** | |
| Proportional Limits | $\epsilon_y^{CG} = 0.42\%, \epsilon_y^{FG} = 0.60\%$ |
| Strain Rate | $\dot{\epsilon} = 10^{-3}(s^{-1})$ |
| R-Ratio (strain-controlled) | $R_\epsilon = -1$ |

### 3.5.5 Contour Plots of Stress and Plastic Strain within Notch Root Region

Prior to application of the probabilistic framework, it is useful to view the grain structure and the resulting contour plots of stresses and equivalent plastic strains within the notch root region for a fine grain and coarse grain IN100 microstructure. Only data from the crystal plasticity region were recorded during the large scale simulation process, since the crystal plasticity region within the notch root is the area of interest. Prior to these large scale simulations, a few simulations were performed in which the stresses and strains for all elements were recorded. In these simulations it was found that there were no severe discontinuities in the stress and strain response at the CP/J2 and J2/EL boundaries due to the differences in material modeling constitutive response. In other words, the crystal plasticity region size was chosen to be large enough so that the overall response of the localized crystal structure response was elastic at the boundary between the crystal plasticity and J2 plasticity regions. The J2 plasticity region was required in order to smear the anisotropic elastic behavior of the outer edge of the crystal plasticity zone to a fully isotropic elastic condition.

The results for a coarse grain and a fine grain IN100 notched specimen are shown in Figures 3.26 and 3.27, respectively. As stated previously, the Von Mises uniaxial equivalent stress is given by $\overline{\sigma} = \frac{1}{\sqrt{2}}\sqrt{(\sigma_1 - \sigma_2)^2 + (\sigma_2 - \sigma_3)^2 + (\sigma_3 - \sigma_1)^2}$ while the

cumulative Von Mises effective plastic strain is $\overline{\epsilon}^p = \sqrt{\frac{2}{3}\epsilon_{ij}^p \epsilon_{ij}^p}$. The contour plots show the Von Mises equivalent stress and effective plastic strain for the maximum tensile load during the third cycle. The values of effective plastic strain below a value of $\overline{\epsilon}^p = 10^{-7}$ were dropped from the contour plots to display the heterogeneity of plastic slip in the microstructure. This value was chosen because it is on the same order of magnitude as the lower bound FIP behavior which will be described in Section 3.4.5.2. As expected, the effective plastic strain is most significant at certain grain boundaries, which is due to the incompatibility of deformation between grains of different orientation.

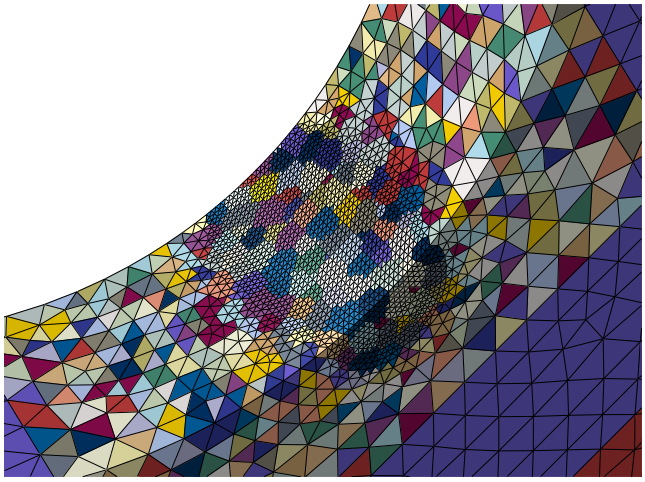

(a) Grain Structure

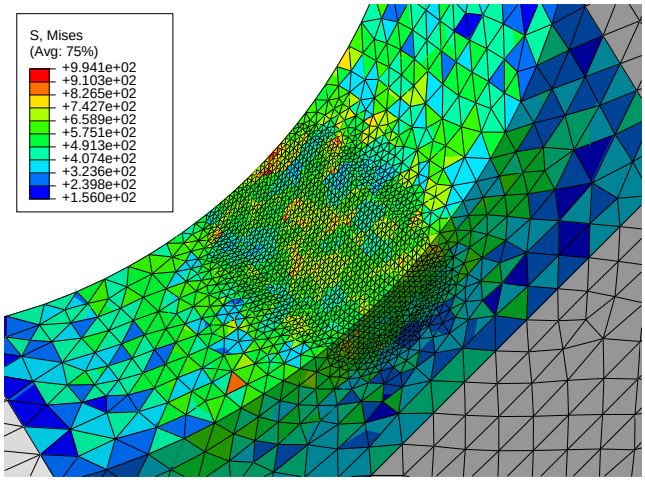


(b) Von Mises Stress

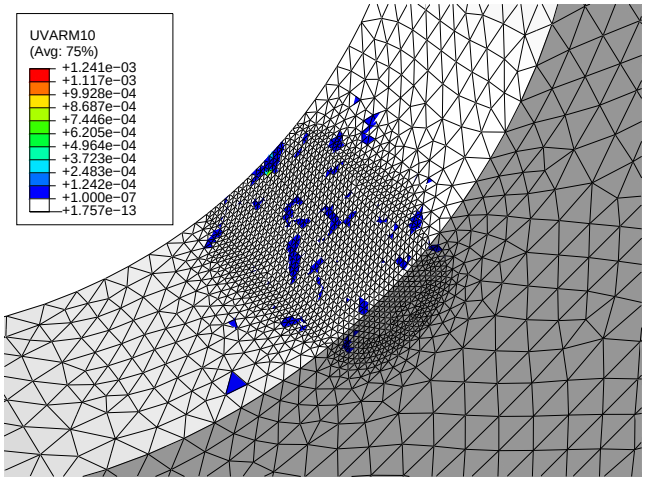


(c) Effective Plastic Strain

**Figure 3.26:** Coarse Grain IN100 Contour Plots - $\rho = 0.6\,\text{mm}$, $\epsilon_a = 0.6\epsilon_y$.

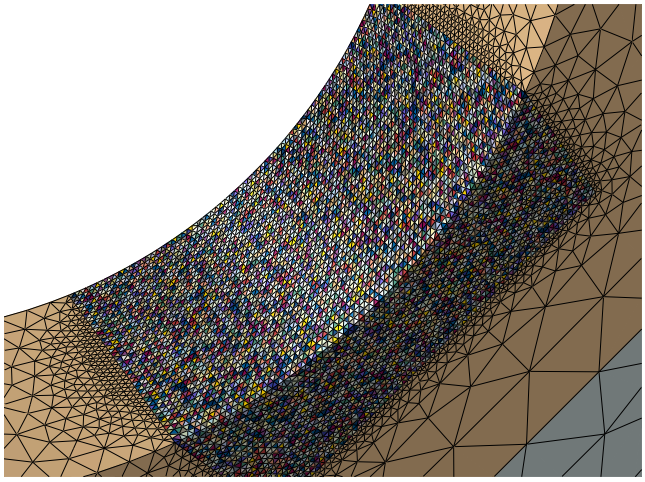

(a) Grain Structure

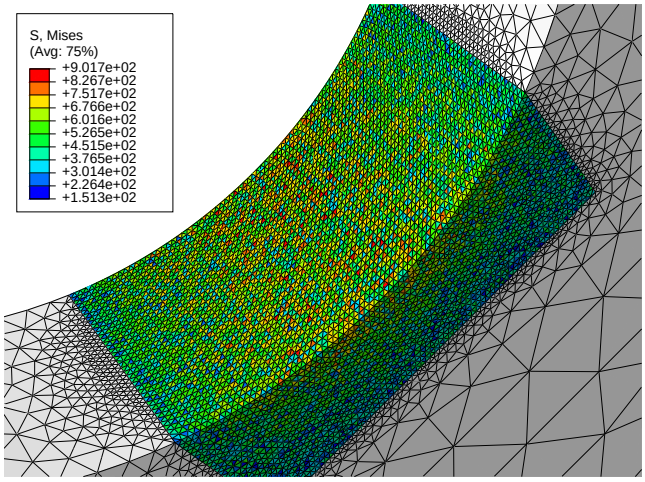


(b) Von Mises Stress

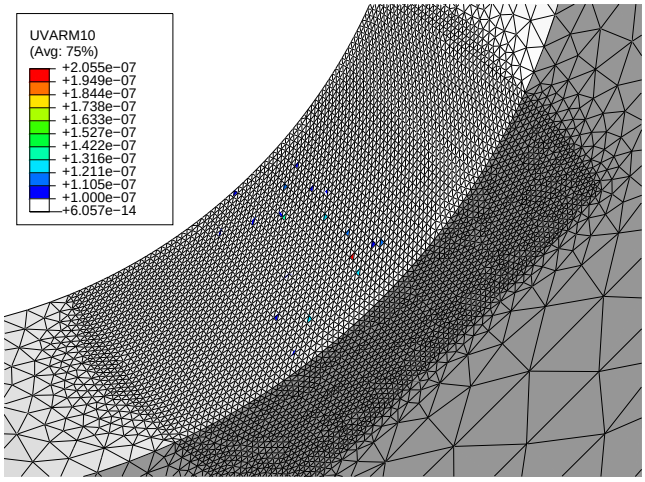


(c) Effective Plastic Strain

**Figure 3.27:** Fine Grain IN100 Contour Plots - $\rho = 0.6\,\text{mm}$, $\epsilon_a = 0.4\epsilon_y$.

## 3.6 Summary

In this chapter, the key microstructure features of the Ni-base superalloy IN100 are reviewed. Two different microstructures are considered, a fine grain and a coarse grain IN100. A computational crystal plasticity [1] model based on physical mechanisms of deformation and particle strengthening is used to inform the fatigue potency of notched specimens through the use of multiaxial fatigue indicator parameters, such as the maximum plastic shear strain range and Fatemi-Socie parameters. This model is used in conjunction with the probabilistic models introduced in the following chapter to estimate a microstructure-sensitive fatigue notch factor.

# CHAPTER IV

# PROBABILISTIC FATIGUE NOTCH TECHNIQUES

## 4.1 Introduction

Many of the most recent probabilistic approaches for fatigue crack initiation have placed an emphasis on including the effects of the size distribution of defects such as inclusions, the proximity of these defects to the surface, and the competition between these mechanisms [45, 47, 50, 53, 54]. It can be imagined that in the presence of many different fatigue damage mechanisms occurring simultaneously, one could propose a total probability of component failure function that is a superposition of all $n$ number of active fatigue mechanisms, i.e., $P_{f,t}(x) = P_I f_I(x) + P_{II} f_{II}(x) + ... + P_n f_n(x)$. In order to do this, however, the probability density function of each mechanism must be known. Experimentally performing parametric studies in order to distinguish each individual mechanism can be a very daunting task, especially for extremely complicated microstructures such as the Ni-base superalloys in this study. Also, the statistically weakest "defect" size within a volume can change with the size of the volume [47, 49]. Finite element analysis can be used to qualitatively compare each failure mechanism and determine the relative contribution of each mechanism to the overall fatigue failure response. Concepts previously introduced within our group [4] are extended to include the effects of the notch root gradient field and local microstructure effects on the formation and growth of fatigue cracks to the scale of the transition crack length. Therefore, the goal of this probabilistic framework is to characterize the microstructurally-sensitive notch root effect on the high cycle fatigue life of notched components. The intent of this research is to use probabilistic techniques to improve the prediction of HCF fatigue life of notched components employing materials with

complex microstructures.

The idea of a fatigue indicator parameter (FIP) was introduced in the previous Chapter to describe the Stage I, shear-dominated formation and growth of small fatigue cracks. The computational crystal plasticity model described previously is used in this section to determine the FIP distribution functions within the notch root region as a function of notch root size and applied strain amplitude. These distributions are applied to the probabilistic framework described here to find the overall probability of failure of the component and to find a microstructure-dependent probabilistic fatigue notch factor. Two different probabilistic frameworks are investigated in this work: (1) The "Grain Scale Approach" is based on preliminary efforts within our research group [4] and considers the probability of crack formation within a grain; (2) The "FIP-Based Transition Crack Length Approach" considers the FIP intensity over a characteristic length scale to estimate the probability that a crack will form and propagate from the notch root to a transition crack length.

## 4.2 Grain Scale Approach

The grain scale approach is an extension of previous work by Owolabi et al. [4]. In this approach, failure is defined as the formation of a crack on the order of grain size. This method is applicable in the high cycle fatigue regime because a majority of life is spent forming a crack to the grain scale. The microstructure effect on the fatigue notch resistance reduction is taken into account by the distribution of FIPs ($\Delta\Gamma$) within a damage process zone, defined as the smallest contiguous volume ($V_d$) enclosing grains with FIP levels above some threshold level (ref. Figure 4.1).

### 4.2.1 Framework

#### *4.2.1.1 Probability of Failure*

Imposing weakest link theory, Weibull statistics, and the assumption that the fatigue driving force parameter, ($\Delta\Gamma$), is a random variable, the probability of formation and

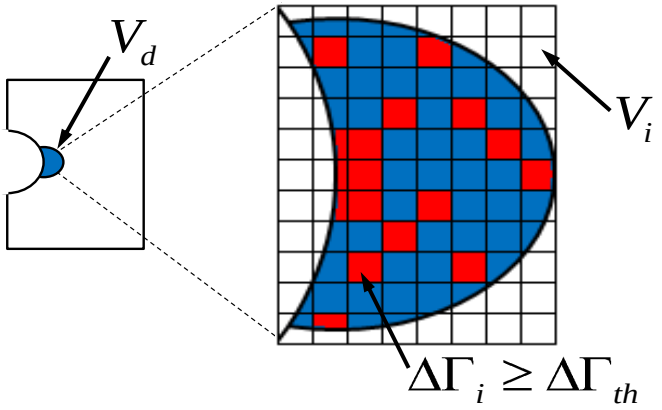


**Figure 4.1:** Schematic showing definition of damage process zone ($V_d$).

growth of a crack takes the form [4]:

$$P_f = 1 - \exp\left\{-\frac{1}{V_o}\int_{V_d}\left\langle\frac{\Delta\Gamma(\epsilon_a \; or \; \sigma_a, R, r) - \Delta\Gamma_{th}(\epsilon_a \; or \; \sigma_a, R, r)}{\Delta\Gamma_o(\epsilon_a \; or \; \sigma_a, R, r)}\right\rangle^{b_\Gamma} dV\right\} \quad (4.1)$$

where $V_o$ is the volume of a reference smooth specimen, $\Delta\Gamma_o$ is the scale parameter, $b_\Gamma$ is the shape parameter, $V_d$ is the damage process zone, and $\Delta\Gamma_{th}$ is the threshold FIP below which no microdamage will occur at a given number of cycles in the HCF regime. Note that Equation 4.1 is of the same form as the Weibull distribution function introduced in the Background section (ref. Equation 2.23). However, this distribution function is based on physically motivated parameters that have been correlated to fatigue crack propagation data of nickel-base superalloy specimens subjected to complex multiaxial loading conditions with and without hold times [72, 73].

The threshold FIP value is found using MSC Equation 3.17 and the assumption that at the threshold, no crack growth is expected, i.e., $da/dN = 0$. This results in the threshold condition

$$\Delta\Gamma_{th} = \frac{\eta b}{A_{FS}\tau_y a} \quad (4.2)$$

Since cracks typically form at the surface of a notch, we consider the crack length $a$ in Equation 4.2 to be equivalent to the grain size $d_{grn}$ of each microstructure. Using values of $A_{FS} = 8.1\text{x}10^{-4}\,(\,\text{MPa}-cycle)^{-1}$ [2], $\eta = 1$, $b = 0.25\,\text{nm}$, $\tau_y^{FG} = (1025/\text{M})\,\text{MPa}$,

$\tau_y^{CG} = (750/\mathrm{M})\,\mathrm{MPa}$ (where M=3.08 is the Schmid factor for a random FCC polycrystalline aggregate [79]), $d_{grn}^{FG} = 4.2\,\mu\mathrm{m}$, and $d_{grn}^{CG} = 34\,\mu\mathrm{m}$ [55], the threshold FIP values for the fine grain and coarse grain IN100 are $\Delta\Gamma_{th}^{FG} = 2.21\mathrm{x}10^{-4}$ and $\Delta\Gamma_{th}^{CG} = 3.73\mathrm{x}10^{-5}$, respectively.

As indicated in the Equation 4.1, the cyclic FIP values are a function of the strain or stress amplitude ($\epsilon_a$ *or* $\sigma_a$), stress ratio $R$, and the distance from the notch root $r$. For simplification, these dependencies are removed from further derivations, but are implicitly inferred. Applying the concept of an effective volume ($V_{eff} = k\,V_{th}$), Equation 4.1 can be rewritten as:

$$P_f = 1 - \exp\left\{-\frac{kV_{th}}{V_o}\left(\frac{\Delta\Gamma_{max}}{\Delta\Gamma_o}\right)^{b_\Gamma}\right\} \tag{4.3}$$

$$where \;\; k = \left(\frac{\sum_{n=1}^{n_{th}} \langle \Delta\Gamma - \Delta\Gamma_{th}\rangle^{b_\Gamma}}{(\Delta\Gamma_{max})^{b_\Gamma}}\right) \tag{4.4}$$

In this equation, $n_{th}$ denotes the number of subvolumes at or above the threshold FIP and $V_{th}$ is the sum of all these subvolumes given by $V_{th} = \sum_{i=1}^{n_{th}} V_i$. Consequently, by the definition of $V_d$ and $V_{th}$, $V_{th}/V_d < 1$.

#### *4.2.1.2 Microscopic Fatigue Notch Factor*

The formulation of the microscopic fatigue notch factor is similar to that proposed in [4] with a few modifications. For this approach, a modified version of the CDF formulation in Equations 4.3 and 4.4 is used, i.e.,

$$P_f = 1 - \exp\left\{-\frac{K_\Gamma^\mu\, V_{th}}{V_o}\left(\frac{\Delta\overline{\Gamma}_{max}}{\Delta\Gamma_o}\right)^{b_\Gamma}\right\} \tag{4.5}$$

$$where \;\; K_\Gamma^\mu = \left(\frac{\sum_{n=1}^{n_{th}} \langle \Delta\Gamma - \Delta\Gamma_{th}\rangle^{b_\Gamma}}{\left(\Delta\overline{\Gamma}_{max}\right)^{b_\Gamma}}\right) \tag{4.6}$$

where $\Delta\overline{\Gamma}_{max} = \Delta\Gamma_{max} - \Delta\Gamma_{th}$. The traditional fatigue notch factor is the ratio of unnotched to notched fatigue strength at the same probability of failure (usually

50%). Therefore, the probability of failure of a smooth (unnotched) specimen and a notched specimen will be the same when

$$\frac{K^{\mu}_{\Gamma,N}\ V_{th,N}}{V_o}\left(\frac{\Delta\overline{\Gamma}_{max,N}}{\Delta\Gamma_o}\right)^{b_\Gamma} = \frac{K^{\mu}_{\Gamma,S}\ V_{th,S}}{V_o}\left(\frac{\Delta\overline{\Gamma}_{max,S}}{\Delta\Gamma_o}\right)^{b_\Gamma} \tag{4.7}$$

where the subscripts $N$ and $S$ denote the respective values for a notched and smooth specimen. The ratio of smooth to notched microscopic fatigue driving force parameters (FIP values) are used to construct a microscopic fatigue notch factor of the form

$$K^{\mu}_{f} = \frac{\Delta\overline{\Gamma}_{max,S}}{\Delta\overline{\Gamma}_{max,N}} = \left(\frac{K^{\mu}_{\Gamma,N}\ V_{th,N}}{K^{\mu}_{\Gamma,S}\ V_{th,S}}\right)^{1/b_\Gamma} \tag{4.8}$$

For the case of a smooth specimen that is loaded at a lower strain amplitude (HCF regime), the number of critically stressed grains will be significantly low. Considering the life-limiting case in which only one grain with volume $V_{grn}$ is critically stressed above the threshold FIP value, the value of $K^{\mu}_{\Gamma,S} = 1$. Therefore, a new quantitative definition of the fatigue notch factor for the formation and growth of a crack on the order of the grain size in HCF is obtained as

$$K^{\mu}_{f} = \left(K^{\mu}_{\Gamma,N}\frac{V_{th,N}}{V_{grn}}\right)^{1/b_\Gamma} \tag{4.9}$$

This $K^{\mu}_{f}$ value follows the essence of the traditional definition of $K_f$, i.e., the ratio of unnotched to notched values of driving force for a given HCF life and same probability of failure, but is rooted in probabilistic arguments. In [4], this probabilistic model was applied to polycrystalline OFHC copper and adequately predicted the trends observed in the experimental results for the average values of the notch sensitivity as a function of the notch root radius.

### 4.2.2 Estimation of Parameters

There are a few different means to estimate the parameters of the Weibull distribution. Typical techniques include the least squares technique (2-parameter Weibull only), the maximum likelihood estimation (MLE) [91], and the moments estimation (ME) [92].

For this investigation, the modified moment estimation (MME) technique is used as outlined in Cohen et al. [93] and more recently in Whitten et al. [94]. The mean $\Delta\bar{\Gamma}_m$ and variance $\Delta\bar{\Gamma}^2_{var}$ are found by modifying expressions in the MME method used in [94] to account for notch size effect. These expressions are given by

$$\Delta\bar{\Gamma}_m = \Delta\Gamma_o \left(\frac{V_o}{kV_{th}}\right)^{\frac{1}{b_\Gamma}} \zeta_1 \tag{4.10}$$

and

$$\Delta\bar{\Gamma}^2_{var} = \Delta\Gamma^2_o \left(\frac{V_o}{kV_{th}}\right)^{\frac{2}{b_\Gamma}} \left(\zeta_2 - \zeta_1^2\right) \tag{4.11}$$

In Equations 4.10 and 4.11, $\zeta_j = \zeta\left(1 + \frac{j}{b_\Gamma}\right)$ where $j = 1, 2$ and $\zeta(\cdot)$ is the gamma function defined by

$$\zeta(s) = \int_0^\infty t^{s-1} e^{-t} dt \tag{4.12}$$

Fully three-dimensional finite element analysis was used to find the $\Delta\Gamma$ distribution and solve for the probability of failure at the scale of a grain.

### 4.2.3 Computational Results

The resulting probability of failure and corresponding microscopic fatigue notch factor versus notch size is shown in Figures 4.2 and 4.3, respectively. Also plotted in these Figures is the shape of the estimated distribution functions of $P_f$ and $K_f^\mu$ as a function of notch root radius using a kernel density smoothing function (KDF) [92]. Each geometry has the same theoretical elastic stress concentration, $K_t = 2.41$, based on the net cross section. As indicated in Figure 4.3, the average microscopic fatigue notch factor as a function of notch size takes on a characteristic sigmoidal shape and varies significantly with notch size. At an applied strain amplitude of 0.6 times the proportional limit, a notch root size of 1.0 mm does not reach the full theoretical elastic stress concentration, $K_t$, value. However, this $K_f^\mu$ is related to the distribution of microplasticity whereas the traditional $K_f$ is based on stress. Therefore, the microscopic and macroscopic fatigue notch factors may not be directly comparable. At

the same amplitude, notch sizes of less than 0.5 mm show little effect on the overall fatigue strength behavior. These trends need to be compared to experiments and perhaps a few more simulations need to be run at a higher strain amplitude to further verify these results. Also, notch sizes larger than 1 mm should be run in order to investigate whether the microscopic fatigue notch factor merges with the macroscopic one.

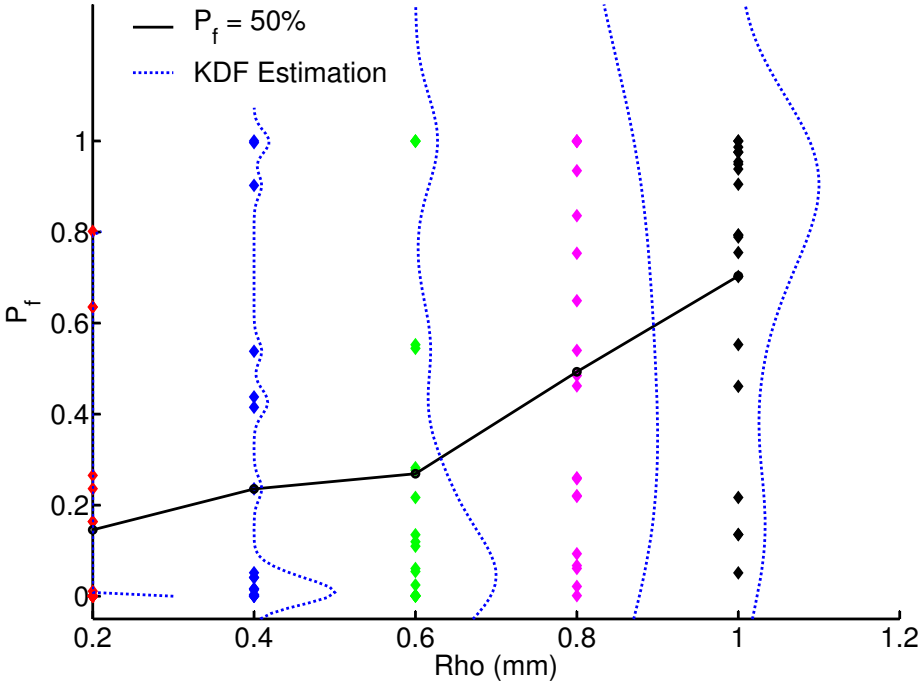


**Figure 4.2:** Probability of failure vs. notch root radius for 20 different instantiations of coarse grain IN100 ($\epsilon_a = 0.6\ \epsilon_y$, $\sigma_a = 450$ MPa).

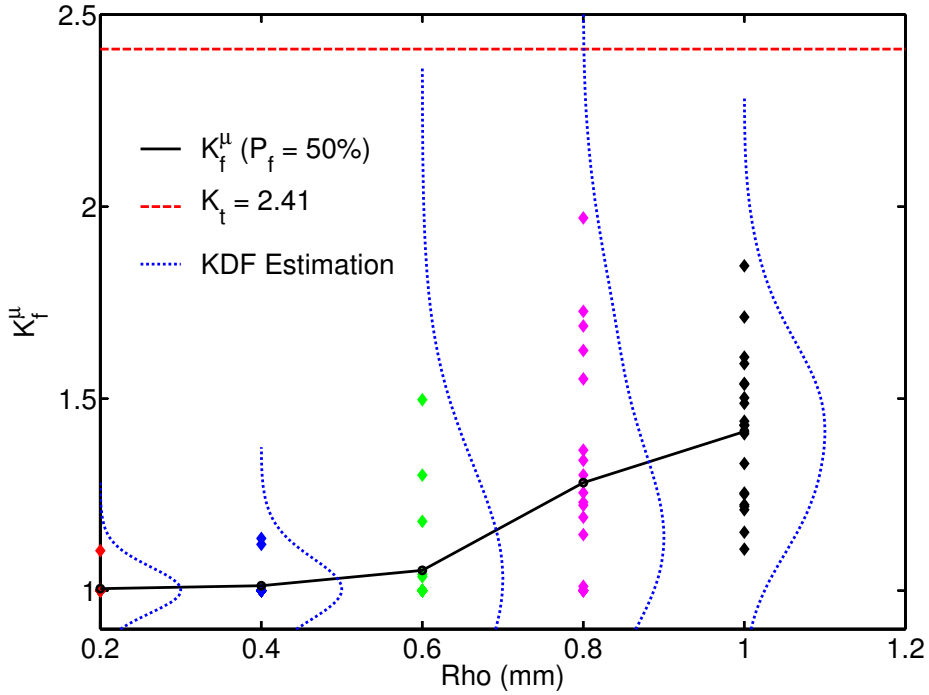


**Figure 4.3:** Microscopic fatigue notch factor vs. notch root radius for 20 different instantiations of coarse grain IN100 ($\epsilon_a = 0.6\ \epsilon_y$, $\sigma_a = 450\,\text{MPa}$).

### 4.2.4 Applications of Grain Scale Approach

One of the limitations of this approach is that it is hard to verify the $K_f^\mu$ experimentally because it is difficult to nondestructively measure crack formation at the scale of a grain. Also, the traditional $K_f$ incorporates crack formation and growth to specimen failure, which is not accounted for in this framework. Another issue is that this framework is not applicable in the low cycle fatigue and transition fatigue regimes, where a majority of the life is spent in small crack growth across multiple grains and coalescence to failure. Regardless of these limitations, this probabilistic approach can be used for qualitative comparison of various notch geometries for a range of microstructures (including ones that have not already been processed). To account for the formation and small crack growth regimes of failure, the FIP distribution over the transition crack length approach was developed.

## 4.3 FIP-Based Transition Crack Length Approach

This approach considers the probability of forming and growing a crack to transition crack length, $L_d$. Once the crack length exceeds the transition crack length, linear elastic fracture mechanics (LEFM) techniques can be applied. Therefore, the number of cycles to crack initiation (from a fracture mechanics standpoint) constitutes the number of cycles to crack incubation $N_{inc}$ combined with the number of cycles to propagate the incubated crack from an initial size at crack incubation to the transition crack length, denoted by $N_{Ld}$. The number of cycles required to form the initial crack on the order of grain size can be found from previous techniques [2] based on the distribution of microplasticity within grains (ref. Equation 3.14). Thus, the total number of cycles to failure can be found as $N_f = N_{inc} + N_{Ld} + N_{LEFM}$.

The transition crack length is the distance in which a crack growing from a notch escapes the influence of the notch root stress concentration. In the present study, the definition of transition crack length follows that of Smith and Miller [95] with a few exceptions. For a semi-circular notch, using the Smith and Miller approach $L_d$ is equal to $0.13\rho$ [95]. For smaller notches that are less than 0.5 mm, this may only constitute 1 or 2 grain diameters in the present coarse grain IN100 microstructure. However, experiments have shown that crack growth data curves (da/dN vs. $\Delta K$) for small crack (EPFM) and long crack (LEFM) curves merge at crack lengths on the order of 3-10 grain diameters [12]. This is typically referred to as the microstructurally-small crack growth regime [12]. Therefore, a transition crack length in which LEFM is applicable must constitute at least 3 grain diameters. This value may be arbitrary depending on the grain size. For example, experiments on a fine-grained IN100 microstructure have shown that the transition from oscillatory microstructurally-small crack growth behavior to crack growth characteristic of LEFM occurs at a crack length of about 100 µm [96], which is on the order of 20-25 grain diameters for the fine grain microstructure. This transition length of 100 µm coincides with a value of

3 grain diameters for the coarse grain IN100 microstructure. Considering the above arguments, the transition crack length values used in this study are summarized in Table 4.1.

**Table 4.1:** Transition Crack Length Values

| Notch Size (mm) | $L_d$ (mm) |
|---|---|
| 0.2 | 0.100 |
| 0.4 | 0.100 |
| 0.6 | 0.100 |
| 0.8 | 0.104 |
| 1.0 | 0.130 |

### 4.3.1 Cumulative Distribution Function Framework

The proposed probability of failure of formation and growth of a crack to the transition crack length is a function of the applied stress amplitude, the notch root size, and the mechanisms of microstructurally small crack growth. Since the probability of formation of a crack on the order of transition crack length depends on the size of a preexisting crack at a given number of cycles, the cumulative distribution function (CDF) used in this analysis takes the form

$$CDF(S_a; L_d, N) = 1 - \exp\left[-\frac{\eta\ a_n}{L_d}\right] \tag{4.13}$$

where $S_a$ is the nominal applied stress and $a_n$ is the crack length at a given number of cycles $N$. The parameter $\eta = -\ln(0.5)$ provides normalization to the case for which the $CDF = 0.5$ when the crack reaches a transition crack length, $L_d$. The crack length $a_n$ can be found by integrating the da/dN crack growth relationship. The CDF becomes

$$CDF(S_a; L_d, N) = 1 - \exp\left[-\frac{\eta}{L_d}\int_{N_{inc}}^{N}\frac{da}{dN}dN\right] \tag{4.14}$$

where the assumed initial crack length ($a_i$) is the size at crack incubation, or on the order of the grain size in this study. A modified form of the microstructurally small

crack (ref. Equations 3.17 and 3.18) growth law da/dN is employed, i.e.,

$$\frac{da}{dN} = A_{FS}\ \tau_y\ \Delta\Gamma_{max}(x)\ a \tag{4.15}$$

where $\Delta\Gamma_{max}(x)$ is the maximum FIP value as a function of x-distance away from the notch root. The value of $\Delta\Gamma_{max}(x)$ is found through simulations and is associated with an exponential decay controlled by the parameter $\xi$, i.e.,

$$\Delta\Gamma_{max}(x) = \Delta\Gamma_{max}(0) \exp\left(\frac{-\xi x}{L_d}\right) \tag{4.16}$$

The exponential decay function in Equation 4.16 can be linearized by taking the natural log of each side of the equation, resulting in

$$\ln\left[\Delta\Gamma_{max}(x)\right] = \ln\left[\Delta\Gamma_{max}(0)\right] - \frac{\xi x}{L_d} \tag{4.17}$$

Thus, a log-linear plot of $\Delta\Gamma_{max}(x)$ versus $x$ distance from the notch root would result in a linear function. Plotted in Figure 4.4 is the distribution of the maximum fatigue indicator parameter, $\Delta\Gamma_{max}(x)$, as a function of $x$ distance from the notch root for different notch root sizes and the coarse grain IN100 microstructure. Also plotted in this Figure is the best fit line (Equation 4.17) for the data points located within a distance, $L_d$, from the notch root. As seen from the best fit lines in Figure 4.4, the parametrization of the maximum FIP value as an exponential decay with distance from notch root works well for the desired regime ($x = 0$ to $x = L_d$).

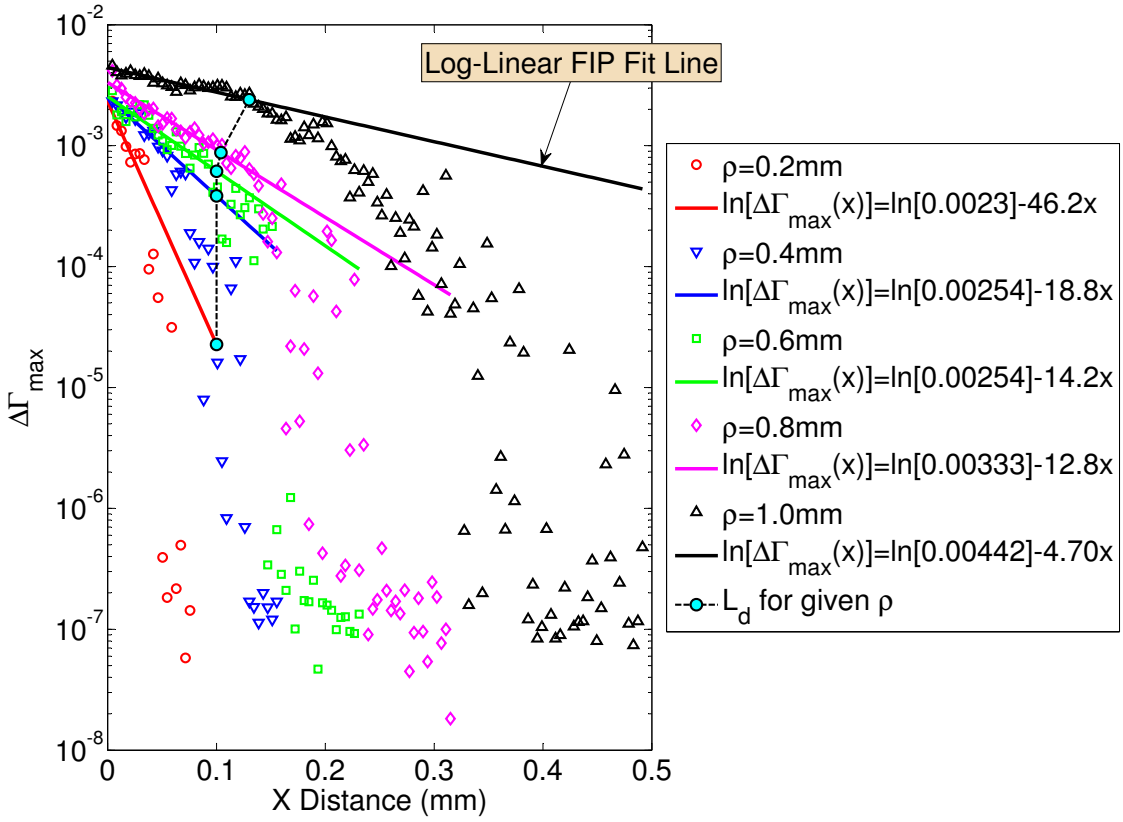


**Figure 4.4:** Maximum FIP distribution versus x-distance from notch root for 5 different notch root sizes for the coarse grain microstructure, strain amplitude $\epsilon = \epsilon_y$.

The exponential decay function (Equation 4.16), determined from the log-linear best fit (ref. Figure 4.4) of the FIP distribution, is used here to determine the CDF function for each simulation run. First, the FIP distribution is divided into $m$ discrete bins ($\Delta\Gamma_{max}(x_1)$, $\Delta\Gamma_{max}(x_2)$, ..., $\Delta\Gamma_{max}(x_m)$). Next, the number of cycles to incrementally grow a crack from bin $x_{j-1}$ to $x_j$ is determined by integrating and rearranging Equation 4.15, i.e.,

$$N_{prop,MSC}(a_{j-1} \rightarrow a_j) = \frac{\ln\left(\frac{a_j}{a_{j-1}}\right)}{A_{FS}\ \tau_y\ \Delta\Gamma_{max,ave}(x_{j-1}, x_j)} \tag{4.18}$$

Here, $A_{FS}$ is a parameter fit through experiments, $\tau_y$ is the critical resolved resolved shear stress given by $\tau_y = \sigma_y/M$, where $M$ is the Taylor factor, and $a_{j-1}$ and $a_j$ are the crack lengths at bins $x_{j-1}$ and $x_j$, respectively. Subsequently, the number of cycles

for each increment of crack propagation is determined and used to construct an $a_n$ versus number of cycles $N$ relationship. Finally, Equation 4.13 is used to determine the CDF as a function of the number of cycles, the remotely applied stress amplitude, and the transition crack length. This method for determining the CDF function for the transition crack length approach is summarized in Figure 4.5.

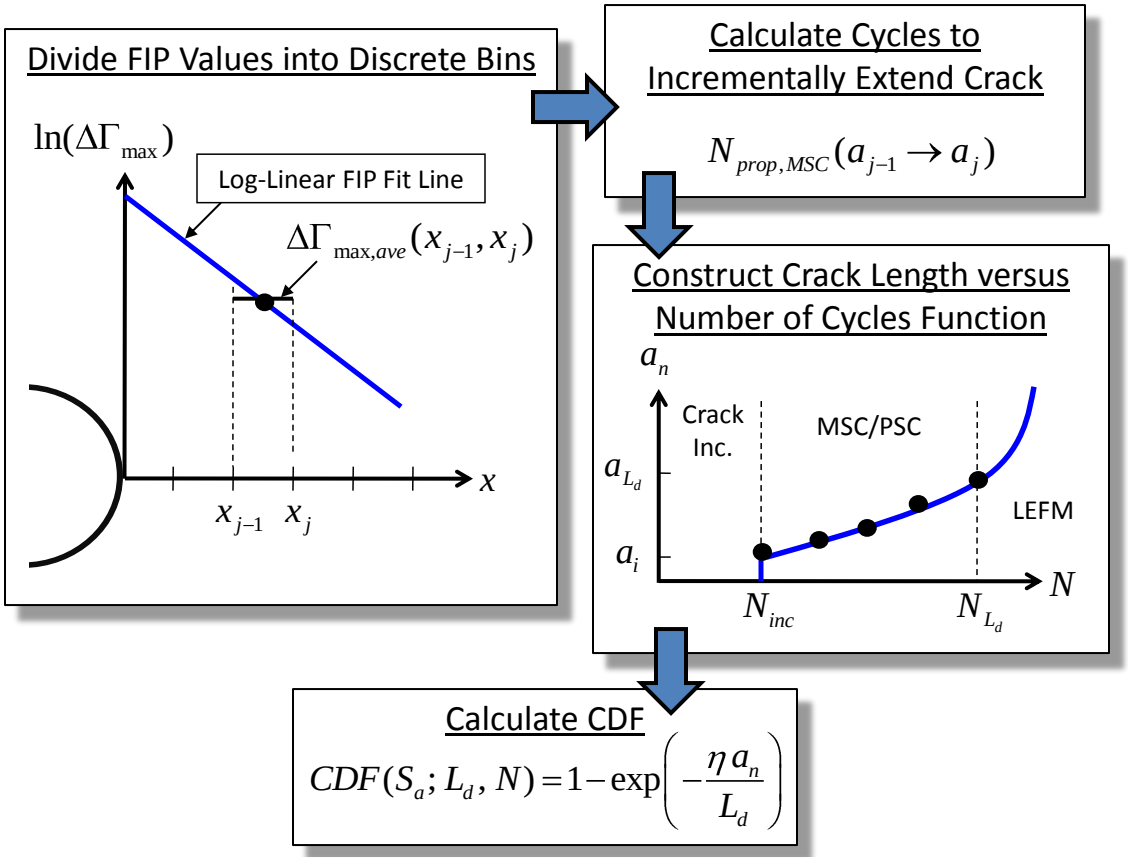


**Figure 4.5:** Method for determining CDF for transition crack length approach.

Once the crack reaches a transition crack length, LEFM conditions are used to determine crack extension. A modified form of the Paris-Erdogan equation is used, i.e.,

$$\frac{da}{dN} = C(\Delta K_{eff})^m \tag{4.19}$$

Here, crack growth is considered to occur only for the tensile portion of the loading cycle, i.e., $\Delta K_{eff} = Y\ S_a\sqrt{\pi a}$ and the constants employed are estimated from fine grain

IN100 long crack growth data ($C$ = 2x10$^{-7}$ and $m$ = 3.3 for T=650°C, f=0.33 Hz, R=0.05, and $\Delta K$ and da/dN are in units of MPa $-$ m$^{1/2}$ and mm/cycle [96]). It is noted that crack closure effects could be taken into account, but it is not the emphasis of the current study. Similar to previous arguments, the calculated propagation life determined through incremental iteration of the crack growth law is used. The general form for LEFM propagation life is given by

$$N_{prop,LEFM} = \frac{2}{(m-2)\ C\ Y^m\ S_a^m\ \pi^m} \left[ \frac{1}{a_i^{(m-2)/2}} - \frac{1}{a_f^{(m-2)/2}} \right] \tag{4.20}$$

### 4.3.2 Results and Comparison to Experiments

#### *4.3.2.1 FIP distribution versus distance from notch*

Plotted in Figure 4.4 above is the distribution of maximum FIP with respect to x-distance from the notch root for five different notch root sizes and the coarse grain microstructure. As seen in this plot, there is a significant difference in FIP intensity between the five different notch root sizes. In addition, the maximum FIP at the notch root is higher for larger notch sizes. This indicates that larger notch sizes have a higher probability of forming and propagating cracks to failure. Also plotted in Figure 4.4 are the logarithmic-linear fit lines for the maximum FIP level over the transition crack length. These lines are fit using least squares linear fitting. The least squares fitting lines were calculated for 20 simulations for each notch size (0.2 mm, 0.4 mm, 0.6 mm, 0.8 mm, and 1.0 mm) and each strain amplitude (0.4$\epsilon_y$, 0.5$\epsilon_y$, 0.6$\epsilon_y$). Comparing the least squares fitting of multiple instantiations indicates that there is a significant amount of scatter for the same notch root size and amplitude application (cf. Figure 4.6).

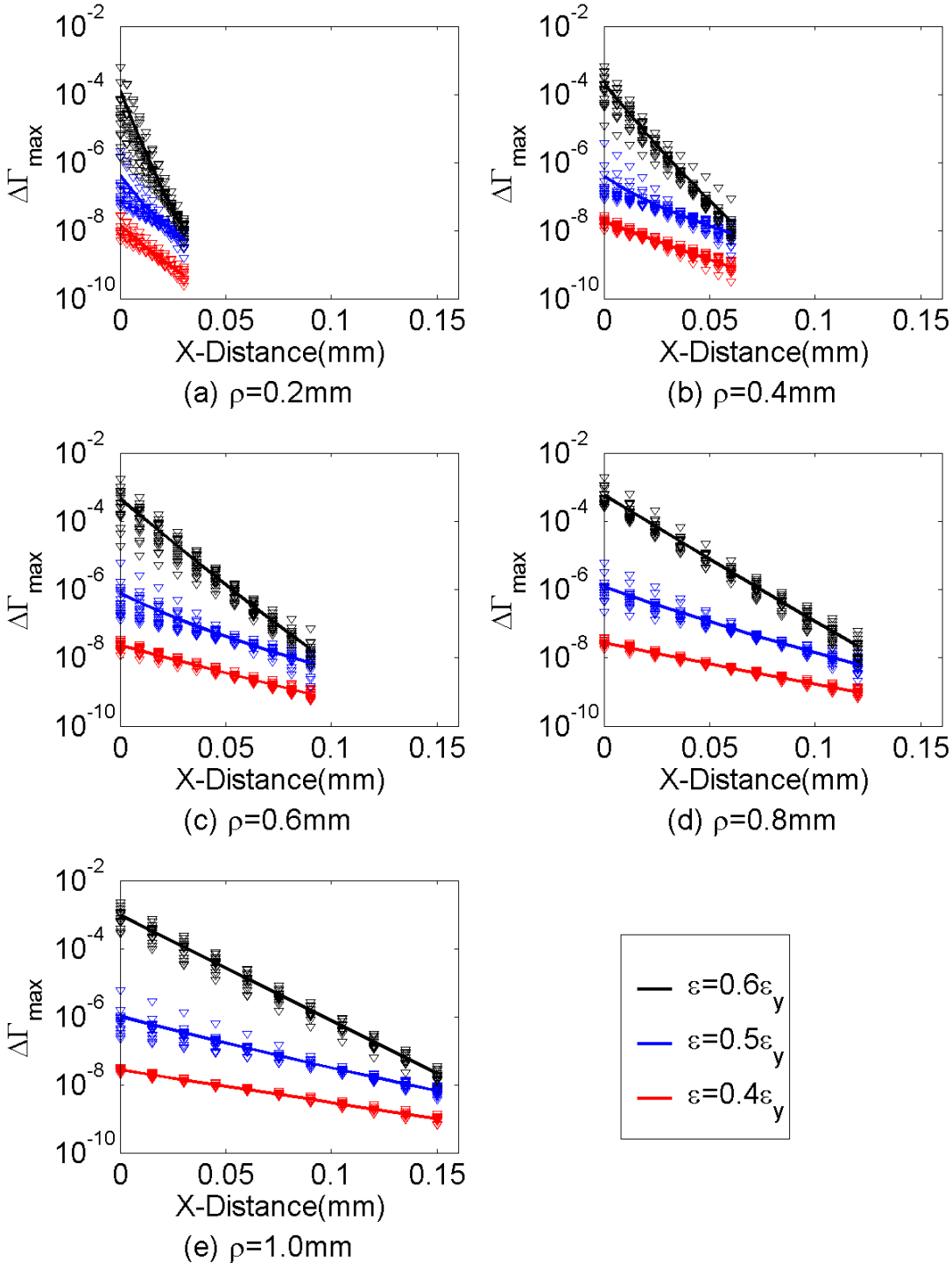


**Figure 4.6:** Logarithmic fit lines for maximum FIP vs. x-distance from notch for notch root radii of (a) $\rho = 0.2\,\text{mm}$, (b) $\rho = 0.4\,\text{mm}$, (c) $\rho = 0.6\,\text{mm}$, (d) $\rho = 0.8\,\text{mm}$ and (e) $\rho = 1.0\,\text{mm}$ at strain amplitudes of 0.4 $\epsilon_y$, 0.5 $\epsilon_y$, and 0.6 $\epsilon_y$.

Using the mean logarithmic fits (solid lines) in Figure 4.6 and replotting these curves on one plot versus a normalized x-distance away from the notch root, several interesting observations are made (Figure 4.7). First, at a given strain amplitude, the slope of these lines are virtually identical. Since these slopes are the same for each strain amplitude, the notch root size effect can clearly be deduced. Another notable feature is that the slopes of the lower applied strain amplitudes ($0.4\epsilon_y$ and $0.5\epsilon_y$) differ significantly from that of the higher applied strain amplitude ($0.6\epsilon_y$). As shown in the next section, this can indicate a transition from a very high cycle fatigue (VHCF) regime to a high cycle fatigue (HCF) regime.

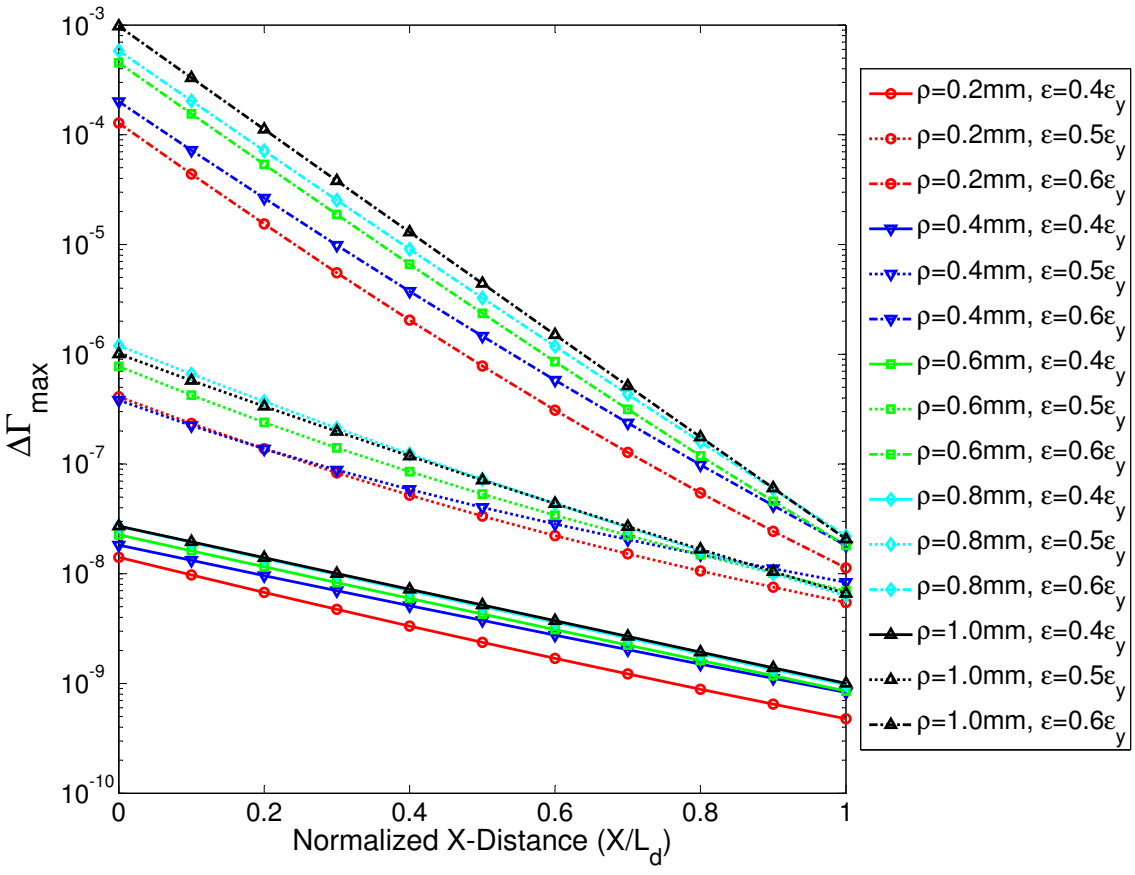


**Figure 4.7:** Mean value of logarithmic fit lines of maximum FIP vs. x-distance from notch normalized by transition crack length for five different notch root radii and strain amplitudes of 0.4 $\epsilon_y$, 0.5 $\epsilon_y$, and 0.6 $\epsilon_y$.

#### *4.3.2.2 Notched Specimen Strain-Life Data*

The crack "initiation" estimation techniques described previously (ref. Equation 3.14 and 3.19) are used here to compare the notched and smooth specimen strain-life data. The smooth specimen data are from experiments [83, 84, 86] and the computational data were created using the computational crystal plasticity model as previously discussed in Section 3.4.2 and 3.4.3. The coarse grain IN100 results are shown in Figures 4.8-4.12 for each notch root radius and Figure 4.13 compares the median data for all notch root sizes on a single plot. The median data point was used for comparison in this instance due to the large span of fatigue lives for a given strain amplitude. If the mean values were used, the behavior would be highly biased by the largest fatigue life value due to the logarithmic scale. As seen in the Figures, a notch effectively shifts the strain-life graph downward. It is interesting to note that the notch effect causes a significant drop in life for specimens loaded at a strain amplitude of $\epsilon_a = 0.6\epsilon_y$. For a smooth specimen loaded at this amplitude, a crack may not initiate even for a very high number of cycles ($10^9$ and beyond), if at all. This corresponds to the very high cycle fatigue range. On the other hand, a notched specimen at this strain amplitude exhibits a crack initiation life more consistent with the transition or HCF regime ($\sim 10^5 - 10^7$ cycles).

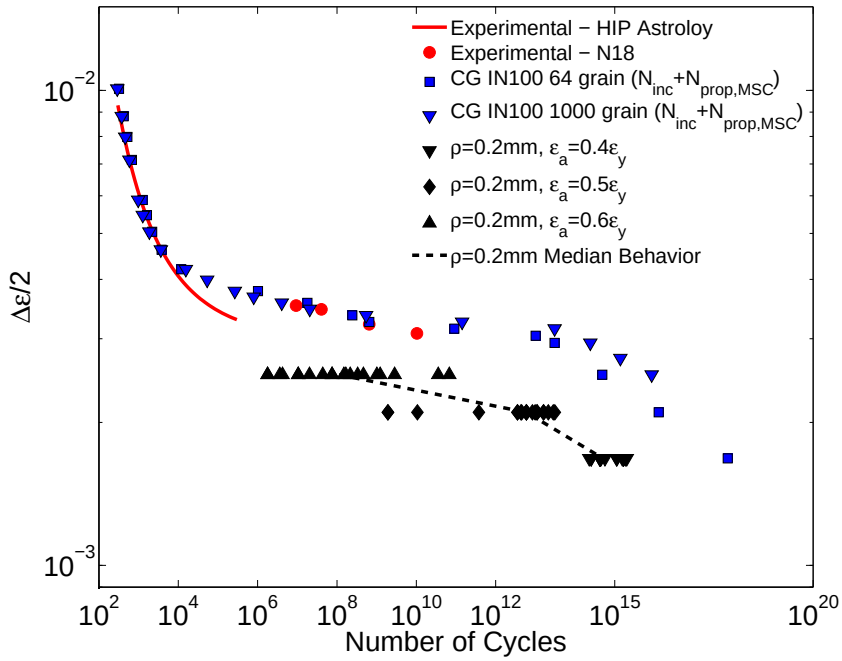


**Figure 4.8:** Coarse Grain IN100 strain-life plot comparing smooth and $\rho = 0.2\,\text{mm}$ notched specimens, $R_\epsilon = -1$.

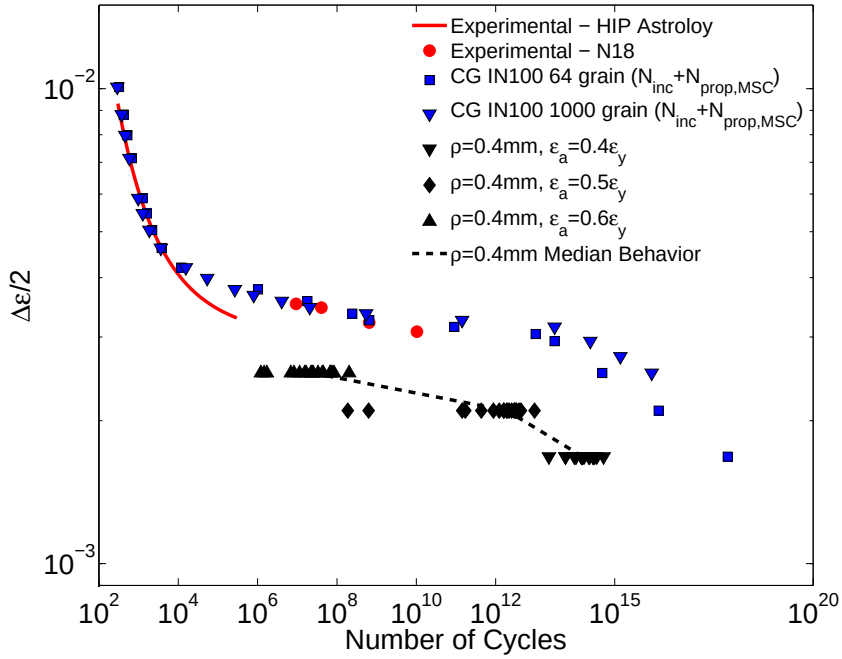


**Figure 4.9:** Coarse Grain IN100 strain-life plot comparing smooth and $\rho = 0.4\,\text{mm}$ notched specimens, $R_\epsilon = -1$.

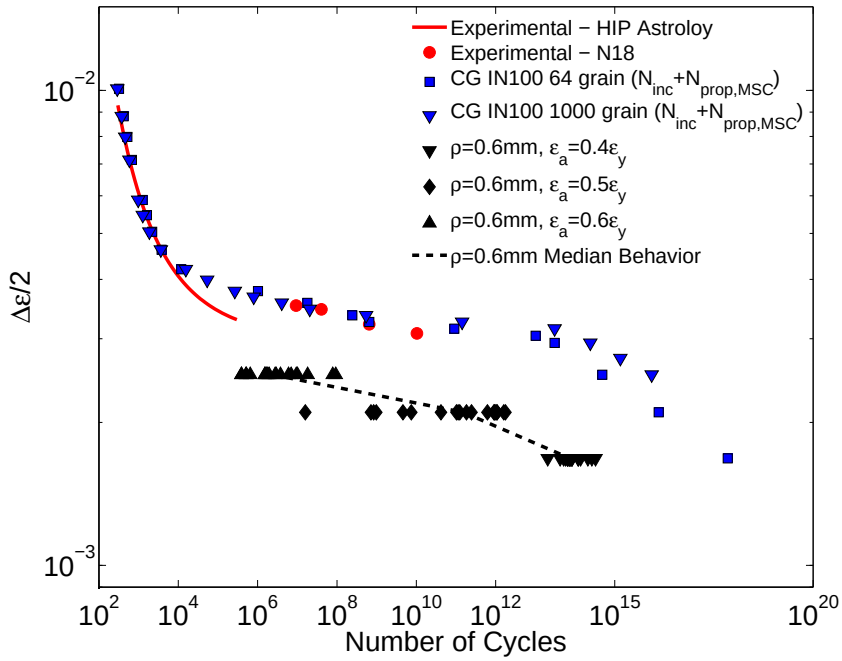


**Figure 4.10:** Coarse Grain IN100 strain-life plot comparing smooth and $\rho = 0.6\,\text{mm}$ notched specimens, $R_\epsilon = -1$.

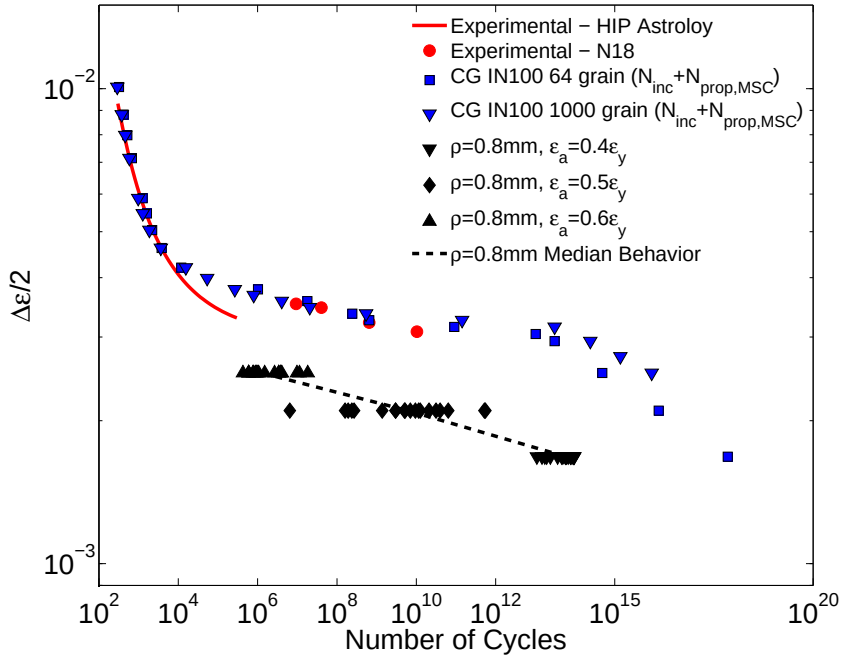


**Figure 4.11:** Coarse Grain IN100 strain-life plot comparing smooth and $\rho = 0.8\,\text{mm}$ notched specimens, $R_\epsilon = -1$.

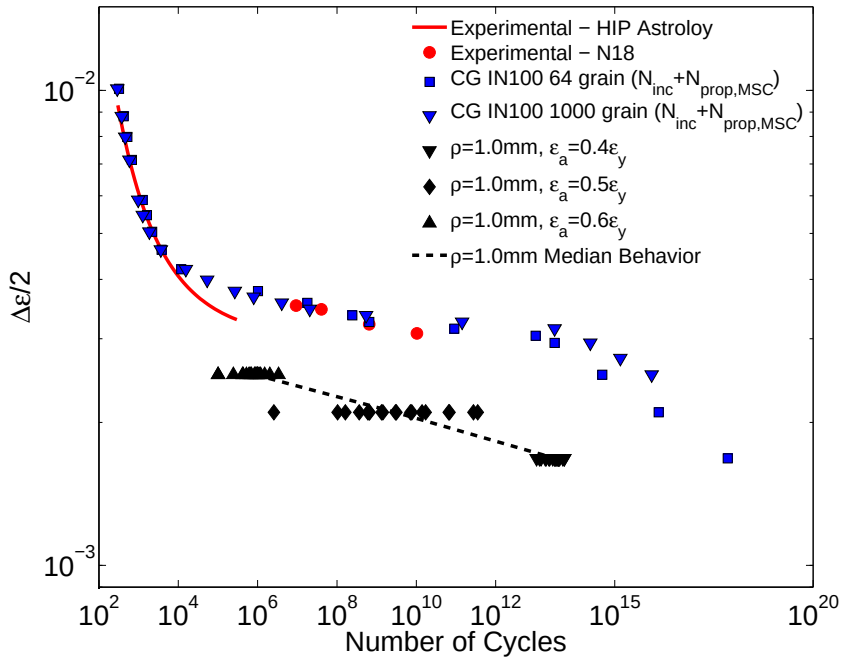


**Figure 4.12:** Coarse Grain IN100 strain-life plot comparing smooth and $\rho = 1.0\,\text{mm}$ notched specimens, $R_\epsilon = -1$.

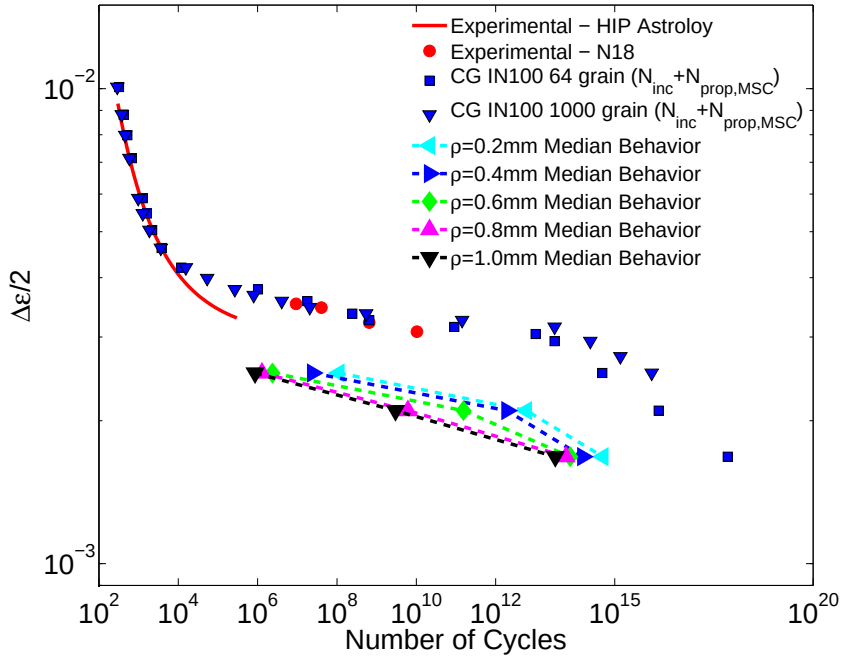


**Figure 4.13:** Coarse Grain IN100 strain-life plot comparing smooth and all notched specimens, $R_\epsilon = -1$.

#### *4.3.2.3 Cumulative distribution function*

Applying the above framework for 20 different instantiations per notch root radius of the coarse grain IN100, the results are shown in Figures 4.14-4.19. As can be seen from these Figures, the benefit of using this approach is that the cumulative distribution function can be calculated for any number of cycles and any probability of failure. This approach can be applied to low cycle fatigue (LCF), HCF and transition fatigue regimes to find the total component failure. Once the crack forms to the transition length, linear elastic fracture mechanics can be used to find the total component failure. This framework predicts that larger notch sizes will tend to fail before smaller notch sizes, which is consistent with general experimental trends. These computationally created cumulative distribution functions need to be compared with experiments.

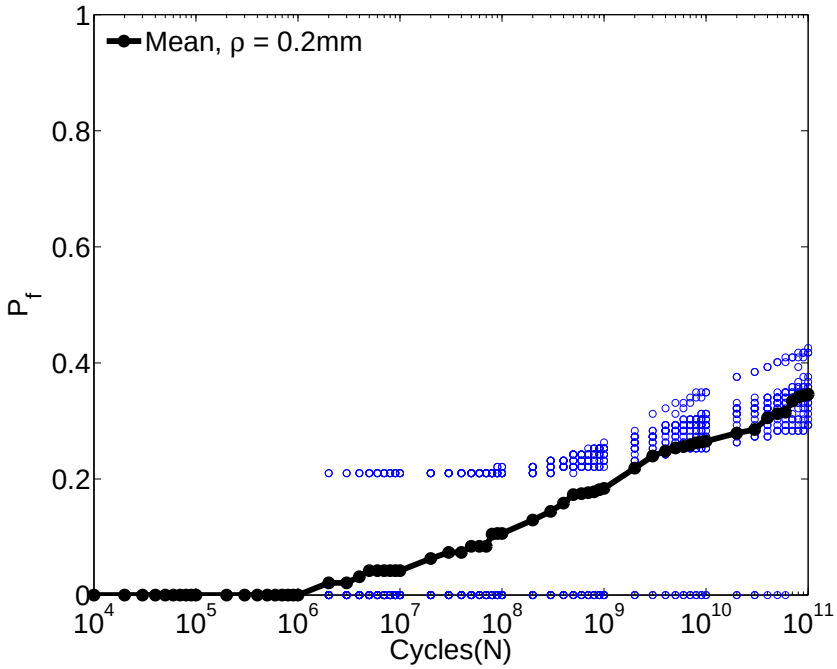


**Figure 4.14:** Cumulative distribution function for coarse grain IN100 with $\rho = 0.2\,\text{mm}$ ($\epsilon_a = 0.6\ \epsilon_y$, $\sigma_a = 450\,\text{MPa}$, $R_\epsilon = -1$).

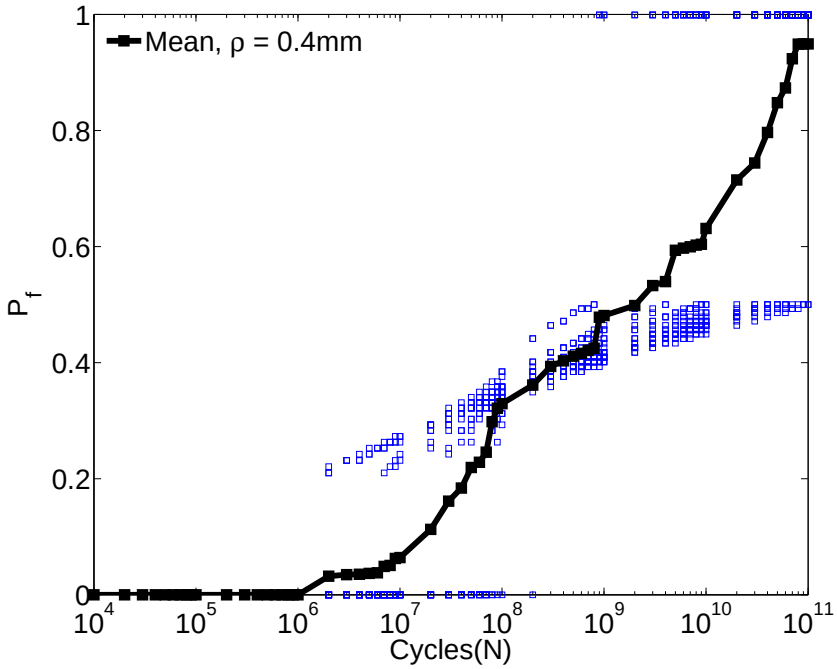


**Figure 4.15:** Cumulative distribution function for coarse grain IN100 with $\rho = 0.4\,\text{mm}$ ($\epsilon_a = 0.6\ \epsilon_y$, $\sigma_a = 450\,\text{MPa}$, $R_\epsilon = -1$).

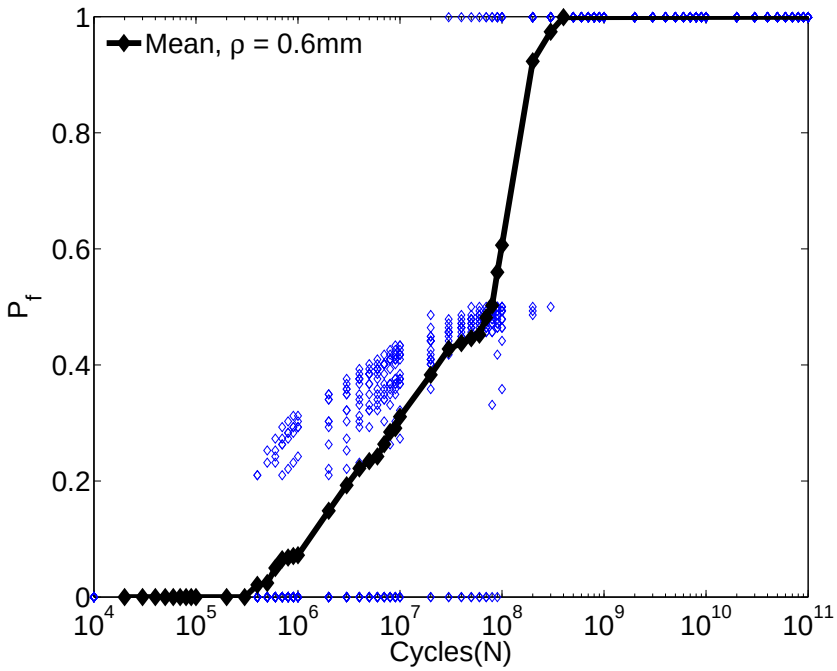


**Figure 4.16:** Cumulative distribution function for coarse grain IN100 with $\rho = 0.6\,\text{mm}$ ($\epsilon_a = 0.6\ \epsilon_y$, $\sigma_a = 450\,\text{MPa}$, $R_\epsilon = -1$).

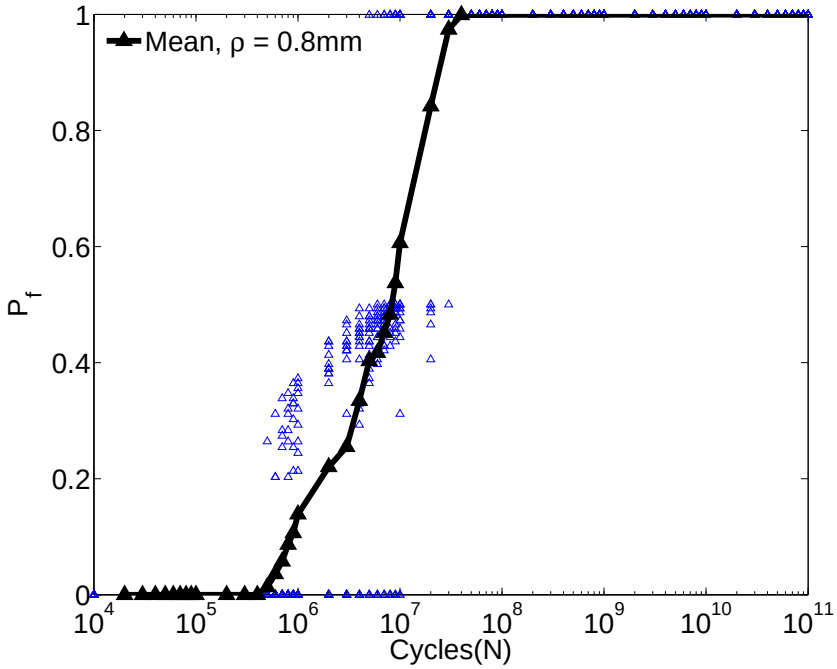


**Figure 4.17:** Cumulative distribution function for coarse grain IN100 with $\rho = 0.8\,\text{mm}$ ($\epsilon_a = 0.6\ \epsilon_y$, $\sigma_a = 450\,\text{MPa}$, $R_\epsilon = -1$).

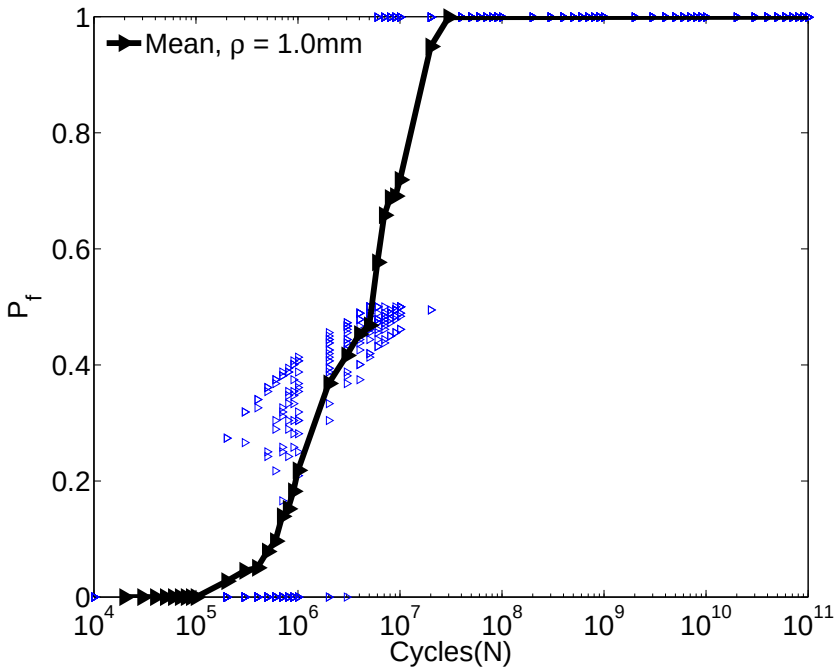


**Figure 4.18:** Cumulative distribution function for coarse grain IN100 with $\rho = 1.0\,\text{mm}$ ($\epsilon_a = 0.6\ \epsilon_y$, $\sigma_a = 450\,\text{MPa}$, $R_\epsilon = -1$).

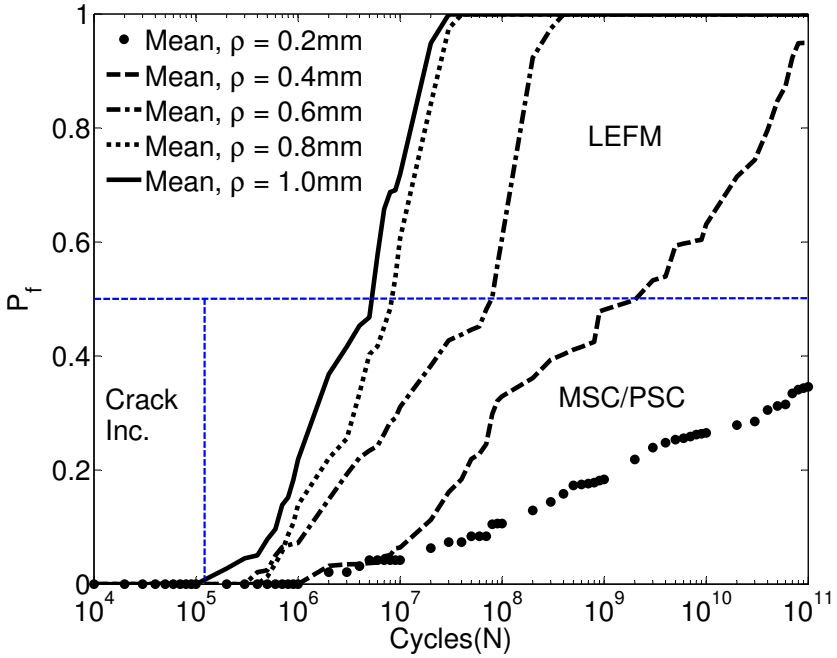


**Figure 4.19:** Comparison of the mean behavior of cumulative distribution functions for different size notches for coarse grain IN100 ($\epsilon_a = 0.6\ \epsilon_y$, $\sigma_a = 450\,\text{MPa}$, $R_\epsilon = -1$).

#### 4.3.2.4 *Equivalent Weibull Stress Function*

An equivalent stress distribution function is introduced to link the applied stress level to the probability of forming a crack to the transition crack length. The CDF in Equation 4.13 is equivalently expressed in terms of an equivalent Weibull distribution as

$$CDF(S_a; L_d, N) = 1 - \exp\left(-\left(\frac{L_d}{L_o}\right)^c \left\langle \frac{\overline{\sigma}}{\sigma_o} \right\rangle^b\right) \tag{4.21}$$

Here, $\overline{\sigma}$ is an equivalent stress function, $\sigma_o$ and $b$ are the Weibull parameters, $L_o$ is a normalization length parameter, and $c$ is a scaling exponent for size effects. The equivalent stress function in this study takes the form of $\overline{\sigma} = K_t S_a - \sigma_L$, where $K_t$ is the theoretical stress concentration factor, $S_a$ is the remotely applied stress, and $\sigma_L$ is the Weibull location parameter.

The Weibull parameters in Equation 4.21 are determined by using the variability in computed FIP values (cf. Figure 4.4 and 4.6) among multiple realizations, along with the recognition of equivalence with Equation 4.13. The equivalent Weibull stress function can be rewritten in terms of a two-parameter equivalent Weibull stress function as

$$F = 1 - \exp\left[-\left(\frac{\overline{\sigma}}{\sigma_o^*}\right)^b\right] \tag{4.22}$$

where $\sigma_o^* = \sigma_o \left(\frac{L_o}{L_d}\right)^{c/b}$. For the transition crack length and the equivalent two-parameter Weibull stress distribution functions (Equation 4.13 and 4.22, respectively) to be equivalent, the terms within the exponential function must be equal, hence,

$$\frac{\eta\ a_n}{L_d} = \left(\frac{\overline{\sigma}}{\sigma_o^*}\right)^b \tag{4.23}$$

One technique for finding the Weibull constants in a two-parameter Weibull distribution function is linear rank regression. Linearization of the transition crack length and equivalent two-parameter Weibull stress distribution functions results in

$$\ln\left[\ln\left(\frac{1}{1-F_m}\right)\right] = b\ln\overline{\sigma} - b\ln\sigma_o^* = \ln(\eta\ a_n) - \ln(L_d) \tag{4.24}$$

This expression is now in the form of a line $y = Ax + B$, where $y = \ln\left[\ln\left(\frac{1}{1-F_m}\right)\right]$, $A = b$, $x = \ln\overline{\sigma}$, and $B = -b\ln\sigma_o^*$. Ranking the values found from the transition crack length approach $(\ln(\eta\ a_n) - \ln(L_d))$ from smallest to largest, we can determine the corresponding estimators for $F_m$ using the median rank statistic as

$$F_m = \frac{m - 0.3}{n + 0.4} \tag{4.25}$$

for the $m$th ranked observation in a sample size $n$ [92]. Therefore, in order to determine the two-parameter equivalent Weibull parameters, the values of $\ln\left[\ln\left(\frac{1}{1-F_m}\right)\right]$ are first plotted versus the values of $\ln[\frac{\eta\ a_n}{L_d}]$ sorted from smallest to largest. As shown in Figure 4.20, the slope corresponds to the Weibull slope parameter, $b$, and the y-intercept is equal to $b\ln\sigma_o^*$.

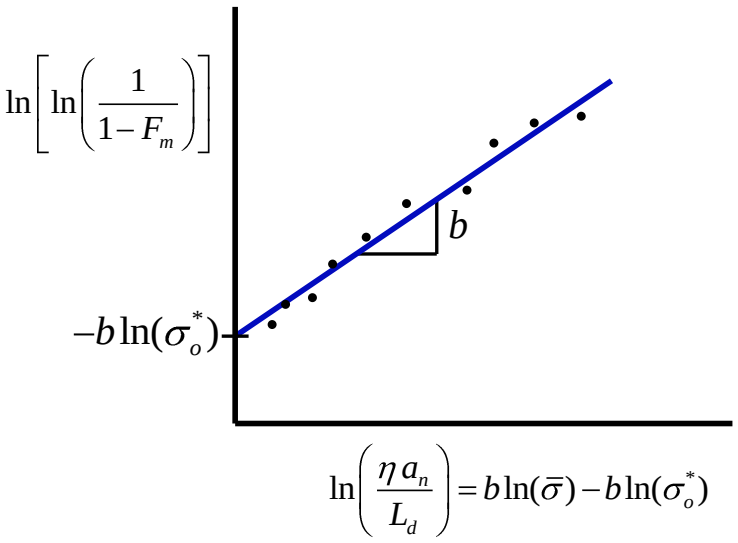


**Figure 4.20:** Method for determining two-parameter equivalent Weibull stress function parameters using values from transition crack length approach.

Using the technique shown in Figure 4.20, the values of the Weibull slope $b$ and Weibull shape factor $\sigma_o^*$ are shown in Figures 4.21 and 4.22, respectively. For the estimation of parameters, only data points that had values of $\frac{\eta\ a_n}{L_d} > 0$ were used. These correspond to the specimens that had initiated cracks. Thus, there was a

transition regime in which only a fraction of the twenty simulated specimens were used in Weibull parameter estimation. It is interesting to note that the Weibull slope and shape parameters increase as a function of the number of cycles. This supports the general trend that variance in fatigue response increases with number of load cycles. The Weibull location parameter, $\sigma_L$, is plotted as a function of number of cycles in Figure 4.23. Once the value of the shape factor $\sigma_o^* = \sigma_o \left(\frac{L_o}{L_d}\right)^{c/b}$ is known, the length scale exponent, $c$ is found by linear regression. In this case, the notch root size, $\rho$, is used in place of $L_d$ because it shows better correlation. In effect, this only changes the scaling factor, $L_o$. The equation for the shape factor can be written as

$$\ln\left[\sigma_o^*\right] = -\frac{c}{b}\ln(\rho) + \frac{c}{b}\ln(L_o^*) \tag{4.26}$$

The shape factor values in the $10^9$ to $10^{11}$ cycle range were used for the estimation of the length scale exponent $c$. In this regime, the change in shape factor as a function of cycles (the slope of the line) appears to be very similar among all notch root radii sizes. In Figure 4.24, the natural log of the shape factor is plotted as a function of the natural log of the notch root radius. Each line in the plot represents the least squares fitting of data points for a given number of cycles. As seen from the graph, the slope $(c/b)$ of these lines is very similar for each data set and is approximately 0.1 in each case. These computationally estimated Weibull parameters and statistical trends need to be verified with experiments.

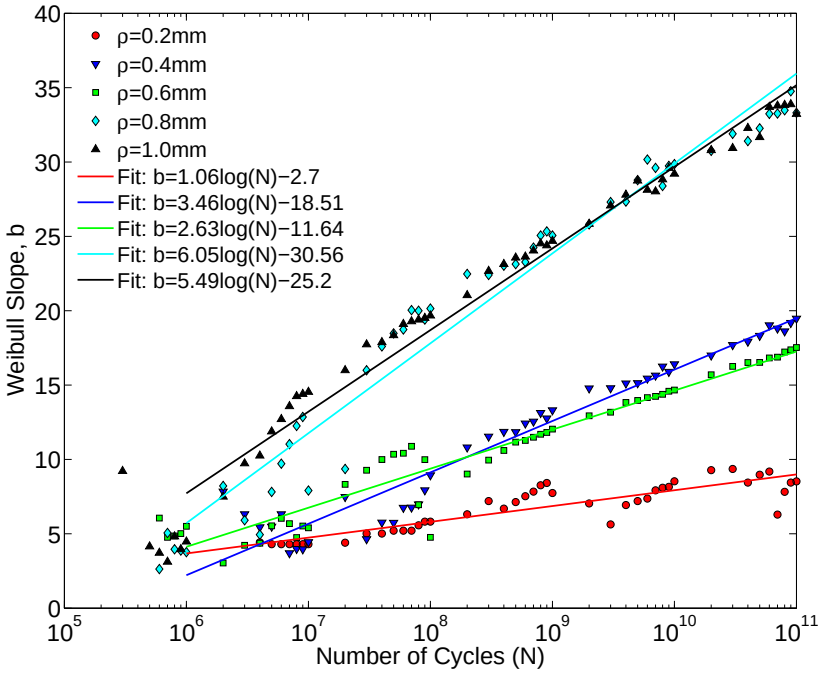


**Figure 4.21:** Weibull slope ($b$) vs. number of cycles for various notch root radii for CG IN100.

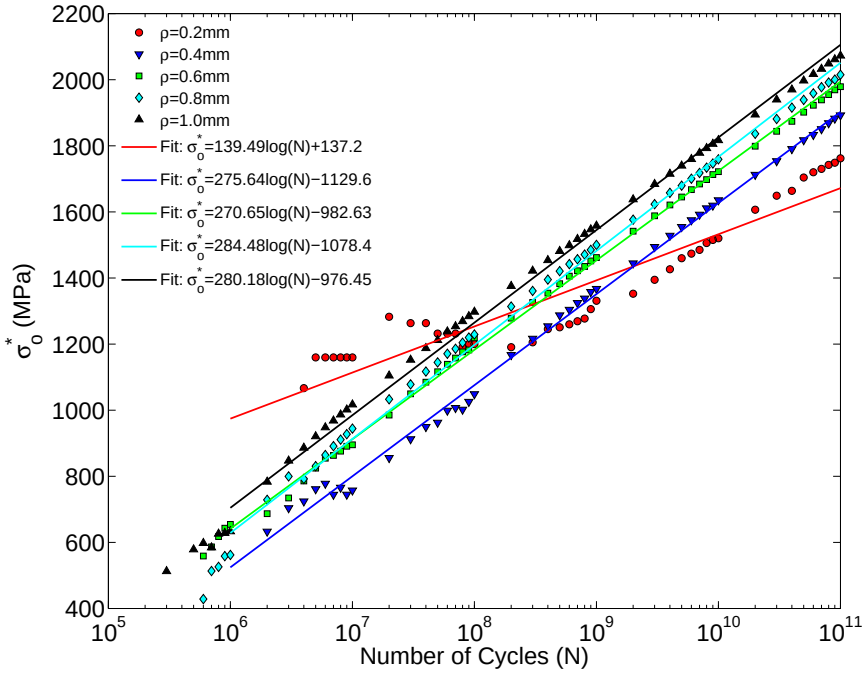


**Figure 4.22:** Weibull shape factor ($\sigma_o^*$) vs. number of cycles for various notch root radii for CG IN100.

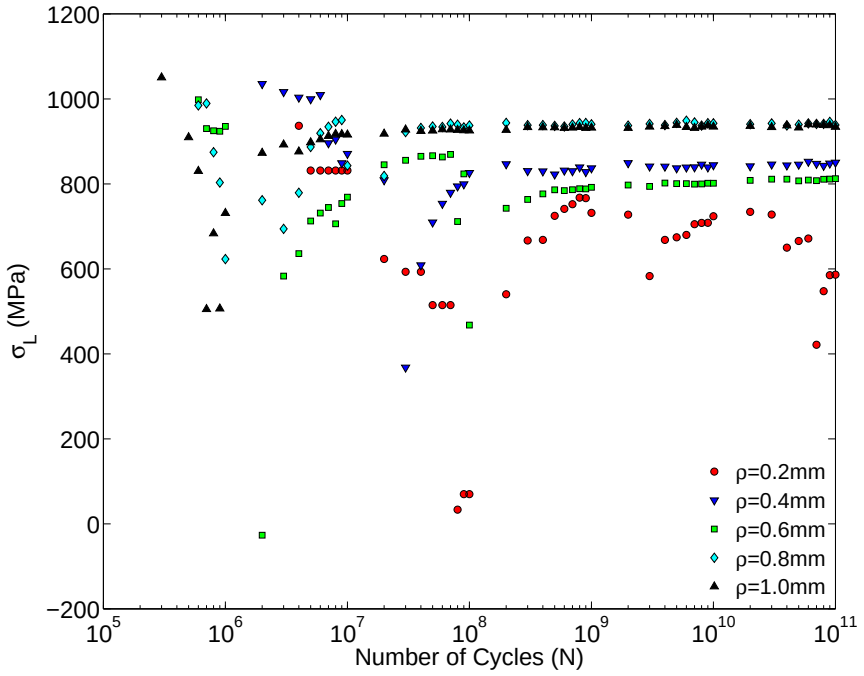


**Figure 4.23:** Weibull location parameter ($\sigma_L$) vs. number of cycles for various notch root radii for CG IN100.

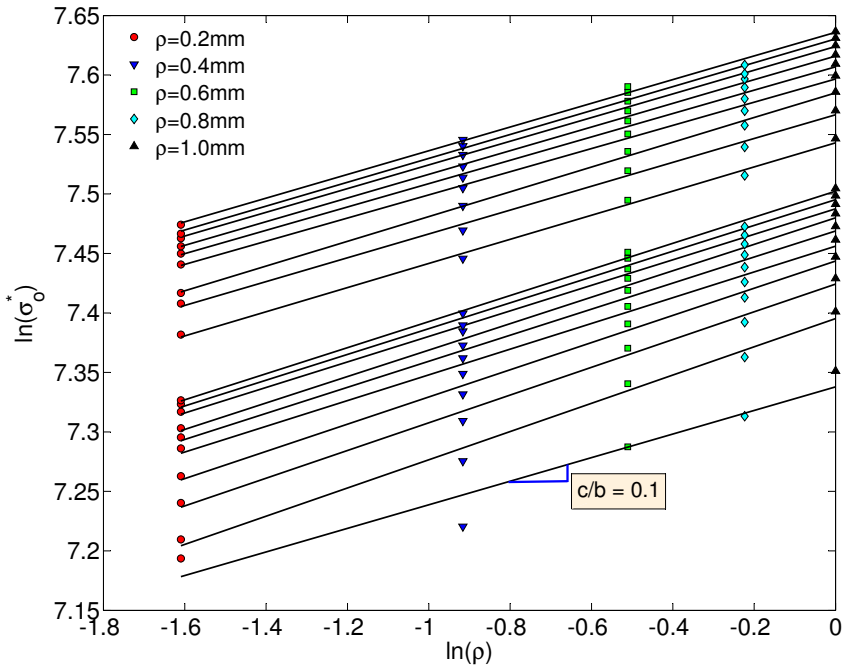


**Figure 4.24:** Method to determine Weibull length scale parameter exponent ($c$).

### 4.3.3 Applications of Transition Crack Length Approach

One limitation of the transition crack length approach is that it simplifies the complex nature of 3D crack formation, growth and nearest neighbor interactions into a simplified model that considers the FIP intensity over a characteristic transition length, similar to average stress models used to analyze notch components. Another issue is that in reality stress redistributes during crack growth and the driving forces for crack propagation increase as the crack size increases, which is not considered in this particular formulation. For this reason, an approach to approximate the FIP redistribution due to crack advance will be developed in future work.

## 4.4 Summary

In this chapter, two different methods were used to analyze the fatigue potency of notched specimens as a function of notch size and applied strain amplitude. The microstructure effect on the fatigue notch factor was taken into account by the distribution of multiaxial-based fatigue indicator parameters. The grain scale approach, which is an extension of previously introduced work within our research group [4], considers the probability of forming a crack on the order of grain size. This approach is applicable to the high cycle fatigue regime in which a majority of life is spent forming a crack to the grain scale. The FIP-based transition crack length approach was used to characterize the probability of microstructurally small crack growth to a transition crack length. Microstructure-sensitive computational crystal plasticity models were used to describe the distribution of FIPs within the notch root region. These distributions were applied to the probabilistic framework described above to find the probability of failure of a notched component and to find a microstructure-dependent probabilistic fatigue notch factor.

# CHAPTER V

# CONCLUSIONS AND RECOMMENDATIONS

## 5.1 Conclusions

Two probabilistic approaches were developed to determine the probability of forming and propagating a crack to a characteristic length. The first approach can be approximated as a fatigue limit approach because it considers the probability of crack formation to the scale of a grain. This is indicative of very high cycle fatigue in which microplasticity or microdamage is very heterogeneous and may only be confined to very few grains. For fatigue cracks propagating past the influence of the first grain, a transition crack length approach was considered. This technique considers the effects of microstructure on the growth of small cracks. These microstructure effects were informed by physically-based crystal plasticity models that are based on key characteristics of the microstructure including grain size, precipitate size, and precipitate volume fraction. Strengthening due to dislocation particle interactions are also considered in this computational model. This model was used to determine the distribution of slip within the notch root region to capture such effects as the notch size effect, peak stress, stress gradient, and microstructure within a notch root zone. These effects are depicted through the use of multiaxial fatigue indicator parameters, such as the maximum plastic shear strain range and the Fatemi-Socie parameter, which are used to describe the stage I, shear-dominated formation and growth of cracks. From simulations, it was shown that the local driving force for fatigue crack nucleation and propagation can vary significantly between different specimens.

Fully three-dimensional finite element analysis is used in this study to qualitatively compare various notch sizes and the relative effect of fatigue strength reduction factor

(a.k.a. the fatigue notch factor) due to the notch effect. The heterogeneity in plastic slip within the notch root region is demonstrated through the use of a three-dimension crystal plasticity model. Using deterministic crack incubation and microstructurally small crack growth models, the probability of specimen failure was determined for each probability framework. It was shown that the crack initiation life was significantly reduced with the introduction of a notch into a specimen.

The techniques employed in this thesis can be used to improve the prediction of HCF life of notched components employing materials with complex microstructures. These techniques can be used in conjunction with experiments to help validate a new material or manufacturing technique to create a variant form of an existing material. Typically, very few experiments are conducted in the high cycle fatigue regime. The time required to experimentally determine the high cycle and very high cycle fatigue response of Ni-base superalloy components necessitates the use of computational and probabilistic strategies and experimental verification in parallel to improve the prediction of fatigue damage due to a notch. The caveat with the probability approaches described above is that more experimental data is needed to verify the computationally created failure probability distribution functions. Especially critical is the characterization of the tails of these distribution functions when designing for minimum life approaches. This extreme value problem is of particular importance in the minimum life design of components loaded under high cycle fatigue [59]. Although the probabilistic framework developed in this thesis was applied to notched Ni-base superalloy components, the framework is general enough that it can be applied to any material system and can be used for multiple failure mechanisms.

## 5.2 Recommendations for Future Work

As alluded to in the background section of this thesis, nonmetallic inclusions and pores play a critical role in the failure of components made from Ni-base superalloy

materials [43, 44]. These inclusions are often introduced into the molten metal prior to the gas atomization process used to create the powder metal [49, 53]. Thus, a probabilistic formulation to determine the failure potency of Ni-base superalloy components should include a consideration for nonmetallic inclusions. However, the main purpose of this thesis was to develop a framework that is able to take into account the effect of microstructure, stress gradient field, and notch acuity on the variability in cyclic fatigue response of a notched component. Therefore, inclusions were not considered in this work so that the effects of the notch root stress field could be distinguished. The techniques employed in this research can be combined with other existing probabilistic formulations that consider the size distribution of defects such as inclusions, the proximity of these defects to the surface, and the competition between different competing damage mechanisms [45, 47, 50, 53, 54]. Also, a close consideration of component size effect must be considered. It has been shown that the statistically weakest "defect" size within a volume can change with the size of the volume [47, 49].

Another direct extension of the current work is to consider the effect of stress redistribution with crack advance. One way to estimate the FIP redistribution due to crack growth is to run simulations on both a cracked and uncracked specimen with the same polycrystalline microstructure within the crystal plasticity zone. The crack can be induced by eliminating elements within the notch root region of an uncracked notched specimen. Other approximation schemes could be developed to estimate the redistribution of FIP values. Another consideration that should be investigated is the effect of neighboring grains on the probability of crack advance. This approach provides an added level of complexity in which the neighboring grain disorientation becomes a factor in the probability of crack advance.

Finally, a consideration for residual stress effects due to surface treatments such as shot peening should be investigated in the future. Shot peening and other forms of compressive pre-stressing of components are extensively used to improve the fatigue

resistance of components subjected to high cycle fatigue. Through shot peening the component surface is strengthened and hardened by the localized cold-working of the material at the surface. The near-surface compressive residual stresses can help offset the tensile portion of an applied load up to a certain depth from the surface. Past this characteristic depth, a residual tensile stress is induced to counteract the surface compressive residual stress. This residual tensile stress within the bulk of the material can be detrimental if not accounted for in component design for fatigue resistance. Also, under higher loads and/or higher temperatures the effect of shot peening may become insignificant due to stress relaxation. These factors will be considered in future work.

# REFERENCES


[1] Shenoy, M., Tjiptowidjojo, Y., and McDowell, D., "Microstructure-sensitive modeling of polycrystalline IN100," *International Journal of Plasticity*, vol. 24, no. 10, pp. 1694–1730, 2008.

[2] Shenoy, M., Zhang, J., and McDowell, D. L., "Estimating fatigue sensitivity to polycrystalline Ni-base superalloy microstructures using a computational approach," *Fatigue & Fracture of Engineering Materials & Structures*, vol. 30, no. 10, pp. 889–904, 2007.

[3] Tjiptowidjojo, Y., Przybyla, C., Shenoy, M., and McDowell, D. L., "Microstructure-sensitive notch root analysis for dwell fatigue in Ni-base superalloys," *International Journal of Fatigue*, vol. 31, pp. 515–525, Mar. 2009.

[4] Owolabi, G., Prasannavenkatesan, R., and McDowell, D., "Probabilistic framework for a microstructure-sensitive fatigue notch factor," *International Journal of Fatigue*, 2010. doi:10.1016/j.ijfatigue.2010.02.003.

[5] Peterson, R. E., *Stress Concentration Factors; Charts and relations useful in making strength calculations for machine parts and structural elements*. Wiley, New York, NY, 1974.

[6] Neuber, H., *Theory of Notch Stresses; Principles for Exact Stress Calculation*. J.W. Edwards, Ann Arbor, MI, 1946.

[7] Bannantine, J. A., Comer, J. J., and Handrock, J. L., *Fundamentals of Metal Fatigue Analysis*. Prentice Hall, Englewood Cliffs, NJ, 1990.

[8] Qylafku, G., Azari, Z., Kadi, N., Gjonaj, M., and Pluvinage, G., "Application of a new model proposal for fatigue life prediction on notches and key-seats," *International Journal of Fatigue*, vol. 21, no. 8, pp. 753–760, 1999.

[9] Weixing, Y., Kaiquan, X., and Yi, G., "On the fatigue notch factor, $K_f$," *International Journal of Fatigue*, vol. 17, pp. 245–251, May 1995.

[10] Weixing, Y., "On the notched strength of composite laminates," *Composites Science and Technology*, vol. 45, no. 2, pp. 105–110, 1992.

[11] Weixing, Y., "Stress field intensity approach for predicting fatigue life," *International Journal of Fatigue*, vol. 15, no. 3, pp. 243–246, 1993.

[12] McDowell, D. L., "Basic issues in the mechanics of high cycle metal fatigue," *International Journal of Fracture*, vol. 80, no. 2-3, pp. 103–145, 1996.

[13] Molski, K. and Glinka, G., "A method of elastic-plastic stress and strain calculation at a notch root," *Materials Science and Engineering*, vol. 50, no. 1, pp. 93–100, 1981.

[14] Ramberg, W. and Osgood, W., "Description of stress-strain curves by three parameters," tech. rep., National Advisory Committee for Aeronautics, Washington, D.C., 1943.

[15] Suresh, S., *Fatigue of Materials*. Cambridge University Press, Cambridge, UK, 2nd ed., 1998.

[16] Luo, J. and Bowen, P., "Small and long fatigue crack growth behaviour of a PM Ni-based superalloy, Udimet 720," *International Journal of Fatigue*, vol. 26, pp. 113–124, Feb. 2004.

[17] Hussain, K., "Short fatigue crack behaviour and analytical models: A review," *Engineering Fracture Mechanics*, vol. 58, pp. 327–354, Nov. 1997.

[18] Tokaji, K., Ogawa, T., and Ohya, K., "The effect of grain size on small fatigue crack growth in pure titanium," *International Journal of Fatigue*, vol. 16, no. 8, pp. 571–578, 1994.

[19] Anderson, T., *Fracture Mechanics: Fundametals and Applications*. Taylor & Francis, Boca Raton, FL, third ed., 2005.

[20] Chan, K. and Lankford, J., "A crack-tip strain model for the growth of small fatigue cracks," *Scripta Metallurgica*, vol. 17, pp. 529–532, Apr. 1983.

[21] Tokaji, K., Ogawa, T., and Kameyama, Y., "The effects of stress ratio on the growth behaviour of small fatigue cracks in an aluminum alloy 7075-T6 (with special interest in stage I crack growth)," *Fatigue & Fracture of Engineering Materials & Structures*, vol. 13, no. 4, pp. 411–421, 1990.

[22] Tokaji, K. and Ogawa, T., "The growth behaviour of microstructurally small fatigue cracks in metals," in *Short Fatigue Cracks, ESIS 13* (Miller, K. J. and de los Rios, E. R., eds.), pp. 85–99, Mechanical Engineering Publications, London, 1992.

[23] Ghonem, H., Nicholas, T., and Pineau, A., "Elevated-temperature fatigue-crack growth in alloy-718 .2. Effects of environmental and material variables," *Fatigue & Fracture of Engineering Materials & Structures*, vol. 16, pp. 577–590, June 1993.

[24] Porter III, W., Li, K., Caton, M., Jha, S., Bartha, B., and Larsen, J., "Microstructural conditions contributing to fatigue variability in P/M nickel-base superalloys," in *11th International Symposium on Superalloys, Superalloys 2008, September 14, 2008 - September 18, 2008*, Proceedings of the International Symposium on Superalloys, (Champion, PA), pp. 541–548, The Minerals, Metals and Materials Society, 2008.

[25] Kumar, R. S., Wang, A. J., and McDowell, D. L., "Effects of microstructure variability on intrinsic fatigue resistance of nickel-base superalloys - a computational micromechanics approach," *International Journal of Fracture*, vol. 137, no. 1-4, pp. 173–210, 2006.

[26] Weibull, W., "A statistical distribution function of wide applicability," *Journal of Applied Mechanics, ASME*, vol. 18, no. 3, pp. 293–297, 1951.

[27] Gumbel, E. J., *Statistics of Extremes*. Columbia University Press, New York, NY, 1958.

[28] Todinov, M., "Probability distribution of fatigue life controlled by defects," *Computers and Structures*, vol. 79, pp. 313–318, 2001.

[29] Todinov, M., "Equations and a fast algorithm for determining the probability of failure initiated by flaws," *International Journal of Solids and Structures*, vol. 43, pp. 5182–5195, 2006.

[30] Wormsen, A., Sjodin, B., Harkegard, G., and Fjeldstad, A., "Non-local stress approach for fatigue assessment based on weakest-link theory and statistics of extremes," *Fatigue & Fracture of Engineering Materials & Structures*, vol. 30, no. 12, pp. 1214–1227, 2007.

[31] Besel, M., Brückner-Foit, A., Motoyashiki, Y., and Schäfer, O., "Lifetime distribution of notched components containing void defects," *Archive of Applied Mechanics*, vol. 76, pp. 645–653, Dec. 2006.

[32] Doudard, C., Calloch, S., Cugy, P., Galtier, A., and Hild, F., "A probabilistic two-scale model for high-cycle fatigue life predictions," *Fatigue & Fracture of Engineering Materials & Structures*, vol. 28, pp. 279–288, Mar. 2005.

[33] Doudard, C., Hild, F., and Calloch, S., "A probabilistic model for multiaxial high cycle fatigue," *Fatigue & Fracture of Engineering Materials & Structures*, vol. 30, pp. 107–114, Feb. 2007.

[34] Weibull, W., "Statistical theory of strength of materials," *Ingeniors Vetenskaps Akademien – Handlingar*, no. 151, p. 45, 1939.

[35] Delahay, T. and Palin-Luc, T., "Estimation of the fatigue strength distribution in high-cycle multiaxial fatigue taking into account the stress-strain gradient effect," *International Journal of Fatigue*, vol. 28, pp. 474–484, 2006.

[36] De Jesus, A. M., Pinto, H., Fernández-Canteli, A., Castillo, E., and Correia, J. A., "Fatigue assessment of a riveted shear splice based on a probabilistic model," *International Journal of Fatigue*, vol. 32, pp. 453–462, Feb. 2010.

[37] Kallmeyer, A. R., Krgo, A., and Kurath, P., "Evaluation of multiaxial fatigue life prediction methodologies for Ti-6Al-4V," *Journal of Engineering Materials and Technology, ASME*, vol. 124, no. 2, pp. 229–237, 2002.

[38] Krö̈ner, E., "Berechnung der elastischen konstanten des vielkristalls aus den konstanten des einkristalls," *Zeitschrift fur Physik*, vol. 151, no. 4, pp. 504–518, 1958.

[39] Krö̈ner, E., "On the plastic deformation of polycrystals," *Acta Metallurgica*, vol. 9, pp. 155–161, Feb. 1961.

[40] Eshelby, J., "The determination of the elastic field of an ellipsoidal inclusion, and related problems," *Proceedings of the Royal Society of London*, vol. 241, no. 1226, pp. 376–396, 1957.

[41] Flaceliere, L. and Morel, F., "Probabilistic approach in high-cycle multiaxial fatigue: volume and surface effects.," *Fatigue & Fracture of Engineering Materials & Structures*, vol. 27, pp. 1123–1135, Dec. 2004.

[42] Papadopoulos, I., "A high-cycle fatigue criterion applied in biaxial and triaxial out-of-phase stress conditions," *Fatigue and Fracture of Engineering Materials and Structures*, vol. 18, no. 1, pp. 79–91, 1995.

[43] Hyzak, J. and Bernstein, I., "Effect of defects on the fatigue crack initiation process in two P/M superalloys - 1. Fatigue origins," *Metallurgical transactions. A, Physical metallurgy and materials science*, vol. 13 A, no. 1, pp. 33–43, 1982.

[44] Hyzak, J. and Bernstein, I., "Effect of defects on the fatigue crack initiation process in two P/M superalloys - 2. Surface-subsurface transition," *Metallurgical transactions. A, Physical metallurgy and materials science*, vol. 13 A, no. 1, pp. 45–52, 1982.

[45] de Bussac, A., "Prediction of the competition between surface and internal fatigue crack initiation in PM alloys," *Fatigue and Fracture of Engineering Materials and Structures*, vol. 17, no. 11, pp. 1319–1325, 1994.

[46] Shenoy, M. M., Kumar, R. S., and McDowell, D. L., "Modeling effects of nonmetallic inclusions on LCF in DS nickel-base superalloys," *International Journal of Fatigue*, vol. 27, no. 2, pp. 113–127, 2005.

[47] Pineau, A., "Superalloy discs durability and damage tolerance in relation to inclusions," *Proceedings of a Conference on High Temperature Materials for Power Engineering 1990*, pp. 913–934, 1990.

[48] Paris, P. and Erdogan, F., "Critical analysis of crack propagation laws," *Journal of Basic Engineering, ASME*, vol. 85, no. 4, pp. 528–534, 1963.

[49] Reed, R. C., *The Superalloys; Fundamentals and Applications*. Cambridge University Press, Cambridge, UK, 2006.

[50] Deyber, S., Alexandre, F., Vaissaud, J., and Pineau, A., "Probabilistic life of DA718 for aircraft engine disks," in *Superalloys 718,625,706 and Derivatives. Proceedings of the Sixth International Symposium on Superalloys 718, 625, 706 and Derivatives, 2-5 Oct. 2005, TMS, Warrendale, PA*, 2006.

[51] Alexandre, F., Deyber, S., and Pineau, A., "Modelling the optimum grain size on the low cycle fatigue life of a ni based superalloy in the presence of two possible crack initiation sites," *Scripta Materialia*, vol. 50, no. 1, pp. 25–30, 2004.

[52] Tomkins, B., "Fatigue crack propagation-an analysis," *Philosophical Magazine*, vol. 18, pp. 1041–1066, Nov. 1968.

[53] de Bussac, A. and Lautridou, J., "A probabilistic model for prediction of LCF surface crack initiation in PM alloys," *Fatigue & Fracture of Engineering Materials & Structures*, vol. 16, no. 8, pp. 861–874, 1993.

[54] Jha, S., Caton, M., and Larsen, J., "Mean vs. life-limiting fatigue behavior of a nickel-based superalloy," in *11th International Symposium on Superalloys, Superalloys 2008, September 14, 2008 - September 18, 2008*, Proceedings of the International Symposium on Superalloys, (Champion, PA, United states), pp. 565–572, The Minerals, Metals and Materials Society, 2008.

[55] Milligan, W., Orth, E., Schirra, J., and Savage, M., "Effects of microstructure on the high temperature constitutive behavior of IN100," *Superalloys 2004. Proceedings of the Tenth International Symposium on Superalloys sponsored by the TMS Seven Springs International Symposium Committee, in Cooperation with the TMS High Temperature Alloys Committee and ASM International, 2004, TMS, Warrendale, PA, USA*, pp. 331–339, 2004.

[56] Wusatowska-Sarnek, A. M., Blackburn, M. J., and Aindow, M., "Techniques for microstructural characterization of powder-processed nickel-based superalloys," *Materials Science and Engineering*, vol. A360, pp. 390–395, 2003.

[57] Wusatowska-Sarnek, A. M., Ghosh, G., Olson, G. B., Blackburn, M. J., and Aindow, M., "Characterization of the microstructure and phase equilibria calculations for the powder metallurgy superalloy IN100," *Journal of Materials Research*, vol. 18, pp. 2653–2663, Nov. 2003.

[58] Kozar, R. W., Suzuki, A., Milligan, W. W., Schirra, J. J., Savage, M. F., and Pollock, T. M., "Strengthening mechanisms in polycrystalline multimodal nickel-base superalloys," *Metallurgical and Materials Transactions*, vol. 40A, pp. 1588–1603, July 2009.

[59] Przybyla, C. P. and McDowell, D. L., "Microstructure-sensitive extreme value probabilities for high cycle fatigue of Ni-base superalloy IN100," *International Journal of Plasticity*, vol. 26, pp. 372–394, Mar. 2010.

[60] Chaboche, J. L., "Constitutive equations for cyclic plasticity and cyclic viscoplasticity," *International Journal of Plasticity*, vol. 5, no. 3, pp. 247–302, 1989.

[61] Bettge, D. and W.Österle, ""Cube slip" in near-[111] oriented specimens of a single-crystal nickel-base superalloy," *Scripta Materialia*, vol. 40, no. 4, pp. 389–395, 1999.

[62] Heilmaier, M., Leetz, U., and Reppich, B., "Order strengthening in the cast nickel-based superalloy IN100 at room temperature," *Materials Science and Engineering*, vol. A319-321, pp. 375–378, 2001.

[63] Reppich, B., Schepp, P., and Wehner, G., "Some new aspects concerning particle hardening mechanisms in $\gamma'$ precipitating nickel-base alloys; ii. experiments," *Acta Metallurgica*, vol. 30, no. 1, pp. 95–104, 1982.

[64] Qin, Q. and Bassani, J. L., "Non-schmid yield behavior in single crystals," *Journal of the Mechanics and Physics of Solids*, vol. 40, pp. 813–833, May 1992.

[65] Qin, Q. and Bassani, J. L., "Non-associated plastic flow in single crystals," *Journal of the Mechanics and Physics of Solids*, vol. 40, pp. 835–862, May 1992.

[66] Shenoy, M. M., Gordon, A. P., McDowell, D. L., and Neu, R. W., "Thermomechanical fatigue behavior of a directionally solidified Ni-base superalloy," *Journal of Engineering Materials and Technology, ASME*, vol. 127, no. 3, pp. 325–336, 2005.

[67] Huther, W. and Reppich, B., "Interaction of dislocations with coherent, stress-free, ordered particles," *Zeitschrift fur Metallkunde*, vol. 69, pp. 628–34, Oct. 1978.

[68] Sinharoy, S., Virro-Nic, P., and Milligan, W. W., "Deformation and strength behavior of two nickel-base turbine disk alloys at $650^oC$," *Metallurgical and Materials Transactions A*, vol. 32, no. 8, pp. 2021–2032, 2001.

[69] Mecking, H. and Kocks, U., "Kinetics of flow and strain-hardening," *Acta Metallurgica*, vol. 29, pp. 1865–1875, Nov. 1981.

[70] Feaugas, X. and Haddou, H., "Grain-size effects on tensile behavior of nickel and AISI 316L stainless steel," *Metallurgical and Materials Transactions A*, vol. 34, pp. 2329–2340, Oct. 2003.

[71] ABAQUS 6.8. Providence, RI, Simulia, 2008.

[72] Fatemi, A. and Kurath, P., "Multiaxial fatigue life predictions under the influence of mean stresses," *Journal of Applied Mechanics, ASME*, vol. 110, pp. 380–388, Oct. 1988.

[73] Fatemi, A. and Socie, D., "A critical plane approach to multiaxial fatigue damage including out-of-phase loading," *Fatigue & Fracture of Engineering Materials & Structures*, vol. 11, no. 3, pp. 149–165, 1988.

[74] McDowell, D., "Multiaxial fatigue strength," *ASM Handbook*, vol. 19, pp. 263–273, 1996.

[75] Findley, K. and Saxena, A., "Low cycle fatigue in Rene 88DT at $650^oC$: Crack nucleation mechanisms and modeling," *Metallurgical and Materials Transactions A*, vol. 37, pp. 1469–1475, May 2006.

[76] Tanaka, K. and Mura, T., "A dislocation model for fatigue crack initiation," *Journal of Applied Mechanics, ASME*, vol. 48, no. 1, pp. 97–103, 1981.

[77] Miller, K. J., "The three thresholds for fatigue crack propagation," in *Proceedings of the 1995 27th International Symposium on Fatigue and Fracture Mechanics, June 26, 1995 - June 29, 1995*, vol. 1296 of *ASTM Special Technical Publication*, (Williamsburg, VA), pp. 267–286, ASTM, 1997.

[78] Miller, K. J., Mohamed, H. J., and de los Rios, E. R., "Fatigue damage accumulation above and below the fatigue limit," in *The behaviour of short fatigue cracks* (Miller, K. J. and de los Rios, E. R., eds.), pp. 491–511, Mechanical Engineering Publications, London, 1986.

[79] Yang, W. and Lee, W. B., *Mesoplasticity and its Applications*. Springer-Verlag, Berlin, 1993.

[80] McDowell, D. L. and Berard, J. Y., "A $\Delta$J-based approach to biaxial fatigue," *Fatigue & Fracture of Engineering Materials & Structures*, vol. 15, pp. 719–741, Aug. 1992.

[81] Forman, R., Kearney, V., and Engle, R., "Numerical analysis of crack propagation in cyclic-loaded structures," *Journal of Basic Engineering*, vol. 89, pp. 459–64, 1967.

[82] Walker, K., "The effect of stress ratio during crack propagation and fatigue for 2024-T3 and 7075-T6 aluminum," in *Effects of Environment and Complex Load History on Fatigue Life*, pp. 1–14, ASTM STP 462, American Society for Testing and Materials, Philadelphia, 1970.

[83] Cowles, B. A., Sims, D. L., and Warren, J. R., "Evaluation of the cyclic behavior of aircraft turbine disk alloys." NASA CR-159409, 1978.

[84] Cowles, B. A., Warren, J. R., and Haake, F. K., "Evaluation of the cyclic behavior of aircraft turbine disk alloys, Part II." NASA CR-165123, 1980.

[85] Gayda, J. and Miner, R. V., "Fatigue crack initiation and propagation in several nickel-base superalloys at $650^oc$," *International Journal of Fatigue*, vol. 5, no. 3, pp. 135–143, 1983.

[86] Bathias, C. and Paris, P. C., "Gigacycle fatigue of metallic aircraft components," *International Journal of Fatigue*, vol. 32, no. 6, pp. 894–897, 2010.

[87] Bathias, C. and Paris, P. C., *Gigacycle Fatigue in Mechanical Practice*. Marcel Dekker, New York, NY, 2005.

[88] Tsutsumi, N., Murakami, Y., and Doquet, V., "Effect of test frequency on fatigue strength of low carbon steel," *Fatigue & Fracture of Engineering Materials & Structures*, vol. 32, no. 6, pp. 473–483, 2009.

[89] Bathias, C., "There is no infinite fatigue life in metallic materials," *Fatigue & Fracture of Engineering Materials & Structures*, vol. 22, pp. 559–565, July 1999.

[90] Groeber, M., Ghosh, S., Uchic, M. D., and Dimiduk, D. M., "A framework for automated analysis and simulation of 3D polycrystalline microstructures.: Part 1: Statistical characterization," *Acta Materialia*, vol. 56, pp. 1257–1273, Apr. 2008.

[91] Cohen, A. C., "Maximum likelihood estimation in Weibull distribution based on complete and on censored samples," *Technometrics*, vol. 7, no. 4, pp. 579–588, 1965.

[92] Bury, K. V., *Statistical Models in Applied Science*. John Wiley, New York, NY, 1975.

[93] Cohen, A. C. and Whitten, B., "Modified maximum-likelihood and modified moment estimators for the 3-parameter Weibull distribution," *Communications in Statistics Part A - Theory and Methods*, vol. 11, no. 23, pp. 2631–2656, 1982.

[94] Whitten, B. J. and Cohen, A. C., "Further considerations of modified moment estimators for Weibull and lognormal parameters," *Communications in Statistics - Simulation and Computation*, vol. 25, no. 3, pp. 749–784, 1996.

[95] Smith, R. A. and Miller, K. J., "Fatigue cracks at notches," *International Journal of Mechanical Sciences*, vol. 19, no. 1, pp. 11–22, 1977.

[96] Caton, M. and Jha, S., "Small fatigue crack growth and failure mode transitions in a Ni-base superalloy at elevated temperature," *International Journal of Fatigue*, 2010. doi:10.1016/j.ijfatigue.2010.01.015.